INFORMATION TO USERS

This manuscript has been reproduced from the microfilm master. UMI films the text directly from the original or copy submitted. Thus, some thesis and dissertation copies are in typewriter face, while others may be from any type of computer printer.

The quality of this reproduction is dependent upon the quality of the copy submitted. Broken or indistinct print, colored or poor quality illustrations and photographs, print bleedthrough, substandard margins, and improper alignment can adversely affect reproduction.

In the unlikely event that the author did not send UMI a complete manuscript and there are missing pages, these will be noted. Also, if unauthorized copyright material had to be removed, a note will indicate the deletion.

Oversize materials (e.g., maps, drawings, charts) are reproduced by sectioning the original, beginning at the upper left-hand corner and continuing from left to right in equal sections with small overlaps.

Photographs included in the original manuscript have been reproduced xerographically in this copy. Higher quality 6" x 9" black and white photographic prints are available for any photographs or illustrations appearing in this copy for an additional charge. Contact UMI directly to order.

Bell & Howell Information and Learning 300 North Zeeb Road, Ann Arbor, MI 48106-1346 USA 800-521-0600



Ultrasonic Digital Beamformation: A Comparative Study

Sunil Vasudevan

September 14, 1998

Department of Electrical Engineering McGill University, Montreal, Canada

A thesis submitted to the Faculty of Graduate Studies and Research in partial fulfillment of the requirements of the degree of Masters of Engineering

© Sunil Vasudevan, 1998



National Library of Canada

Acquisitions and Bibliographic Services

395 Wellington Street Ottawa ON K1A 0N4 Canada Bibliothèque nationale du Canada

Acquisitions et services bibliographiques

395, rue Wellington Ottawa ON K1A 0N4 Canada

Your file. Votre référence

Our file Notre référence

The author has granted a nonexclusive licence allowing the National Library of Canada to reproduce, loan, distribute or sell copies of this thesis in microform, paper or electronic formats.

The author retains ownership of the copyright in this thesis. Neither the thesis nor substantial extracts from it may be printed or otherwise reproduced without the author's permission.

L'auteur a accordé une licence non exclusive permettant à la Bibliothèque nationale du Canada de reproduire, prêter, distribuer ou vendre des copies de cette thèse sous la forme de microfiche/film, de reproduction sur papier ou sur format électronique.

L'auteur conserve la propriété du droit d'auteur qui protège cette thèse. Ni la thèse ni des extraits substantiels de celle-ci ne doivent être imprimés ou autrement reproduits sans son autorisation.

0-612-50670-3



Abstract

Real-time ultrasonic imaging systems have been available for more than fifty-five years and are becoming an important tool in the practice of modern medicine. During this time much has occurred to the basic architecture and functions of these clinical systems and their beamformers, which are, in many ways, the most important components of these systems. Throughout most of the 30 years of real time imaging, analog beamformers have been the mainstay of all ultrasonic instruments. But at the present time the industry is undergoing a major shift toward digital beamformation with the introduction of several commercial systems. The thesis will look at the evolution of digital ultrasound beamformers, some of the changes that have occurred and will discuss current trends in beamformer design. Typical analog and digital beam formers have been simulated and their performance compared in terms of beam width, side lobe levels and signal-to-noise ratio. Also the effect of apodization on images have been examined. Experimental investigations have been carried out to compare delay-sum -add and synthetic aperture imaging on different phantoms. The technical challenges in digital beamformation will be reviewed, as also the constraints introduced by today's market place. Finally, the future of digital beamformation in the context of advances in computer and microelectronics technologies is discussed.

Resumé

Les systèmes d'imagerie ultrasonic en temps réel sont disponibles depuis plus de cinquante ans, mais à présent, ces systèmes prennent de plus en plus d'importance au sein de la médecine moderne. Durant ces cinquante ans, plusieurs changements à l'architecture et fonctions de ces systèmes ont beaucoup evolués, surtout pour ce qui est des composantes des ces systèmes qui font la focalisation. Les focaliseurs analogues ont dominé les trente dernieres années. Cependant, de nos jours, l'industrie fait un virage vers la focalisation digitale. Cette thèse présente une retrospective sur l'évolution des systèmes de focalisation ainsi qu'un aperçu sur les tendances contemporaines pour ces systèmes. La résolution latérale et le niveau du lobe secondaire sont étudiés et les résultats de ces études démontrent qu'en reduisant le niveau des lobes secondaires, la résolution latérale se detériore. Des systèmes de focalisation communs, analogues et digitales, sont simulés et leur performance comparée en terme d'étendu du faisceau, l'importance des lobes secondaires, et le ratio de signal au bruit. expérimentales comparent les performances des systèmes delai-somme contre celle des systèmes d'ouverture synthétique. Imagerie d'ouverture synthétique permet d'augmenter la vitesse des fenêtres de données, mais les systèmes delai-somme ont de lobes secondaires plus petits, et des faisceaux plus étendus. Les défis techniques dans la focalisation digitale sont discutés, ainsi que les contraintes presentes dans les marchés commerciaux. Finalement, le futur de la focalisation digitale, étant donné les avances dans les domaines de la microelectronique et del'informatique, sera presentée.

Acknowledgement

Firstly I would like to thank **God** for giving me health and patience in completing this thesis. Over the two years that I spent on research, for my thesis, many people have helped me to reach my objective of completing it. I take this opportunity to thank them all. The time spent on my graduate work has not only been, a learning exercise academically but also an enriching one personally.

First of all I would like to thank my supervisor **Dr Kenneth Watkin**, Ph.D. for his wonderful supervision. No words are big enough to convey my heartfelt gratitude to him. His excellent guidance, suggestions and sharp insights have helped me in completing my thesis. His great sense of humor has only made my experience at the laboratory an enjoyable one. It has been a privilege working under his supervision.

I would like to thank my colleagues Ibrahima Diouf, Souheil Hakim, Amol Karnick and Jeri Miller for their comments and helpful tips. I would especially like to thank Ibrahima Diouf for the many hours spent listening and discussing problems encountered during my thesis work. My sincere thanks to Hossein Najafzadeh-Azghandi of Telecommunication and Signal Processing lab, McGill University for his invaluable help and comments. Thanks also to Michael Godbout for his help with french abstract.

I am thankful to Bernard Charbneau of Instrumentation Scientifique et Medicale Inc., Montreal and Ernest L. Madsen of Dept of Medical Physics and Engineering, University of Wisconsin, Madison for being kind enough to lend me their phantoms. Thanks also to Charles Borm, Biomedical engineer, Royal Victoria Hospital, Montreal for all the technical support and help.

Finally, my thanks, to my family and relatives. Thank you, Mom and Dad for your unstinted support and encouragement. I am thankful to my brother, Dr Anil Vasudevan and sister Ms Sunita Vasudevan for motivating me. "Thanks" is too small a word for all that my Uncle and Aunt have done for me while taking care of me here in Canada (sorry that I eat too much!). It has been a wonderful two years that I spent with you. Thanks, Anita and Ajay for putting up with me over the two years. Finally my thanks to Mr Gopalkrishnan Menon and Ms Prema Menon for all their help and patience.

Table of Contents

1. INTRODUCTION	1
1.2 Why is digital beamformation gaining importance	4
2. BEAMFORMER BASICS	5
2.2 TRANSDUCER ARRAYS	7
A) Sequential Array Scanners	7
B) Mechanical Array Scanners	
C) Phased Array Scanners	9
3. BEAMFORMER DEVELOPMENT	10
3.1 EVOLUTION OF DIGITAL BEAMFORMATION	13
4. APERTURE THEORY AND FAR_FIELD DIRECTIVITY FUNCTIONS	21
4.1 LINEAR APERTURES	22
4.2 AMPLITUDE WINDOWS	23
4.3 BEAM STEERING AND FOCUSING	27
4.4 ARRAYS	28
4.4.1 The Phased Array (Beam Steering)	32
5. METHODS AND PROCEDURES	35
5.1.1 DATA ACQUISITION	
5.1.2 SIGNAL PROCESSING AND IMAGE RECONSTRUCTION	
5.1.3 PHANTOMS	
5.1.4 SYSTEM PARAMETERS	
5.1.4a Beam Angle	
5.1.4b Temporal Sampling Period	
5.1.4c Spatial Sampling Period	41
5.1.4d Filter cut-off frequencies	42
5.1.4e Attenuation Coefficients	
5.1.4f Inverse Filter	43
6. SIMULATION AND EXPERIMENTS	45
6.1 SIMULATIONS	45
6.2 EXPERIMENTAL INVESTIGATIONS	
6.2.1 Delay-Sum-Add architecture	
6.2.2 Synthetic Aperture architecture	
7. RESULTS	54
7.1 SIMULATIONS	54
7.2 EXPERIMENTAL INVESTIGATIONS	
7.2.1 Delay-Sum-Add architecture	
7.2.2 Synthetic Aperture architecture	
8. DISCUSSION	66
8.1 SIMILI ATIONS	66

8.2 EXPERIMENTAL INVESTIGATIONS			
9. FUTURE WORK		•••••••	79
10. CONCLUSION			81
11. BIBLIOGRAPHY		*******************************	82

1. Introduction

The use of ultrasound imaging has been studied since the early 1950's. During this time, advances in technology and clinical practice have made ultrasound a leading medical diagnostic imaging modality. Modern ultrasound equipment is relatively inexpensive and portable. As the demand for higher quality ultrasound images increase, 'beamformation' plays an important role in advancing image quality and reducing the cost of equipment. The term "beamforming" is usually applied to focusing of transmit pulses and received data.

Figure 1.1 shows a simplified block diagram of a typical medical ultrasound scanner. The transducer converts electrical signals produced by the pulser into acoustic energy and converts returning acoustic energy into electrical signals. They are then beamformed and the resulting composite signal is processed and formatted for display. Beamforming in commercial equipment may have variations and employ different techniques. A distinction that is important in the industry is whether a beamformer is analog, hybrid or digital. An analog beamformer uses analog delay elements for focusing. A hybrid beamformer may introduce analog mixers for fine delay and/or basebanding. A digital beamformer will have analog-to-digital converters immediately following the TGC amplifiers, where all focusing delays are implemented digitally.

The earliest phased array beamformers were developed in the late 1960's for imaging of the brain [9] and improved in the early 1970's for echocardiography [10, 11, 12]. These

early systems involved relatively simple implementations of beamformer functions [9, 10]. For focusing lumped L-C delay lines were used as delay elements. Real-time sector scanning, where the beams are steered in particular directions, required rapid switching among a great number of delay configurations, which required a complex control system and produced undesirable switching noise in the analog delay lines. For dynamic focusing and steering, L-C delay lines as delay elements were extremely bulky, since the delay patterns for focal points through the depth along the radial direction are different for each element and for each steering direction, requiring very complex switching circuitry. Also due to inherent artifacts such as insertion loss, impedance mismatching and switching transients the L-C lines were replaced by electronic delays. Gradually, digital beamformation evolved from beamformers with electronic delays to complete digital beamformation systems (DBF). Underlying all these changes, are known mathematical relationships. These relationships and associated computer simulations, illustrate the changes brought about by the beamformer evolution and are explored in this thesis.

Digital beamformation has witnessed significant advances and changes recently. It has evolved from simple delay and add architecture [5, 7, 8, 9, 11, 13, 21, 24] to complex synthetic array beamforming [28, 29, 30, 31, 32, 33, 34] with many features like phase aberration correction etc., while techniques like frequency-domain beamforming, have not received wide acceptance.

The thesis is organized as follows. Section 2 describes the functions of a generic beamformer. The functions performed by a beamformer are reviewed and a generic block diagram is given. The basic beamformation equation will be used to identify those components, which have been modified during the evolution process. The different types of arrays employed for beamforming are described.

Section 3 reviews beamformer development. Performance comparison of analog and digital delay lines are presented in table format. Section 3 then traces the evolution of digital beamformation and changes that have occurred. Heavy use is made of diagrams to show various changes that have been made in beamformation over the years.

Section 4 describes the theory behind beam steering and focusing in terms of aperture function, apodization, etc. These mathematical functions are the basis for most of the simulations carried out in this thesis. Graphical depiction of ultrasound beamshapes are used to describe the influences of various parameters described.

Section 5 describes the method and procedures for all experimental investigations conducted as part of this thesis. A brief description of all the phantoms used are given and also the system parameters used in the investigations are described.

Section 6 describes the simulations conducted that compare the performances of an analog and digital beamformer. The effect of apodization, discussed in Section 4 on images will be studied through the simulations. Given the trends in digital beamformer

development, Section 6 also describes the architecture of the two different implementation of DBF: Delay-Sum-Add (DSA) architecture and Multi-element synthetic aperture focusing architecture (M-SAF) and comapre their performances through experimental investigations.

Section 7 presents the results obtained from the simulation and investigations carried out in the thesis and Section 8 discusses the results presented.

Section 9 discusses the future work. Some of the unique challenges associated with digital beamformation described. Section 10 summarizes the findings of this research and their implications.

1.2 Why is digital beamformation gaining importance?

The general motivation to move towards digital beamformation is to achieve multifunction use in a flexible format. Examples are

- The resolution of ultrasonic images is greatly enhanced using digital control of weight vector to achieve beamwidth control.
- It enables more precise and rapid changing of the receiver delay times, so that the focal point may track the returning echoes along any steering direction.
- A sufficiently high dynamic range of the echo information can be stored.
- Frame rate can be increased by simultaneously forming multiple beams.

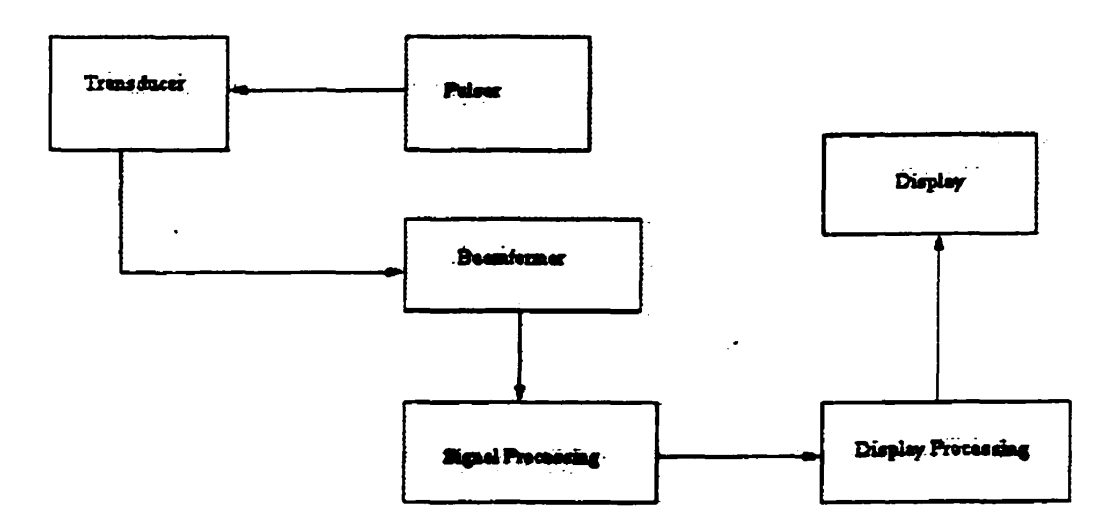


Figure -1.1 Schematic diagram of a ultrasound scanner

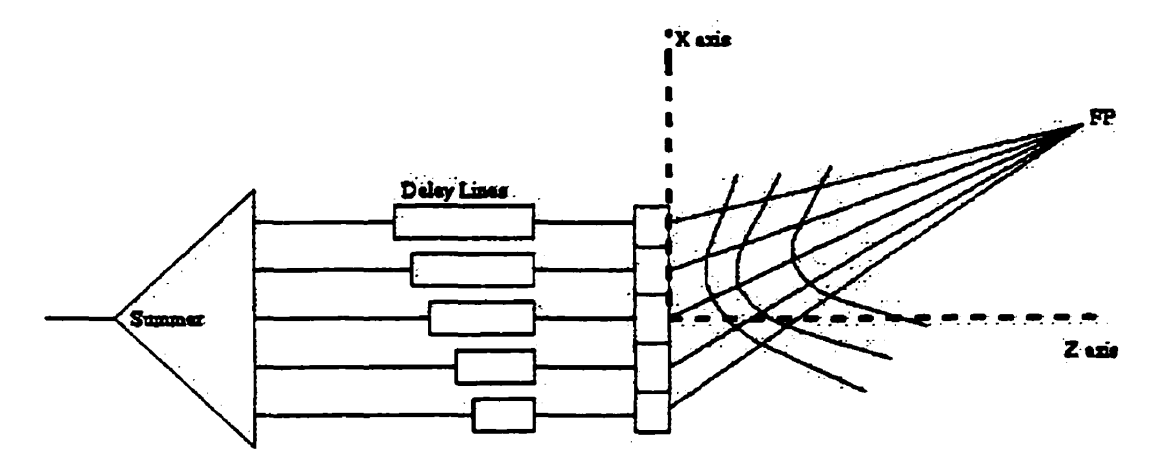


Figure -2.1 Basic geometry for beamformer calculations

2. Beamfomer Basics.

The functions of a beamformer include the following:

- generate transmit timing and possible apodization (the term apodization will be used as a synonym for weighting, tapering and shading) during transmit.
- supply the time delays and signal processing during receive.
- supply apodization and summing of delayed echoes.
- possible additional signal processing related activities.

The goal of all of these functions is to create a narrow, uniform beam with low sidelobes over as long a depth as possible. During both transmit and receive operations, appropriate delays are supplied to accomplish the focusing and steering needed. Figure 2.1 demonstrates the geometry that is usually used. Figure 2.1 also illustrates the reception process. Wavefronts are shown emanating from a point source labeled as FP. These signals are received by the array elements, amplified and passed on to the delay lines. The delay lines are shown as rectangular boxes whose length corresponds to the desired delay. Finally, the echoes are passed on to the apodization/summer stage, which takes the contributions from each element, multiplies them with a weighting function, and adds up the results. The transmit operation is essentially the inverse of receive focusing; time delays from a common synchronization signal are generated by some means, often down counters, and the array elements are fired accordingly. It is assumed the array elements act as point sources and generate the required wavefronts.

The general expression for the received echo r(t):

$$r(t) = \sum_{i=1}^{N} A_{ii} \sum_{j=1}^{N} A_{xj} s \left(t - \tau_{ii} - \tau_{xj} + \frac{2 R_{jp}(t)}{c} \right). \tag{2.1}$$

In this expression, the transmitted waveshape is s(t). The A's refer to whatever weighting function that might be applied to each of the channels during the transmit and receive operations. In the simplest case these would be equal to one for uniform aperture weighting. $R_{fp}(t)$ is the distance of the source point (FP) from the center of the transducer array and c is the velocity of the wavefront in meters per second. Similarly, τ 's refer to the transmit and receive delays applied during transmit and receive beamformation operations. i and j are indices of the receive and transmit elements, respectively, and subscripts r and x refer to receive and transmit operations. These four parameters, A_{ri} , A_{xj} , τ_n , and τ_{xj} will form the basis of the discussion on beamformer evolution; changes in their values and in the methods by which their role has been implemented has defined the different generation of instruments. Quality of beamformation is strongly influenced by them.

Finally, in Equation 2.1, N is the number of transmit and receive elements and will assumed to be constant. N is also an important factor in establishing the performance level and the cost of an ultrasound system.

Referring to Figure 2.1, the expression for determining the values for the transmit and receive delays given a desired focal point is:

$$\tau_i = \frac{1}{c} \left[\sqrt{(x_i - z_{fp})^2 + z_{fp}^2} - R_{fp} \right]$$
 (2.2)

In this expression, c is the speed of sound, τ_i is the transmit or receive delay, x_{fp} and z_{fp} are the coordinates of the point at which we wish to focus, and R_{fp} is the distance from the origin or the phase center to that focal point. The focal point may be one of the following:

- a fixed point in space such as a transmit focal point
- a point which moves at the speed of sound with the wavefront of the transmitted pulse in dynamic focusing
- a point corresponding to a pixel in an image to be formed as with a synthetic aperture approach

These cases will be discussed as they arise in the thesis.

2.1 Transducer Arrays

Beamformers come in a wide variety of sizes and capabilities with much of this variability coming from different types of transducer arrays the beamformer service. The commonly used arrays are described below:

A. Sequential Linear Array Scanners

A linear array consists of a number of small individual transducers arranged side by side in a single assembly. Two-dimensional images are produced in a sequential array scanner by transmitting on each of the array elements and receiving the echo information with the same elements for each B-mode line in the final display. This sequence of image formation which results in a rectangular image format can be illustrated with reference to Figure 2.2. For the sake of simplicity, five elements of the linear array are shown. Element 1 is pulsed first, and echoes from the insonification are received by the same element producing the top B-mode line in the final display. At the completion of this transmit-receive operation, the second element is pulsed, and the echoes received by this element produces the second line of display. This sequence continues until the last element has been fired to produce the bottom or last line in the display. In general, for these type of systems, the number of unique B-mode lines corresponds to the number of elements in the linear array. As a result of the electronic scanning in these systems, as well as the relatively low number of image lines per frame, very high frame rates are possible. In these systems, the field of view is identical to the total length of the array.

B. Mechanical Sector Scanners.

Mechanical sector scanners include one or more piston transducers which are rocked or rotated about a fixed axis by means of an electric motor. Usually the transducers are contained in a liquid filled housing with an acoustic window, and the entire assembly is directly placed onto the skin surface to produce the resulting image in a circular sector format. Individual B-mode lines are scanned radially from a common orgin corresponding to the center of rotation.

C. Phased Array Sector Scanners.

Phased array scanners are the most sophisticated real-time systems. These utilize a small array transducer which readily allows visualization of anatomic structures through restricted acoustic windows. Phased array systems produce images by rapidly steering the acoustic beam through the target organ by electronic rather than mechanical means. In contrast to the sequential linear array scanners, all of the array elements in a linear phased array system are utilized in producing each of the individual B-mode lines which comprise the final two-dimensional image. Figure 2.3 shows a five element phased array, where appropriate delays are applied to steer the beam and focus at the predetermined point.

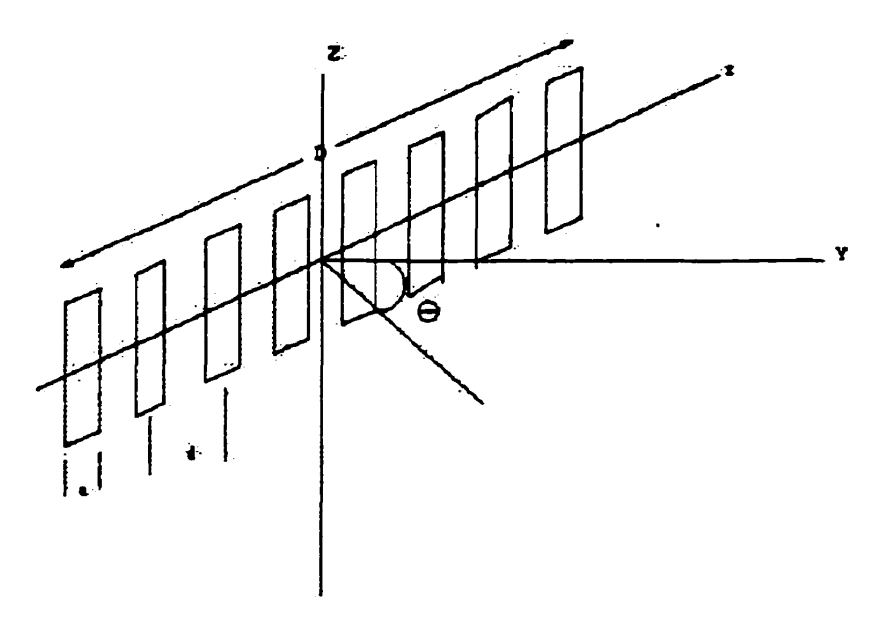


Figure -2.2 Design of N element linear array of aperture size $D \times L$, element separation d, and element size a.

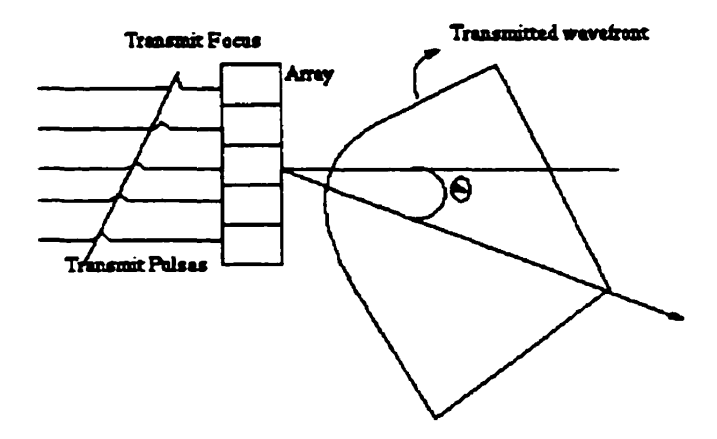


Figure -2.3 Phased array transmit steer (angle 6) and focus by using delays

3. Beamformer Development

In this section we will review the major evolutionary steps in beamformer development.

The earlier designs[10, 11,12] relied mostly on using a collimated beam and narrowing of the beamshape at the near-to-far field transition. Several significant limitations are immediately apparent. For example, the focal region is quite limited, the sidelobe levels are quite high, and the near field extensive. The transmit only beamformer equation generally used is given below:

$$r(t) = \sum_{j=1}^{N} A_{xj} s(t - \tau_{xj} + \frac{2R_{fp}(t)}{c})$$
 (3.1)

The limited focal region is directly associated with the use of constant values for the τ_{xi}

in Equation 3.1. As a consequence the τ_{xy} will cancel the $\frac{2R_{fp}(t)}{c}$ term only in one location. Further, there is the need to use a high f-number so that the depth of field is acceptable for routine imaging. It is likely that the limited focusing capabilities along with extensive near field and high side lobe levels are the major reasons why the market acceptance of real-time systems was fairly slow. The mechanical B-scanners dominated well into the late 1970's.

The need to suppress sidelobes in clinical imaging was recognized by Thurstone and Von Ramm [11]. The combination of transmit and receive beamformation does lower sidelobe levels considerably. This performance can be dramatically improved by the introduction of apodization or weighting of transmit pulses and/or received echoes by an appropriate weighting function. This was demonstrated and reported in several research papers in the

70's [11, 18, 48, 55]. Apodization became available in commercial instruments starting from about 1980 and onwards. Along with dynamic apodization came the capability to increase the aperture size dynamically during receive, i.e. dynamic aperture.

The concept of dynamic focusing with medical ultrasound transducers goes back to the 1950's[41]; however, its reduction to practice required about 20 years. The first Duke University phased array system [49, 51] was capable, at least in principle of employing dynamic focusing and reports of designs capable of dynamic focus were reported in the literature in the late 1970's and early 80's [7, 18, 29, 52]. A major benefit from dynamic focusing is the ability to lower the f-number during receive beamformation and to keep it relatively constant until the end of the aperture. This was of obvious value with high channel (i.e. number of transducer elements in an array) count systems. Implementation of dynamic focusing in analog beamformers is usually accomplished by the use of coarse and fine delay circuit blocks. In a typical design the coarse delay was realized by the use of a summing delay line which was preceded by a cross-point switch to deselect the appropriate tap for a particular channel. Two types of fine delay implementations have been reported:

- by heterodyning the received signal to baseband or an intermediate frequency with a mixing signal whose phase was changed as needed for dynamic focusing [7, 18, 29]
- by choosing a tap of a shorter delay line by a very carefully designed switch or switches [2, 49].

The heterodyning approach is more of a narrowband approach in that the fine delay correction is valid over a limited frequency range [47]. However phase and hence the time delay control that is achievable with this method exhibits good resolution.

There is considerable subtlety to the implementation of the required delays as well as the selection of delay quanta and other parameters. Later on, much interest was shown on the amplitude and phase quantization on sidelobes as well as grating lobes [3, 4, 28, 32, 34, 40, 46, 47]. Much of the cost variations associated with different types of systems is related to the extent to which the system designers have attempted to minimize these quantization errors. The entry into digital beamformation has required, however a re-evaluation of many of these issues

Table 1. Comparisons of various delay systems.

Device	Delay	Programmability	Bandwidth	Dynamic Range	Cost
Lumped Elements	Electromagnetic propagation	Digital tap selection	Tap density dependent	High(accurate matching)	increases with Delay
Charge transfer device	Serial charge transfer	Clock frequency	~ 5 MHz	40-50 dB (cti)	
Serial analogue memories	Single charge transfer	Clock timing	~ 6 MHz	< 30 dB	
Digital	A/D + memory	Clock timing	A/D sampling rate dependent	A/D bit-number dependent	Increases with sample rate

3.1 Evolution of Digital Beamformation.

This section will trace the development of digital beamformation. We will start from the very early designs and work our way towards the present.

The earliest works on use of digital control for delays appeared in 1975 [19]. A technique was developed for use of charge coupled devices (CCD) to provide programmable time variable analog signal delay for scanning a linear ultrasonic phased array. This technique had dynamic focusing depths of 2 to 40 cm. The element delays were controlled by a 8080 microprocessor. Figure 3.1 shows the system operation of the earliest attempt at digitally controlling delays.

Even though digital control was used to control delays, the concurrent use of analog delay lines created major problems in imaging like image artifacts. This led to the development of electronic delay lines and new techniques for dynamically varying the electronic delay lines. For the first time, the concept of sampled data systems was used to implement circuits for electronic delay lines [8]. The underlying principle behind these delay schemes involved buffering the sampled data in a memory with independent read/write ports. The stored samples are read out after an appropriate number of clock cycles to generate an on-line, pipeline delay (Figure 3.2a). Another variation of implementing a delay line was also described [8, 20]. A FIFO (first in first out) device in conjunction with a RAM memory was used. The FIFO eliminates the addressing circuitry needed for RAM implementation. The delays thus implemented are long with high precision, broad bandwidth and minimum phase distortion. Furthermore, the development

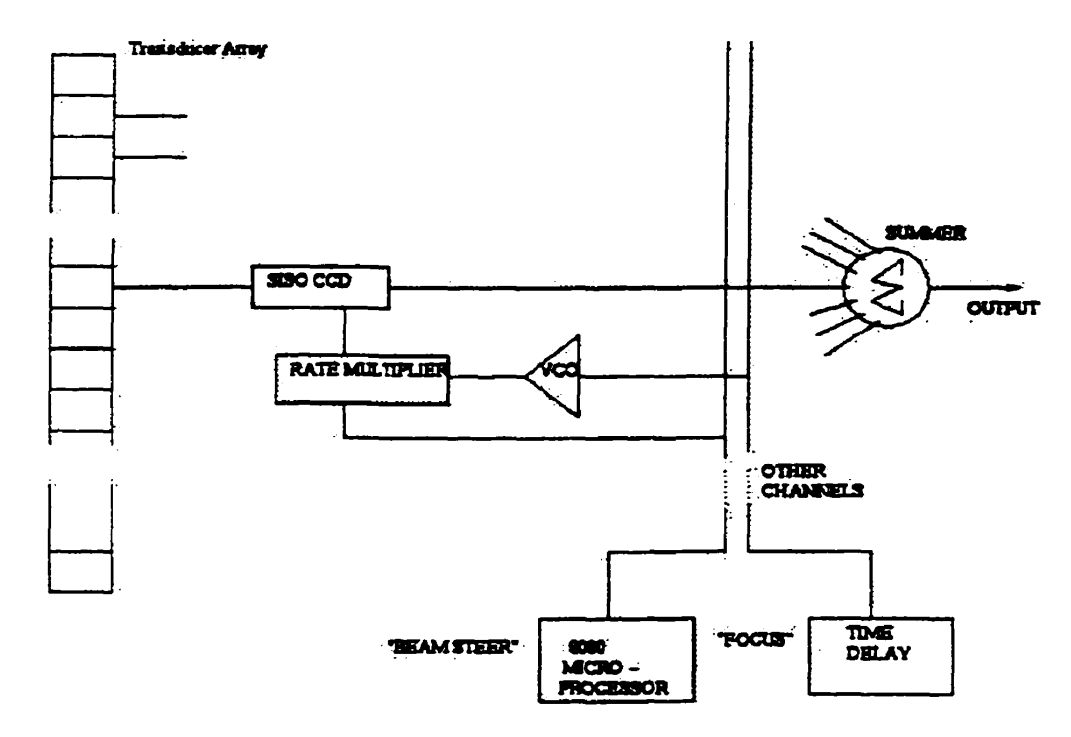


Figure -3.1 Simplified system operation of earliest attempt at digitally controlling delays

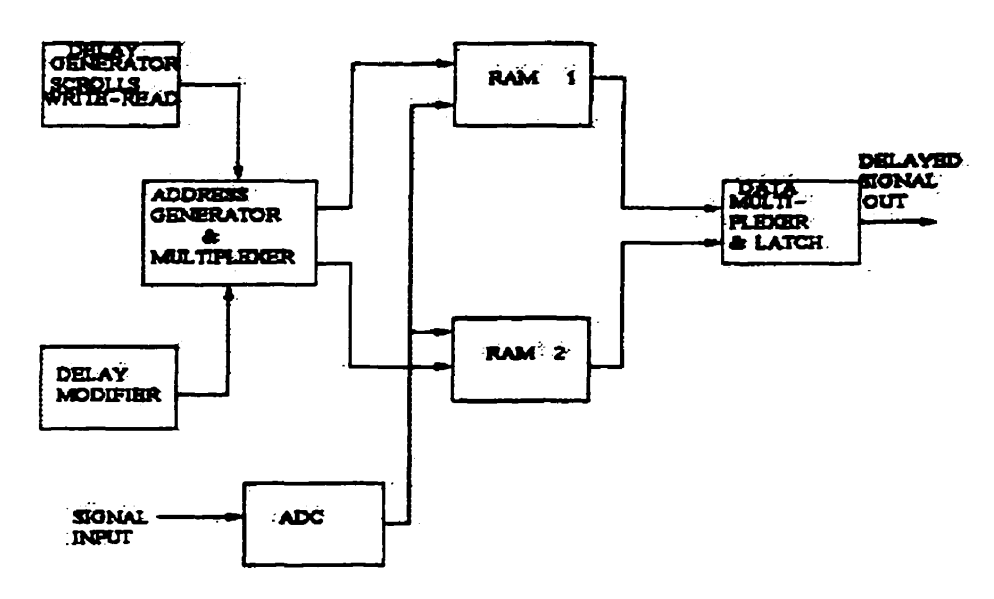
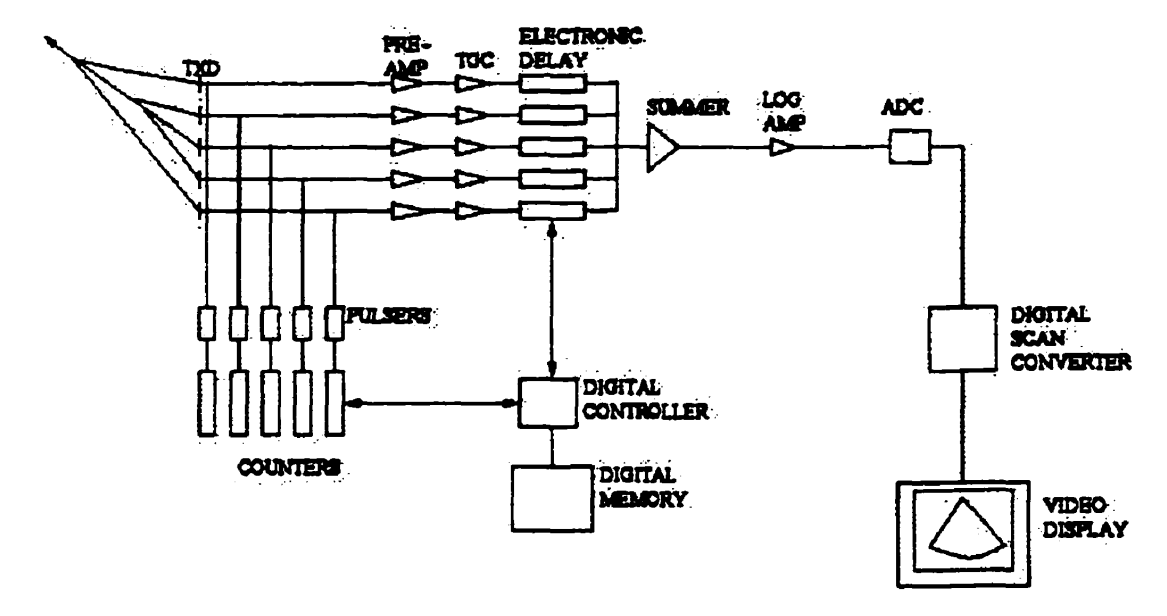


Figure -3.2a Principle of digital delay line



F igure -3.2b Phased array ultrasound system with digital delays

and refinement of IC electronic components made these schemes attractive. Figure 5b shows the general architecture of digital beamformer implemented.

Figure 3.3 is a block diagram of earliest digital system constructed where all analog circuitry is replaced by digital circuitry [20]. In this 16-channel system, the microprocessor controller fixed the times at which each transmitter sends an electrical pulse to its transducer element, to steer the acoustic signal in the desired direction. The echo signals after amplification are digitized and fed to a digital delay circuit consisting of FIFO memory element. The delay in this element was controlled by the microprocessor to provide focusing and steering at the receiver. The signals were then summed together to form the reconstructed image.

One of the major problems in medical ultrasound imaging was the imaging of the dynamic movements of organs such as the heart. The systems that were developed made use of one delay line per channel, providing the required delay in a discrete quasicontinuous manner. Each delay line provided hundreds of delay taps to provide the overall delay. So real-time scanning of the heart required fast switching to continuously track the echoes, which required an especially complex control system and introduced undesirable switching noise. In order to track the variable returning echoes efficiently, novel methods for implementing a programmable delay system were developed [21, 22]. The technique was based on separate and independent processing of the carrier and of the envelope of the echo pulses. Carrier phasing was accomplished by electronic phase-shifters, while delay lines varied the envelope delay. The approach adopted was based on

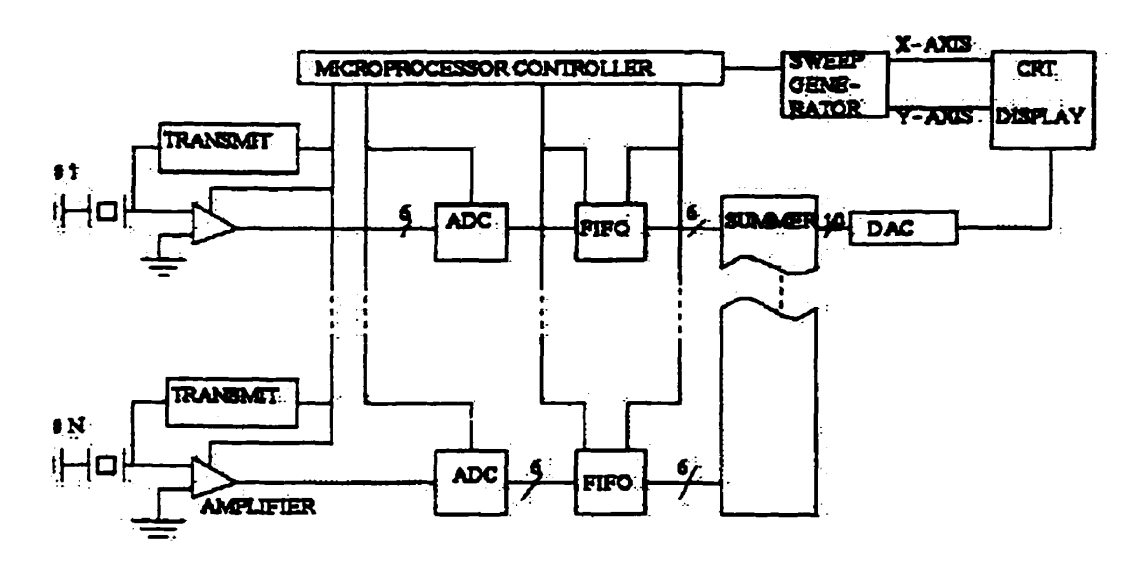


Figure -3.3 Block diagram of the ultrasonic imaging instrument when the analog circuitry is replaced by digital circuitry

mixing the echo with a digitally phase-controlled coherent local oscillator, followed by filtering of the upper or of the lower sideband. Once phase coherence of signals was established, the increment of the delay line required for time-shifting the signal envelope is no longer dependent on the carrier frequency value f_o , but on the extent of signal bandwidth around f_o . This drastically reduced the requirements of the delay line. An important consequence of this new technique was that the signals from all array channels could be processed using one single delay line, rather than a delay line per channel. Figure 3.4 shows the schematic diagram of the simplified system. O'Donnell et.al., [27] proposed a digital beamformer with autonomous channel control in place of the conventional delay and add architecture. The fully digital beamformer used the principle of baseband interpolation. A block diagram of the processing performed on each channel is presented in Figure 3.5. The digital baseband interpolation algorithm uses baseband demodulation followed by low pass filtering and phase rotation to implement the delays. The phase is rotated using a CORDIC processor.

While the earliest commercially available digital beamformers were available in the early 80's, they did not begin to have significant impact until the early 1990's. Much of this delay was due to the need for A/D converters (ADC) with sufficiently large number of bits and a high enough sampling rate for ultrasound signal digitization. This was reflected by the discussion of various designs published in the literature and reviewed above. In the designs discussed above [8, 22], 8-bit A/D converters were used which limited the quantization of delay as well as the pulse fidelity. They tried to overcome this problem by using analog shift registers [8] or by phase shifting [22]. Therefore an obviously

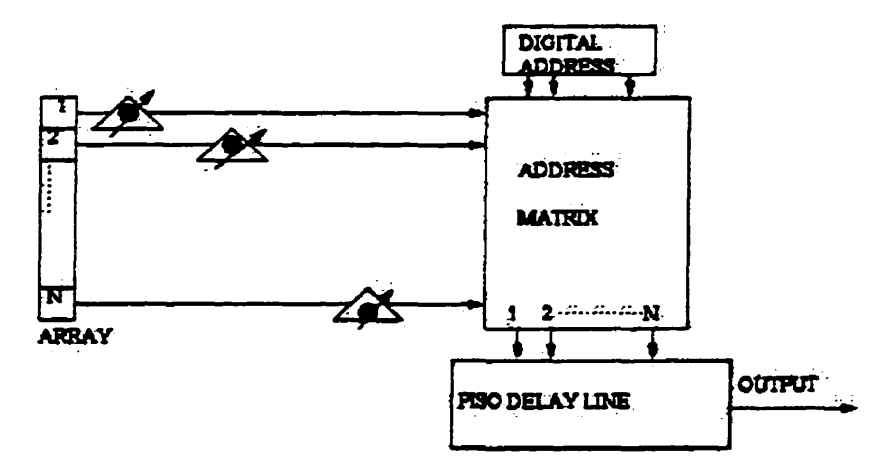


Figure -3.4 Schematic diagram of phased array system using single delay line

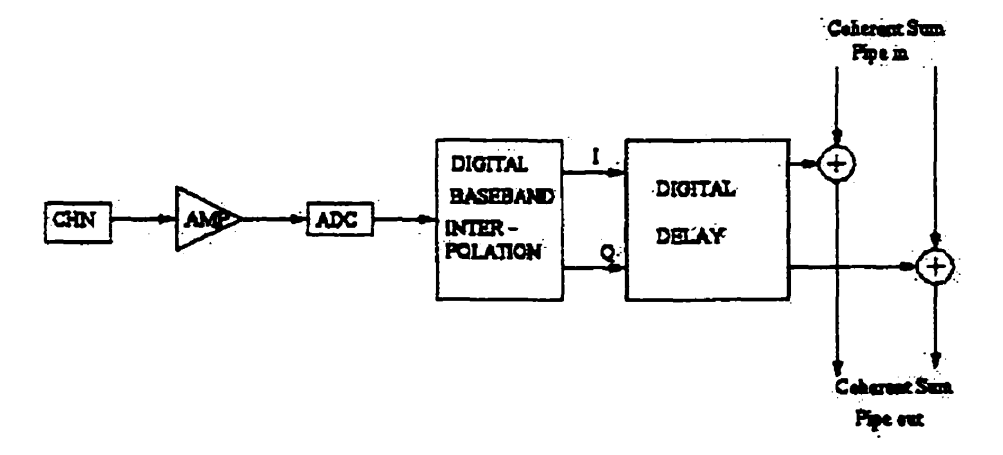


Figure -3.5 Fully digital beamformer using baseband interpolation

important topic is the number of bits required for A/D conversion. The literature does not supply a real answer. Most expressions given are constrained by the assumptions made. Peterson et al. [23] gave the quantization induced sidelobe level as $1/2^B\sqrt{3N}$, while Steinberg [24], who considers the possibility of partial coherence in the quantization noise, describes the same quantity as $-10logN_{eff}$ -6B. In both expressions B is the number of bits, N is the number of processing channels, and N_{eff} is the number of statistically independent channels. Thus B dictates the side lobe level. Higher the number of bits used, lower the side lobe level. This in turn has an effect on the dynamic range. Now 12-bit A/D converters have been developed, thus increasing the dynamic range.

With respect to sampling rate, it is, of course, important to sample at a rate sufficient to capture all of the information in the bandwidth. Once again, there is no consensus in the literature, as to what is the optimum sampling rate. It has been generally agreed that a sampling rate of four to ten times the transducer frequency is required for waveform reconstruction [3, 24, 27]. Earlier it was difficult for ADC's to handle such large frequencies, which led to the development of alternative algorithms for beamforming that required lower sampling rates. The different sampling techniques used were analytic signal sampling, second order sampling, and quadrature sampling [25]. These methods are shown in Figure 3.6. The analytic signal sampling is performed by removing the negative frequency components of the signal with the aid of Hilbert transform. This method is not suitable for ultrasound imaging because it required a Hilbert transformer for each channel. Second-order sampling is an alternative technique that eliminates the need for Hilbert transformer. Second-order sampling yields two sequences of uniformly

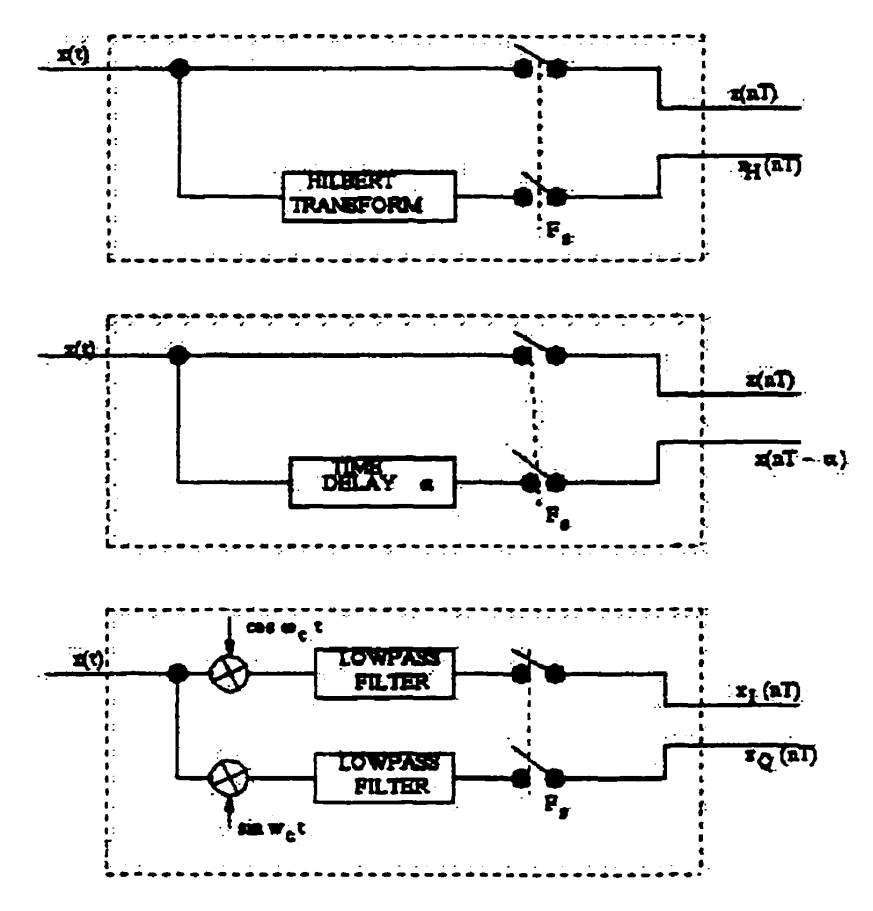


Figure -3.6 Complex sampling procedures: (a) analytic sampling (b) second order sampling and (c) quadrature sampling

spaced samples, which are interleaved. This reduces the sampling rate but requires an ideal bandpass filter with relatively complex frequency transfer characteristics. Quadrature sampling characterizes a bandpass signal with uniformly spaced samples of its quadrature components. However this method has poor resolution and also has higher hardware requirements like two low pass filters, phase shifters and adders for each channel. Table 3.1 shows comparison of various sampling techniques.

To reduce the sampling rate alternative beamforming algorithms have been created [5, 26]. Song, K. T. et al. [5] have proposed a modified second order and quadrature sampling to overcome some of the problems in conventional sampling methods. These methods used fewer ADC's. Figure 3.7 is the schematic representations of these methods. Cho et al. [26] proposed multi order sampling to further reduce the errors in sampling. This method uses two pieces of data for quadrature component and yields a large SNR. Figure 3.8 shows a digital beamformer with multi-order sampling.

Table -2 Comparison of various sampling techniques

Type of sampling	Sampling rate	Hardware complexity	Detection error
Uniform sampling	$f_s > 2f_o + B$	lowest	large
Quadrature sampling	$f_s > B$	very high	no
2 nd order sampling	$f_s > lf_o > B$ l = 1, 2,	high	Q independent
Modified quadrature sampling	$f_o < f_s < 2f_o - B$ (Q > 1.5)	low	no
Multi-rate sampling	$n/f_s + a < f_s < n/f_s + a$	low	no

In these implementations, the two parameters of the ADC, i.e. the number of bits and sampling rate, cannot be optimized simultaneously. Generally, there is a direct trade-off between the sampling rate of the ADC and dynamic range achievable. Most of the

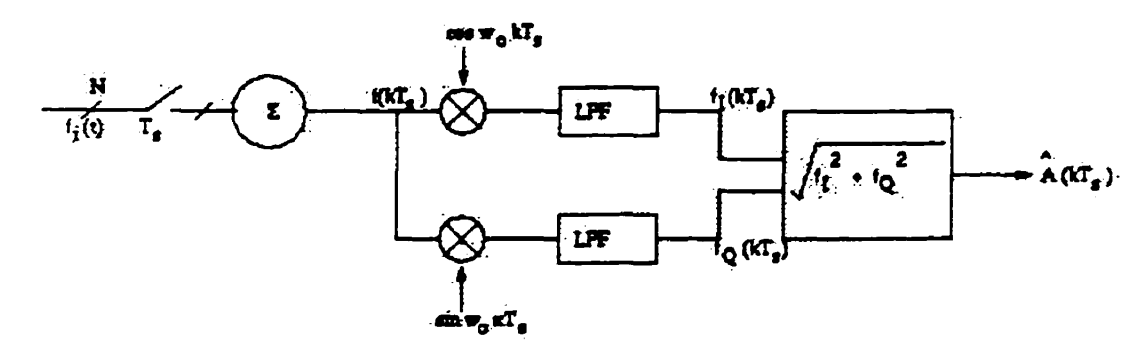


Figure - 3.7 Schematic diagram of modified quadrature sampling method

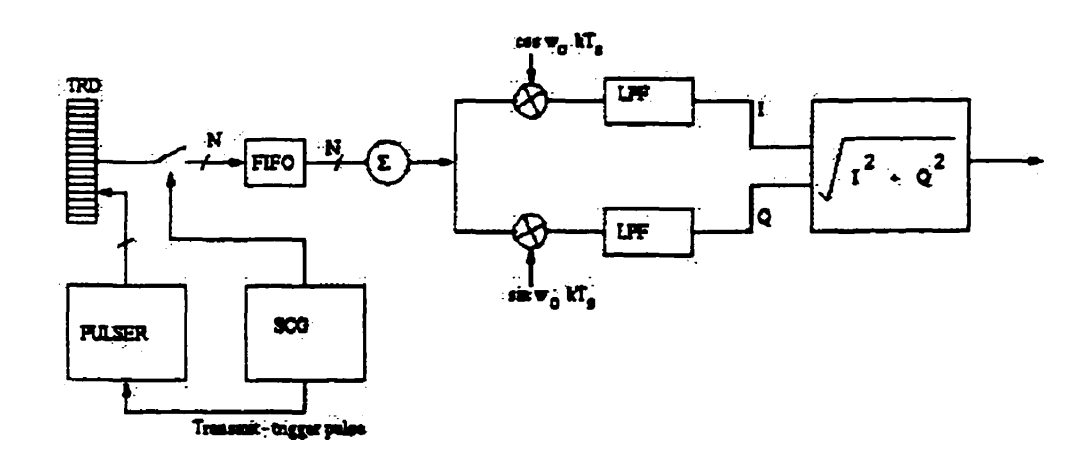


Figure -3.8 Schematic diagram of a digital beamformer with multi-order sampling

commercially available converters are either, low speed and high resolution or high speed and low resolution. Parallel or "flash" converters have the highest speeds (over 50 MHz), but their complexity grows rapidly with increasing resolution. In practice, the optimum performance from a speed and resolution point of view is obtained by using two-stage parallel converters. This type of converter achieves a reduction in circuit complexity at the expense of sampling speed and has speed/resolution parameters better suited to digital ultrasonic imaging. A recently introduced two-stage converter has twelve bit resolution at a 10 MHz sampling rate [3].

While the implementations of digital beamformers reviewed above have been of the basic delay-and-sum kind, lately there has been a considerable shift to a more complex beamforming method, synthetic aperture imaging. The concept of synthetic aperture focusing can be traced back to the early 1950's in radar applications. Rapid developments in digital computing made it possible to apply the principles to digitized ultrasonic signals. The application of the method to ultrasonic beamforming was first proposed by Johnson et al., 1975 [28]. A synthetic aperture image is formed by exciting the transmit elements individually. The receive beams necessary to fill a sector scan are formed simultaneously. The final image formed is the sum of the beamformed energy from each transmit burst.

Several different ways of implementing the synthetic aperture technique have been published in the literature. Of these, the synthetic aperture focusing technique (SAFT) appears to be the popular method. The first real-time SAFT imaging system was

developed by a Stanford University group [29]. The system viewed a fixed field with a 32-transducer array with a focus table for each pixel. To overcome the drawbacks of earlier methods, new techniques were developed. Ozaki et al. [29] designed a new imaging ultrasonic imaging system that used a single transducer, which moved linearly on an object surface, transmitting a spatially wide beam into the object and receiving the returning echoes at a constant spatial interval. The received signal are then digitized and stored in a FIFO memory. An A-scan line was calculated using the signal data present in the memory and transferred to a display unit, and then the transducer is moved to the next measurement point. Figure 3.9 shows the principle of image reconstruction in SAFT. Another technique called the synthetic receive aperture technique was developed by Nock and Trahey [30]. This imaging system addressed a very large number of receive elements using a smaller number of parallel receive channels. Figure 3.10 shows the architecture of the receiver part of a SRA imaging system. In order to form each line of data, the transmitters were fired once for each receive subaperture. After the signals were acquired from each subaperture, the final signal is formed by adding the sum from various subapertures. This technique was much simpler in terms of digital memory and computations required. It also improved the resolution with a comparatively cheaper architecture.

The synthetic focusing techniques discussed so far employed only one-way dynamic focusing (during reception). Ylitalo [31] proposed a novel Fourier-domain synthetic aperture ultrasound imaging employing a curved array. The new approach achieved two-way focusing using simple hardware. The effective aperture had a size double that of the

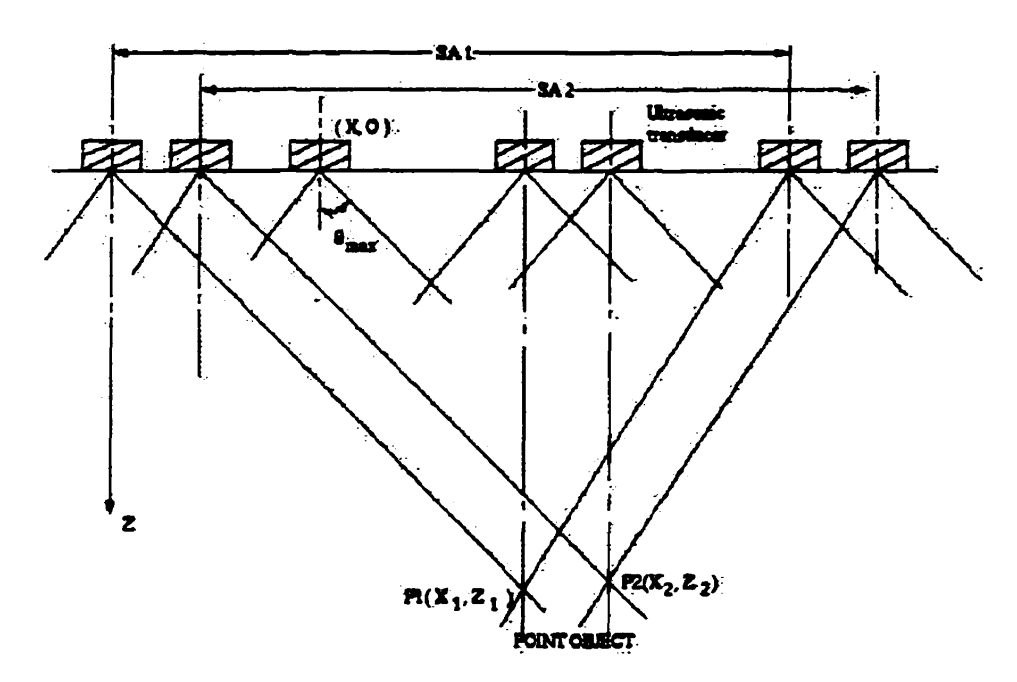


Figure - 3.9 Principle of image reconstruction in SAFT

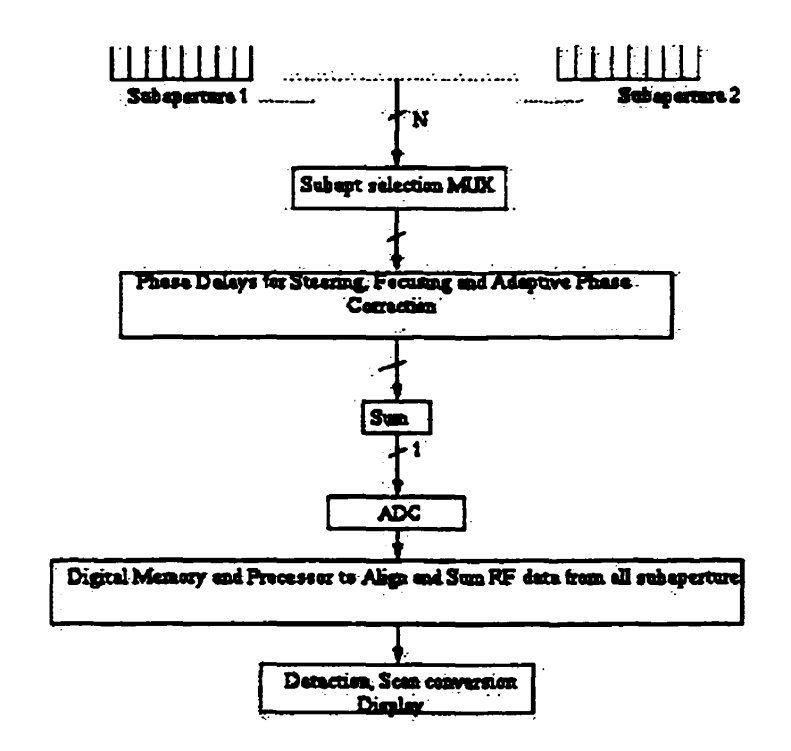


Figure -3.10 Architecture of a Synthetic Receive System (SRA)

phased array technique. Synthetic focusing is achieved through Fourier-domain processing.

Synthetic aperture systems are sensitive to motion artifacts due to phase distortions. But phase correction for both motion and tissue inhomogeneities can be performed in a single compensation procedure. Many beamforming algorithms have been developed to reduce motion artifacts due to phase distortion [29, 34].

A new method called multi-element synthetic aperture focusing (M-SAF), which dramatically reduces the size and cost of low channel count systems was developed by O'Donnell et al. [34]. Figure 3.11 shows the data acquisition strategies. This method uses spatial frequencies corresponding to receive, transmit combination. The subapertures are then stepped across the array one element at a time with coincident transmit and receive subapertures.

Thus the flexibility of digital beamformers permits novel beamforming methods to be developed and exploited. These areas are still under development and have begun to enter commercial machines

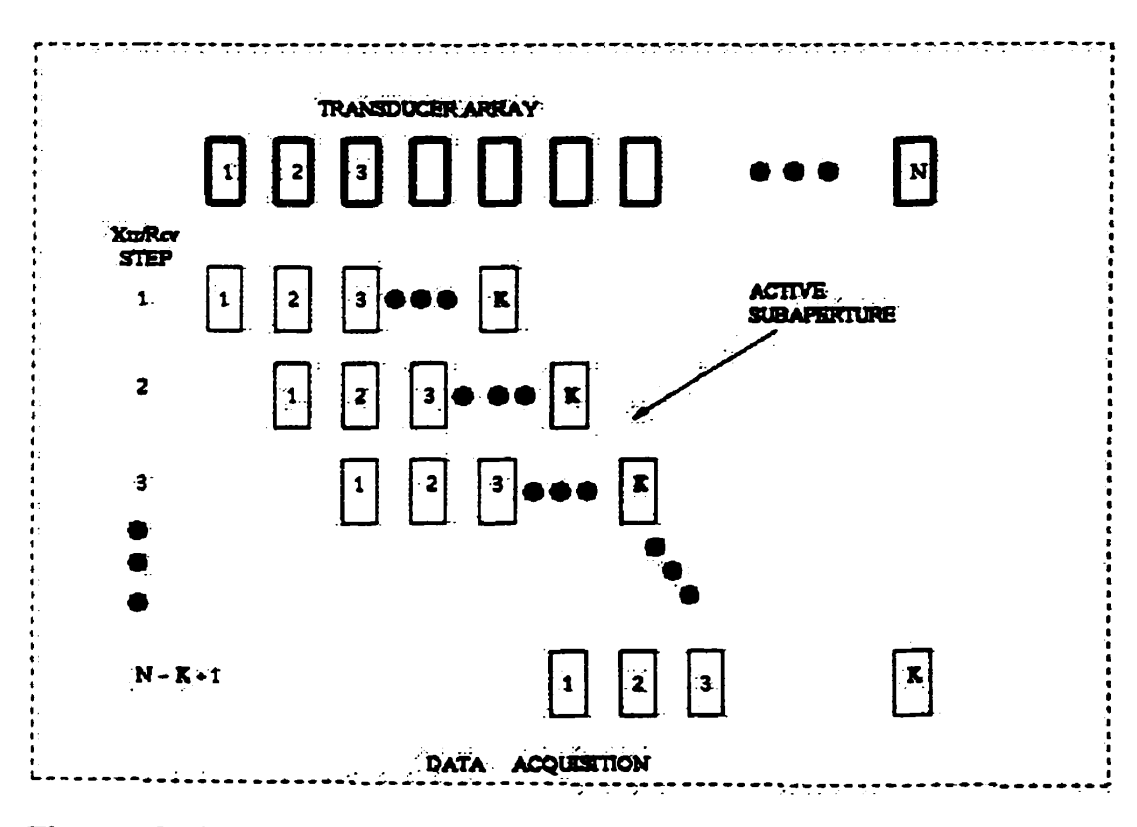


Figure -3.11 Data acquisition strategy for M-SAF

4. Aperture Theory and Far Field Directivity Functions.

"Aperture" in acoustics is used to refer to either a single electroacoustic transducer or an array of electroacoustic transducers. The complex aperture function, that is, the magnitude and phase of the sound distribution within the aperture, determines the Fresnel and Fraunhofer diffraction patterns of the aperture, which in turn determines the beam profile of a transducer element. The basic equations that are derived from complex aperture theory are used to describe the performance of a single transducer and an array of transducers. The derivations below are not presented in their entirety. These basic equations are used in the simulations carried out in this thesis.

The far-field and the near-field criterion are given by the following two equation [35]:

$$r > \pi R^2 / \lambda > 1.356R \tag{4.1}$$

$$1.356R < r < \pi R^2 / \lambda \tag{4.2}$$

where,

$$r = \sqrt{x^2 + y^2 + z^2}$$

is the magnitude of the position vector to a field point and R is the maximum range.

The far field directivity function of a general volume aperture is given by

$$D(f,s) = F_{r_a} \{ A(f,r_a) \} = \int_{-\infty}^{\infty} A(f,r_a) \exp(+j2\pi s \cdot r_a) dr_a, \qquad (4.3)$$

where

$$\mathbf{r}_a = (\mathbf{x}_a, \mathbf{y}_a, \mathbf{z}_a).$$

 $s = (f_X, f_Y, f_Z)$, are the spatial frquencies.

and $dr_a = dx_a dy_a dz_a$. Note that the complex aperture function can be expressed as

$$A(f,r_a) = a(f,r_a) \exp[+j\theta(f,r_a)], \tag{4.4}$$

where $a(f,r_a)$ is the amplitude and $\theta(f,r_a)$ is the phase of the response at spatial location r_a of the aperture. Both $a(f,r_a)$ and $\theta(f,r_a)$ are real functions. The function $a(f,r_a)$ is also known as the amplitude window.

4.1 Linear Apertures

A linear aperture represents a single transducer of length L meters where the phase response of the transducer is zero, that is,

$$A(f, x_a) = a(f, x_a), \qquad \theta(f, x_a) = 0$$
 (4.5)

Now consider the case of a linear aperture of length L meters lying along the X axis as shown in Figure 4.1. Also shown in the figure is a field point with spherical coordinates (r,θ,ψ) . The field point is assumed to be in the far field region of the aperture given by Eq. (4.1), where R=L/2 meters is the maximum radial extent of the aperture.

The position vector describing the spatial location of the aperture is given by

$$r_a = (x_a, 0, 0),$$

and as a result,

$$A(f,r_a) = A(f,x_a), \tag{4.6}$$

$$s \bullet r_a = (f_X, f_Y, f_Z) \bullet (x_a, 0, 0) = f_X x_a,$$
 (4.7)

and

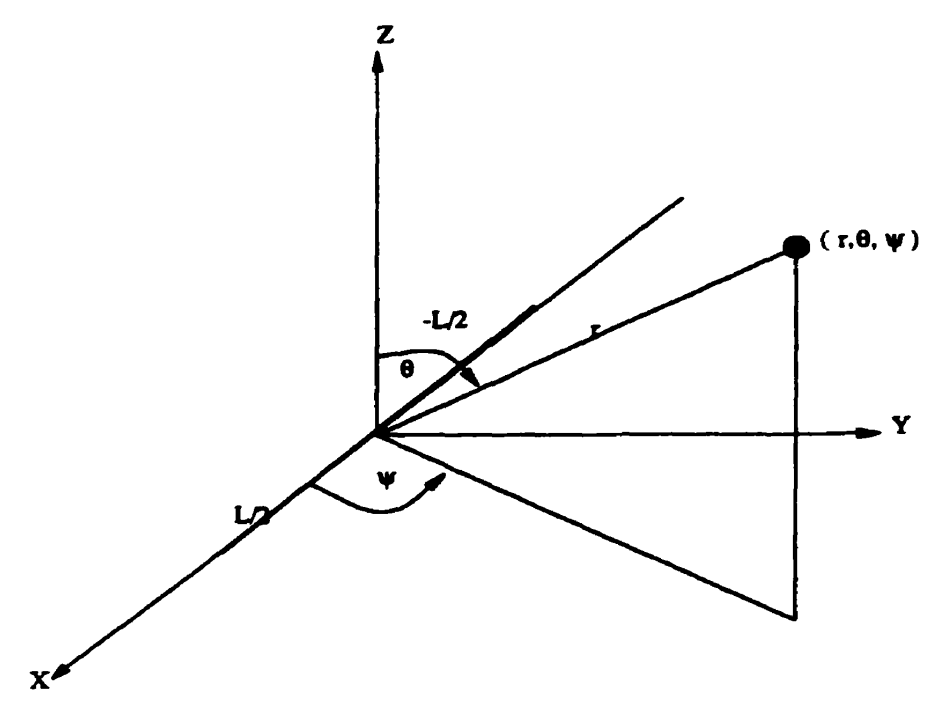


Figure -4.1 Linear aperture of length L meters lying along the X-axis. Also shown is a field point with spherical coordinates (r, θ, ψ) .

$$d\mathbf{r}_a = d\mathbf{x}_a \tag{4.8}$$

Therefore, upon substituting Eqs. (4.6) through (4.8) into Eq. (4.3), we obtain the expression for the beam pattern of a linear aperture:

$$D\left(\frac{\sin\theta}{\lambda}\right) = F_{x_a}\left\{A(f,x_a)\right\} = \int_{-L/2}^{L/2} A(f,x_a) \exp(+j2\pi\left(\frac{\sin\theta}{\lambda}\right)x_a) dx_a, \quad (4.9)$$

where

$$A(f,x_a) = a(f,x_a)\exp[+j\theta(f,x_a)] \tag{4.10}$$

Equation (4.9) is the directivity function of the aperture.

4.2 Amplitude Windows

To determine the far-field beam pattern, beamwidth, and the relationship between beamwidth and sidelobe levels of far-field beam patterns, the elements are windowed i.e. each element are given a 'weight', thus controlling the transducer reponse. This is called apodization and is implemented with help of amplitude windows which are discussed next.

A. The rectangular amplitude window

The rectangular amplitude window is defined as follows:

$$rect(x/L) = \begin{cases} 1, |x| \le L/2. \\ 0, |x| > L/2. \end{cases}$$
 (4.11)

The amplitude of the complex frequency response of the transducer is constant along the length L of the transducer, regardless of the magnitude of frequency f with zero phase (Figure 4.2).

Therefore,

$$A(f,x_a) = a(f,x_a) = rect(x_a/L)$$
(4.12)

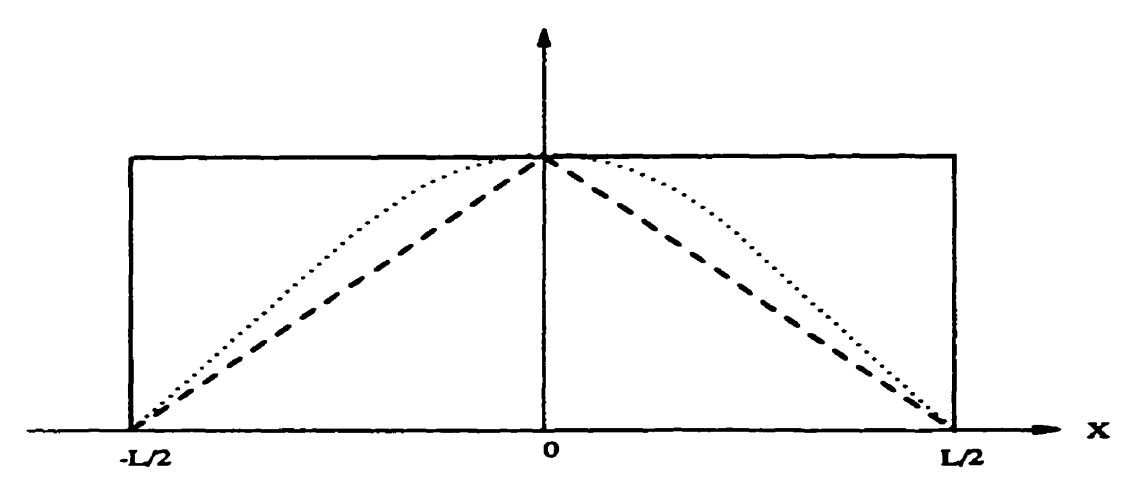


Figure-4.2 Rectangular (solid), triangular (dash) and hanning (dot) amplitude windows.

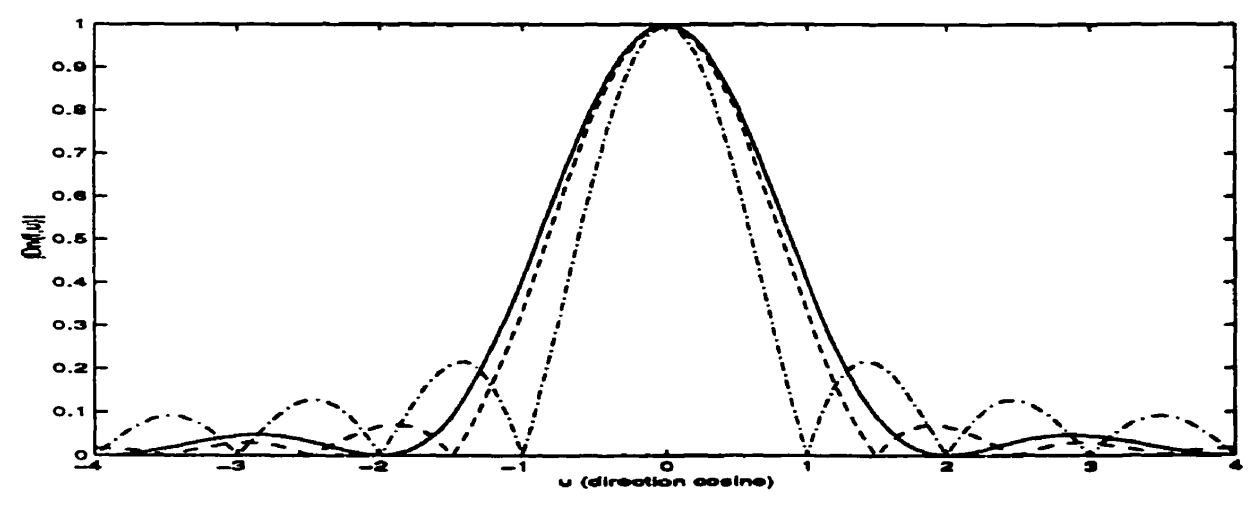


Figure-4.3. Magnitude of the normalized far-field beam patterns of the rectangular amplitude window (dashed curve), triangular amplitude window (solid curve), and hanning amplitude window (dot-dash curve) plotted as a function of direction cosine u.

Substituting Eqs. (4.12) and (4.11) into Eq. (4.9) yields

$$D\left(\frac{\sin\theta}{\lambda}\right) = F_{x_a}\left\{rect(x_a/L)\right\} = \int_{-L/2}^{L/2} \exp(+j2\pi\left(\frac{\sin\theta}{\lambda}\right)x_a)dx_a, \tag{4.13}$$

or

$$D\left(\frac{\sin\theta}{\lambda}\right) = F_{x_a}\left\{rect(x_a/L)\right\} = L\sin c\left(\frac{\sin\theta}{\lambda}\right)L$$
 (4.14)

where

$$\sin c(x) = \frac{\sin(\pi x)}{\pi x}. (4.15)$$

The normalized far-field directivity function is defined as follows:

$$D_{N} \left(\frac{\sin \theta}{\lambda} \right) = \frac{D \left(\frac{\sin \theta}{\lambda} \right)}{D_{\text{max}}} \tag{4.16}$$

$$D_N\left(\frac{\sin\theta}{\lambda}\right) = \sin c\left(\frac{\sin\theta}{\lambda}\right)L. \tag{4.17}$$

B. The triangular amplitude window

The triangular amplitude window is defined as follows:

$$tri(x/L) = \begin{cases} 1 - \frac{|x|}{L/2}, |x| \le \frac{L}{2}, \\ 0, |x| > \frac{L}{2} \end{cases}$$
 (4.18)

The amplitude of the complex frequency response of the transducer is triangular in shape along the length L of the transducer irrespective of the magnitude of frequency f. Also the phase of the complex frequency response is zero (Figure 4.2). Therefore,

$$A(f, x_a) = a(f, x_a) = tri(x_a/L),$$
 (4.19)

Substituting Eqs. (4.22) and (4.21) in Eq. (4.9) yields

$$D\left(\frac{\sin\theta}{\lambda}\right) = F_{x_a}\left\{rri(x_a/L)\right\} = \int_{-L/2}^{L/2} 1 - \frac{|x_a|}{L/2} \exp(+j2\pi\left(\frac{\sin\theta}{\lambda}\right)x_a)dx_a, \quad (4.20)$$

or

$$D\left(\frac{\sin\theta}{\lambda}\right) = F_{x_a}\left\{tri(x_a/L)\right\} = \frac{L}{2}\sin c^2\left(\frac{\sin\theta}{\lambda}\right)L$$
(4.21)

Referring to Eq. (4.16), the normalization factor is given by

$$D_{\max} = D(f,0) = L/2, \tag{4.22}$$

since sinc(0) = 1 is the maximum value of the sinc function. Substituting Eqs. (4.21) and (4.22) into Eq. (4.16) results in the expression for the normalized far-field beam pattern of the triangular amplitude window:

$$D_N\left(\frac{\sin\theta}{\lambda}\right) = \sin c^2\left(\left(\frac{\sin\theta}{\lambda}\right)L/2\right). \tag{4.23}$$

C. The hanning amplitude window

The hanning amplitude window is given by

$$a(f,x_a) = \cos^2(\pi x_a/L)rect(x_a/L). \tag{4.24}$$

The final expression for the far-field directivity function for a hanning amplitude window can be found from Equations (6.3-65) and (6.3-66) in Ziomek [35] and is given by

$$D\left(\frac{\sin\theta}{\lambda}\right) = F_{x_a} \left\{\cos^2(\pi x_a/L)rect(x_a/L)\right\}$$

$$= \frac{L}{2} \left\{\sin c^2 \left[\left(\left(\frac{\sin\theta}{\lambda}\right) + \frac{1}{2L}\right)L \right] + \sin c^2 \left[\left(\left(\frac{\sin\theta}{\lambda}\right) - \frac{1}{2L}\right)L \right] \right\}. (4.25)$$

$$D\left(\frac{\sin\theta}{\lambda}\right) = F_{x_a} \left\{\cos^2(\pi x_a/L)rect(x_a/L)\right\} = ,$$

$$0.5L \sin c \left(\frac{\sin\theta}{\lambda}L\right) + 0.5F_{x_a} \left\{\cos(2\pi x_a/L)rect(x_a/L)\right\}$$
(4.26)

which is the unnormalized far-field beam pattern of the hanning amplitude window.

Referring to Eq. (4.26), the normalization factor is given by

$$D_{\max} = D(f,0) = L/\pi. \tag{4.27}$$

Substituting Eqs. (4.25) and (4.26) into Eq. (4.16) results in the normalized far-field beam pattern of the hanning amplitude window (see Figure 4.2):

$$D_{N}\left(\frac{\sin\theta}{\lambda}\right) = \frac{\cos(2\pi\left(\frac{\sin\theta}{\lambda}\right)L)}{1 - \left(2\left(\frac{\sin\theta}{\lambda}\right)L\right)^{2}},\tag{4.28}$$

Looking at the plots for the normalized far-field beam pattern of the various amplitude windows discussed above (Figure 4.3), one sees that the first sidelobe level of the hanning amplitude window is approximately -23 dB, while the sidelobe levels for the rectangular and triangular amplitude windows are approximately -13 and -27 dB, respectively. This can be attributed to the way the windows approaches zero at the end points $x = \pm L/2$. The triangular window approaches zero in a comparatively smooth fashion i.e. with a smaller slope than the other two amplitude windows and hence has lower sidelobe levels. A reduction in sidelobe levels results in a wider main lobe; see Figure 4.3. Figures 4.4, 4.5 and 4.6 shows the polar plots of normalized far-field beam patterns for the amplitude windows discussed, as given by Equations (4.17), (4.23) and

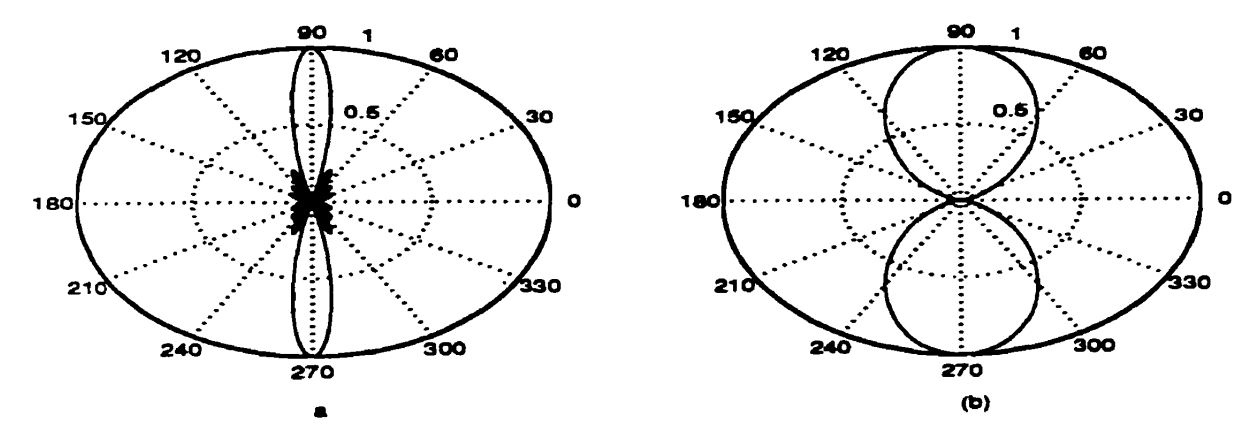


Figure -4.4 Polar plot of the magnitude of the normalized horizontal far-field beam pattern of the rectangular amplitude window for (a) $L/\lambda = 4$, (b) $L/\lambda = 2$.

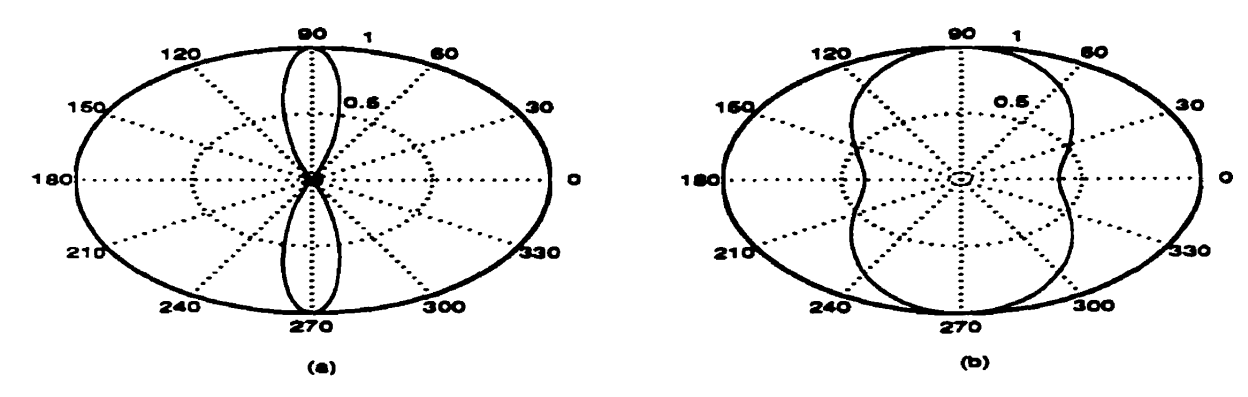


Figure -4.5 Polar plot of the magnitude of the normalized horizontal far-field beam pattern of the triangular amplitude window for (a) $L/\lambda = 4$, (b) $L/\lambda = 2$.

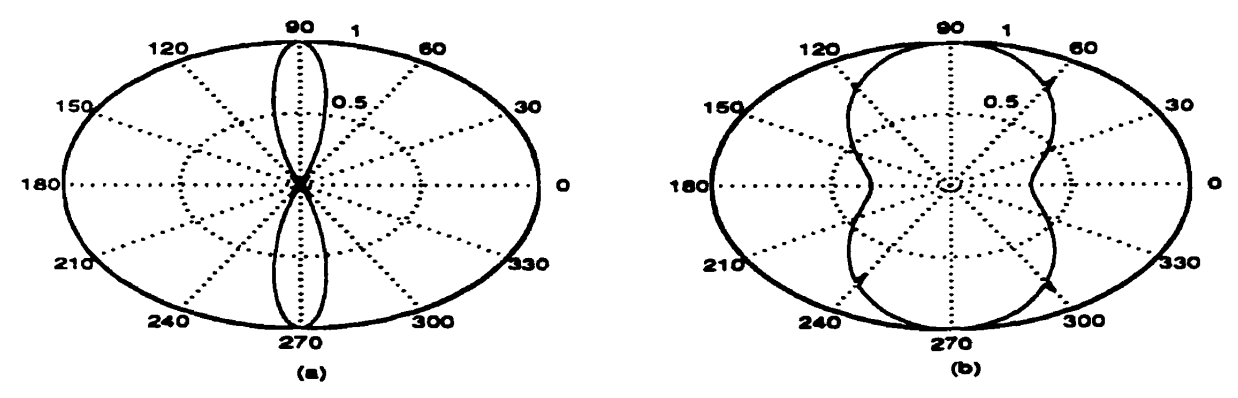


Figure -4.6 Polar plot of the magnitude of the normalized horizontal far-field beam pattern of the hanning amplitude window for (a) $L/\lambda = 4$, (b) $L/\lambda = 2$.

the plots, the main lobe width is dependent on the aperture length and wavelength. The beam width is directly proportional to the wavelength λ and inversely proportional to the length L of the aperture. The figures shows the beam patterns for two different ratios of L/λ .

4.3 BEAM STEERING AND FOCUSING.

We now examine the far-field beam pattern when the phase response $\theta(f,x_a)$ is nonzero.

We express $\theta(f, x_a)$ in terms of the following polynomial:

$$\theta(f, x_a) = \theta_0(f) + \theta_1(f)x_a + \theta_2(f)x_a^2 + \dots + \theta_N(f)x_a^N, \tag{4.29}$$

where $\theta_o(f)$ represents a constant value of phase across the aperture, $\theta_1(f)$ x_a is the linear phase variation across the aperture and is responsible for beam steering. $\theta_2(f)x_a^2$ is the quadratic phase variation across the aperture and is responsible for focusing in the Fresnel zone.

Now let $D\left(\frac{\sin\theta}{\lambda}\right)$ be the far-field beam pattern of the amplitude window $a(f, x_a)$, that is,

$$D\left(\frac{\sin\theta}{\lambda}\right) = F_{x_a}\left\{a(f,x_a)\right\} = \int_{-\infty}^{\infty} a(f,x_a)\exp(+j2\pi\left(\frac{\sin\theta}{\lambda}\right)x_a)dx_a, \quad (4.30)$$

and let $D\left(\frac{\sin\theta}{\lambda}\right)$ be the far-field beam pattern of the aperture function $A(f, x_a)$ given by,

$$D\left(\frac{\sin\theta}{\lambda}\right) = F_{x_a}\left\{a(f,x_a)\exp[+j\theta(f,x_a)]\right\}$$

$$= \int_{-\infty}^{\infty} a(f,x_a)\exp[+j\theta(f,x_a)]\exp(+j2\pi\left(\frac{\sin\theta}{\lambda}\right)x_a)dx_a. \quad (4.31)$$

Now, assume that the phase response across the aperture is a linear function of x_a , that is,

$$\theta(f, x_a) = \theta_1(f)x_a, \tag{4.32}$$

If Eq. (4.32) are substituted into Eq. (4.31), then

$$D'\left(\frac{\sin\theta}{\lambda}\right) = F_{x_a}\left\{a(f,x_a)\exp(-j2\pi\left(\frac{\sin\theta'}{\lambda}\right)x_a)\right\}$$

$$= \int_{-\pi}^{\pi} a(f,x_a)\exp[+j2\pi\left(\frac{\sin\theta}{\lambda}\right) - \left(\frac{\sin\theta'}{\lambda}\right)x_a\right]dx_a, \qquad (4.33)$$

therefore,

$$D\left(\frac{\sin\theta}{\lambda}\right) = D\left(\left(\frac{\sin\theta}{\lambda}\right) - \left(\frac{\sin\theta'}{\lambda}\right)\right) \tag{4.34}$$

Therefore, a linear phase response across the length of the aperture will cause the beam pattern $D\left(\frac{\sin \theta}{\lambda}\right)$ to be steered in the direction $\theta = \theta'$.

4.4 ARRAYS

An array can be thought of as a *sampled aperture*, consisting of individual electroacoustic transducers called elements.

Consider a linear array composed of an even number of elements lying along the X axis.

If the each element is not identical; has a different complex frequency response, and is

not equally spaced relative to adjacent elements, then the complex frequency response of this array according to Ziomek [35] can be expressed as

$$A(f, x_a) = \sum_{n=-N/2}^{-1} b_n(f) e_n(f, x_a - x_n) + \sum_{n=1}^{N/2} b_n(f) e_n(f, x_a - x_n)$$
 (4.35)

OF

$$A(f,x_a) = \sum_{n=1}^{N/2} [b_{-n}(f)e_{-n}(f,x_a - x_{-n}) + b_n(f)e_n(f,x_a - x_n)], \qquad (4.36)$$

where N is the total even number of elements, x_n is the x coordinate of the center of element n, $b_n(f)$ is the frequency dependent complex weight associated with element n, and $e_n(f, x_a)$ is the complex frequency response of element n, also known as the element function.

Eq. (4.35) indicates that the complex frequency response of the array is equal to the linear superposition of the complex weighted frequency responses of all individual elements in the array. The complex weights are used to control the complex frequency response of the array and therefore, the array's far-field directivity function by amplitude and phase weighting.

a) Even number of elements

The expression for the far-field beam pattern can be expressed as:

$$D\left(\frac{\sin\theta}{\lambda}\right) = \sum_{n=1}^{N/2} \begin{bmatrix} b_{-n}(f)E_{-n}\left(\frac{\sin\theta}{\lambda}\right)\exp(+j2\pi\left(\frac{\sin\theta}{\lambda}\right)x_{-n}) \\ +b_{n}(f)E_{n}\left(\frac{\sin\theta}{\lambda}\right)\exp(+j2\pi\left(\frac{\sin\theta}{\lambda}\right)x_{n}) \end{bmatrix}$$
(4.37)

If all the elements in the array are identical, but still not equally spaced, then Eq. (4.37) reduces to

$$D\left(\frac{\sin\theta}{\lambda}\right) = E\left(\frac{\sin\theta}{\lambda}\right) \bullet O\left(\frac{\sin\theta}{\lambda}\right)$$

(4.38)

where

$$E\left(\frac{\sin\theta}{\lambda}\right) = F_{x_a}\left\{e(f, x_a)\right\} \tag{4.39}$$

is the far field beam pattern of one of the identical elements in the array and for N even,

$$O\left(\frac{\sin\theta}{\lambda}\right) = \sum_{n=1}^{N/2} \left[b_{-n}(f) \exp(+j2\pi \left(\frac{\sin\theta}{\lambda}\right) x_{-n}) + b_{n}(f) \exp(+j2\pi \left(\frac{\sin\theta}{\lambda}\right) x_{n}) \right]$$
(4.40)

Equation (4.40) is referred to as the *product theorem* for linear arrays. It states that the far-field directivity function $D\left(\frac{\sin\theta}{\lambda}\right)$ of a linear array of identical, complex weighted elements is equal to the product of the far-field directivity of one of the identical elements in the array, and the far-field directivity function of an equivalent linear array of identical, complex-weighted, omnidirectional point elements.

Finally, if all the elements in the array are equally spaced, then

$$x_n = (n - 0.5)d,$$
 $n = 1,2,...,N/2,$ (4.41)

and

$$x_{-n} = -x_n,$$
 $n = 1, 2, ..., N/2,$ (4.42)

where d is the interelement spacing in meters.

b) Odd Number of Elements.

Now consider a linear array composed of an odd number of unequally spaced elements with different complex frequency responses lying along the X axis. Using the principle of superposition, the complex frequency response of this array can be expressed as

$$A(f,x_a) = \sum_{n=-N}^{N} c_n(f) e_n(f,x_a - x_n), \tag{4.43}$$

where

$$N' = (N-1)/2, (4.44)$$

N is the total odd number of elements, x_n is the x coordinate of the center of element n, and $x_0 = 0$, since one element is centered at the origin of the array.

Therefore the far field beam pattern is given by,

$$D\left(\frac{\sin\theta}{\lambda}\right) = \sum_{n=-N}^{N} b_n(f) E_n\left(\frac{\sin\theta}{\lambda}\right) \exp(+j2\pi\left(\frac{\sin\theta}{\lambda}\right) x_n), \tag{4.45}$$

where $E_n\left(\frac{\sin\theta}{\lambda}\right)$ is the far-field beam pattern of element n.

If all the elements in the array are identical, but still not equally spaced, then Eq.(4.45) reduces to:

$$D\left(\frac{\sin\theta}{\lambda}\right) = E\left(\frac{\sin\theta}{\lambda}\right) p\left(\frac{\sin\theta}{\lambda}\right) \tag{4.46}$$

where $E\left(\frac{\sin \theta}{\lambda}\right)$ is the far field beam pattern of one of the identical elements in the array,

and for N odd, the far-field beam pattern of an equivalent linear array of identical, complex-weighted, omnidirectional point elements is given by

$$O\left(\frac{\sin\theta}{\lambda}\right) = \sum_{n=-N}^{N} b_n(f) \exp(+j2\pi \left(\frac{\sin\theta}{\lambda}\right) x_n), \tag{4.47}$$

where N' is given by Eq. (4.44).

Finally, if all the elements in the array are equally spaced, then

$$x_n = nd, n = -N', \dots 0, \dots, N' (4.48)$$

4.4a The Phased Array (Beam Steering)

Consider a linear array of N (odd) identical, equally spaced, complex weighted, omnidirectional point elements lying along the X axis. The far-field directivity function of this array is given by

$$D\left(\frac{\sin\theta}{\lambda}\right) = O\left(\frac{\sin\theta}{\lambda}\right) = \sum_{n=-N}^{N} b_n(f) \exp(+j2\pi \left(\frac{\sin\theta}{\lambda}\right) nd), \tag{4.49}$$

since $E\left(\frac{\sin\theta}{\lambda}\right) = 1$ for an omnidirectional point element.

Now let $D\left(\frac{\sin\theta}{\lambda}\right)$ be the far-field beam pattern of the array when it is only amplitude

weighted, and let $D\left(\frac{\sin \theta}{\lambda}\right)$ be the far field beam pattern of the array when it is complex

weighted; that is,

$$D\left(\frac{\sin\theta}{\lambda}\right) = \sum_{n=-N}^{N} a_n(f) \exp(+j2\pi \left(\frac{\sin\theta}{\lambda}\right) nd)$$
 (4.50)

and

$$D'\left(\frac{\sin\theta}{\lambda}\right) = \sum_{n=-N'}^{N'} a_n(f) \exp\left[+j\left[2\pi\left(\frac{\sin\theta}{\lambda}\right)nd + \theta_n(f)\right]\right]$$
(4.51)

If the phase weights are given by

$$\theta_n(f) = -2\pi \left(\frac{\sin \theta'}{\lambda}\right) nd, \qquad n = -N', \dots, 0, \dots, N', \qquad (4.52)$$

Now substituting Eq. (4.52) into Eq. (4.51) yields

$$D\left(\frac{\sin\theta}{\lambda}\right) = \sum_{n=-N'}^{N'} a_n(f) \exp\left[+j2\pi\left(\frac{\sin\theta}{\lambda}\right) - \left(\frac{\sin\theta'}{\lambda}\right)nd\right],\tag{4.53}$$

or

$$D\left(\frac{\sin\theta}{\lambda}\right) = D\left(\frac{\sin\theta'}{\lambda}\right) - \left(\frac{\sin\theta'}{\lambda}\right),\tag{4.54}$$

Therefore, a linear phase variation applied across the length of the array will cause the beam pattern $D\left(\frac{\sin\theta}{\lambda}\right)$ to be steered in the direction $\theta=\theta'$, which is equivalent to steering the beam pattern to $\theta=\theta'$. Figures 4.7, 4.8 and 4.9 are polar plots of the magnitude of the normalized horizontal far field patterns for rectangular, triangular and hanning apodizations respectively, of a linear array of N=7 elements, equally spaced for beam tilt angles of $\theta=45$ and $\theta=0$ degrees. The figures show that steering of beam from the axis causes grating lobes to appear. The grating lobes are more pronounced when the inter-element spacing is greater than $\lambda/2$, where λ is the wavelength associated with the transducer array [35]. While rectangular apodization has the minimum beam width, but has the highest side lobe levels when compared with triangular and hanning apodization for both cases of steering.

Finally, the phase shift $\theta_n(f)$ in radians is equivalent to a time delay τ_n in seconds, that is,

$$\theta_n(f) = 2\pi f \tau_n, \tag{4.55}$$

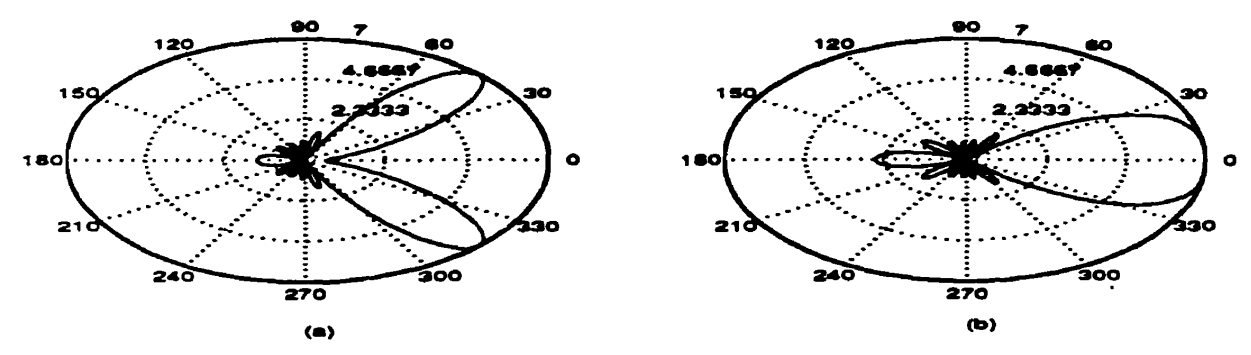


Figure -4.7 Polar plot of the magnitude of the normalized horizontal far-field beam pattern of a linear array with rectangular apodization for a beam tilt angle of (a) $\theta = 45^{\circ}$, (b) $\theta = 0^{\circ}$ and $d/\lambda = 0.5$.

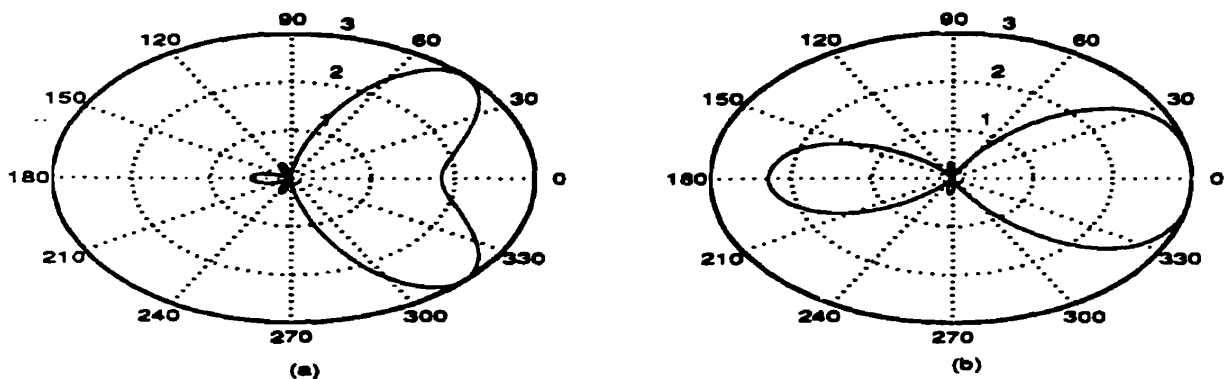


Figure -4.8 Polar plot of the magnitude of the normalized horizontal far-field beam pattern of a linear array with triangular apodization for a beam tilt angle of (a) $\theta = 45^{\circ}$, (b) $\theta = 0^{\circ}$ and $d/\lambda = 0.5$.

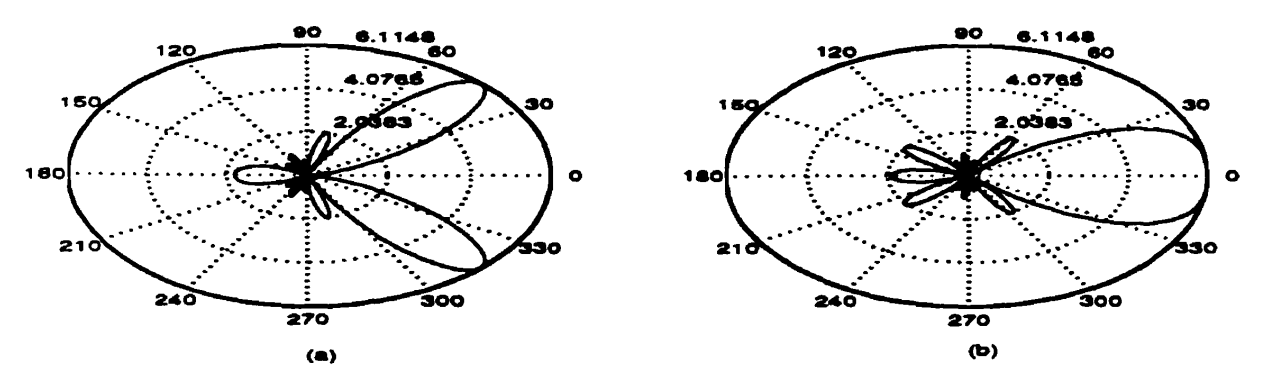


Figure -4.9 Polar plot of the magnitude of the normalized horizontal far-field beam pattern of a linear array with hanning apodization for a beam tilt angle of (a) $\theta = 45^{\circ}$, (b) $\theta = 0^{\circ}$ and $d/\lambda = 0.5$.

or

$$\tau_n = \frac{\theta_n(f)}{2\pi f}.\tag{4.56}$$

.

34

5. Methods and Procedures

This section describes the methods and procedures for investigating experimentally the proposed implementations of digital beamformation. The system used for the investigation can be divided into three components: 1) data acquisition and 2) signal processing and 3) image reconstruction. The hardware and software implementation of each of these components is described below.

5.1.1 Data Acquisition

Ultrasound images are obtained from a Aloka ultrasound machine (Aloka, Tokyo, Japan, model: SSD-246), manufactured in 1964. The transmit part of the system is a parallel real-time transmit system with a 3MHz, 64-element linear transducer array and pitch of 2 mm. The elements are 0.2mm from the probe surface. The transmit circuitry of the machine consists of a trigger which generates a gated square pulse. The amplitude is variable from 0 to 400 V p-p. This trigger pulse is applied to the transmit elements through a dual channel multiplexer.

The RF (raw or radio frequency signal) data is then received linearly by tapping the test points on the receive circuit of the machine after pre-amplification and transferred to a Tektronix digital oscilloscope (Model: TDS-520, 1991) where the A-scans (received electrical signals) are viewed. The oscilloscope digitizes the A-scans using an 8-bit analog-to-digital converter at a sampling frequency of 25 MHz. The digitized samples are transferred and stored in a Pentium PC (66 MHz and 32 MB of RAM). The system allows the efficient recording and transfer of the single element data, using a GPIB

interface and an IEEE Std. 488.2-1987 GPIB cable that is connected to the 24-pin GPIB connector (D-type shell, IEEE Std 488.1-1987) on the oscilloscope. Each A-scan has 72K samples corresponding to a spatial range of about 130mm. This system is not capable of performing any real-time imaging, because of the absence of a real-time digital beamformer. All beam forming and image reconstruction is carried out digitally, off-line on a computer to emulate a full digital imaging system, which is described next. This method is advantageous since the received signals can be accessed at all stages in the signal processing chain. See Figure 5.1 for the experimental setup.

5.1.2 Signal Processing and Image Reconstruction

Figure 5.2 shows the schematic representation of the software-implemented signal processing and image reconstruction of the received signals. Before beginning the signal processing the signals are averaged over a number of cycles to remove non-periodic noise imposed by the data acquisition system. The beam-forming unit forms the first part of signal processing. It weights (apodizes) and delays the individual single element RF signals and sums them into a RF scan line.

The delay and apodization values to the beamforming unit are given as coarsely sampled representations of the ideal delay and apodization functions for each element. The delay system operates by dividing the desired delay at a given time into a coarse delay and a fine delay. The coarse delay is in units of the sampling time interval, $T_s = 1/f_s$, and can be implemented by simply shifting the signal an integer number of samples. After the coarse delay operation is performed, the fine delay is added after up sampling the coarse

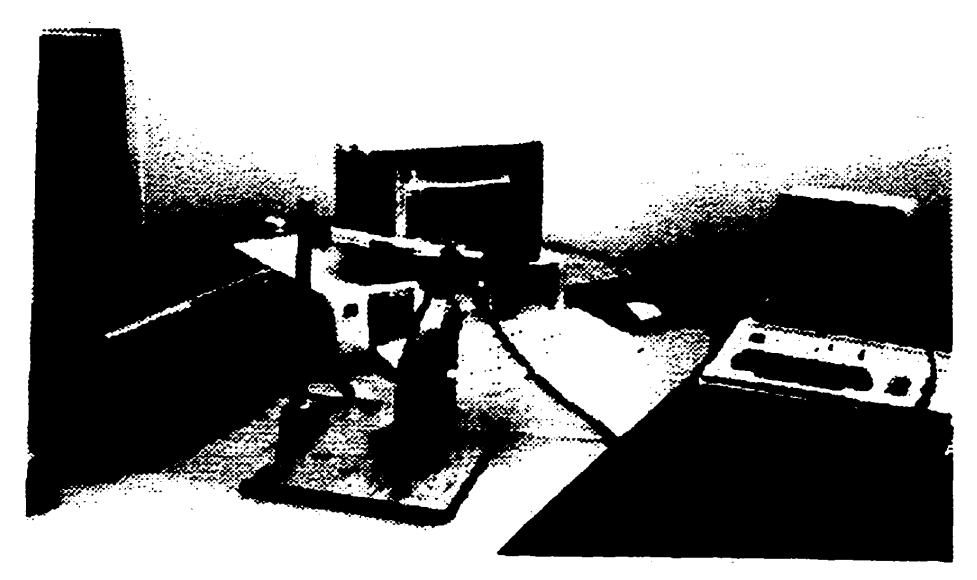


Figure -5.1 Picture of the experimental setup for data acquisition

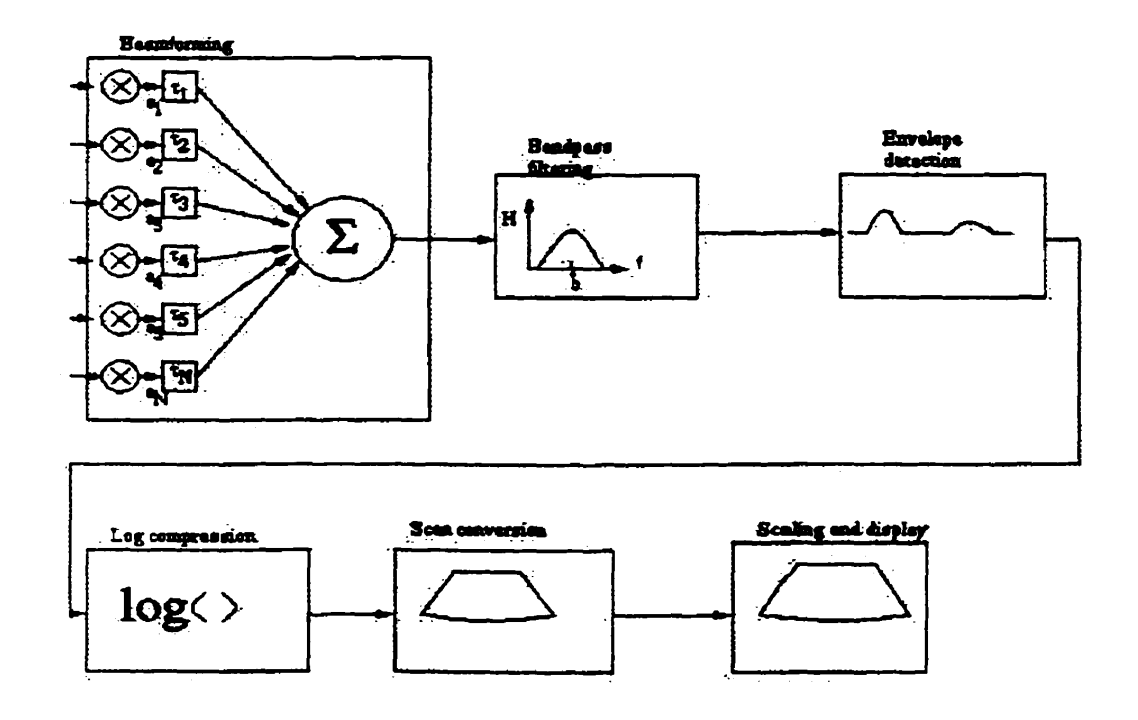


Figure -5.2 Software implementation of beamforming and signal processing.

delayed signal by a factor proportional to the delay error. The signal is then down sampled to the original frequency.

Following the beam forming, the RF data are filtered with a digital bandpass filter to increase the signal-to-noise ratio. They are then envelope detected using the Hilbert transform technique [36]. Since the real-time transmitter has a fixed transmit focus, a retrospective filtering technique is used to reduce the effects of the fixed transmitter [41]. The inverse filter deconvolves the defocused transmit pattern producing a new in-focus transmit/receive image. The inverse filter is designed using least-squares method and is described later in the section. Finally, the scan lines are log compressed to reduce the dynamic range, scan converted, re-scaled and displayed. All images presented in this thesis were reconstructed on a rectangular grid with 192 beam lines positioned at constant increments of $\sin(\theta)$ over 512 pixels. Also, the scan conversion routine is constructed such that any pixel is the maximum of the number of data points at the region represented by the pixel, thus eliminating the drop in amplitude of the image that would result from simple averaging.

All signal processing and image reconstruction, emulating the digital beamformer systems are implemented on a second computer, a Pentium PC (233 MHz and 64 KB RAM). Thus the PC acts as the receive and display of the experimental setup.

5.1.3 Phantoms

The RF data that are used for experimental investigations are acquired from different phantoms. Since the receiving part of the experimental system described above is not real-time, it excludes investigations where movement distortion could be a problem. Hence all imaging is done on custom built and standard phantoms. Phantoms used in this thesis for the investigations may be classified into water phantoms and tissue-mimicking phantoms.

a) Lucite block in water bath

This phantom has a single Lucite slab of dimensions 12.5×9×1.5 mm which is immersed in a plastic tank holding de-mineralized and distilled water. Lucite is assumed to be a perfect reflector. This phantom is used to characterize transmit and receive beam patterns of the transducer array. The rf signals received are also used to set system parameters such as signal bandwidth, center frequency of transmitted signal and filter cut off frequencies.

b) Lucite block holding tubes of different lengths.

A Lucite block of dimensions $12 \times 6.5 \times 4$ mm has holes drilled on the surface to hold hollow plastic tubes of 2 mm diameter. Copper wires are inserted in the hollow tubes to increase the reflectivity. The lengths of the tubes vary from 1mm to 8 mm. This phantom is in a degassed water bath. It is used to find the point-spread function (PSF) of the different methods.

c) Metallic sphere on Lucite slab.

This phantom has a metallic sphere of diameter 2.5 mm on a Lucite block of dimensions $12.5 \times 9 \times 1.5$ in a degassed water bath. This phantom is used to view improvements in edge detection with beam forming.

d) Lesion and scattering phantom.

This phantom is custom made (Ernest L. Madsen, Dept of Medical Physics, University of Wisconsin, Madison). It has a number of spherical lesions of diameter 6 mm and a backscatter coefficient 14 dB below their surrounding medium. The lesions have a attenuation slope of 0.5 dB/cm/MHz. The surrounding medium consists of glass bead scatterers of 45-53 microns in diameter range. There are 4 grams of beads per litre.. It is used to compare over all image quality for different methods.

e) Cyst and Wire phantom

This is a wire and cyst tissue mimicking phantom (Nuclear Associates, model: #84-317). This phantom has a series of monofilament nylon targets, 0.375mm in diameter that are separated over varying distances. It also has four simulated cysts of diameters 4, 6, 8 and 12mms.(cylinders of gel with no scattering). The filling medium is a hydrogel containing a scattering agent that simulates human liver parenchyma. It is used for comparing the overall image quality and finding the point-spread function.

5.1.4 System parameters

This section presents the various design parameters like beam angle that decides the aperture length, temporal and spatial sampling periods, filter cut-off frequencies, and attenuation coefficients. Computer simulations are done to show the effect of temporal sampling on image reconstruction. The criterion for deciding the minimum spatial resolution are discussed. Also the filter cut-off frequencies and attenuation coefficient calculations are presented.

5.1.4a Beam angle

The beam angle is an angle within which the scattered ultrasonic wave from a point object can be practically received. The received ultrasonic signal along an axis from a point object is dependent on the spatial distribution of ultrasonic signal produced by the transmitted ultrasonic beam. This spatial distribution is primarily determined by the spreading loss of the ultrasonic wave and by the shape and size of the ultrasonic transducer (Section 4 Figures 4.4, 4.5 and 4.6). The beam spread angle or the beam width of the ultrasonic wave transmitted was assumed to be the angle of divergence at -6 dB point. The effective aperture length was determined by this angle. The angle, θ_{6dB} is given [37] by the equation

$$\theta_{6dB} = \sin^{-1}\left(0.71\frac{\lambda}{d}\right) \tag{5.1}$$

5.1.4b Temporal Sampling Period

The temporal sampling period, Δt , is generally determined by the sampling theorem

$$\Delta t \le \frac{1}{2f_{\text{max}}} \tag{5.2}$$

where f_{max} is the maximum frequency in the frequency spectrum. However the transducers have broad band characteristics. Also the received pulse echo has a wide range of frequencies. Figure 5.3a shows the waveform of a transmitted signal, and Figure 5.3b shows its frequency spectrum. Figure 5.4 shows reconstructed images of a point object for four temporal sampling periods as contour plots. The sampling periods correspond to frequencies at the -6 dB point, the -3 dB point, and the maximum amplitude point, respectively, from the frequency spectrum. We see that side lobe level increases as the sampling period decreases. This results in the degradation of image quality. Also analysis of the plots show that it is the bandwidth of the waveform and not the center frequency of the transducer that determines the minimum sampling rate. The rule of thumb states that the sampling rate should be 4 to 10 times the transducer frequency [10, 24].

5.1.4c Spatial Sampling Period

The spatial sampling period is necessary to determine the beam space resolution and number of beam lines in a scan format. Generally, the maximum spatial frequency is the frequency at the -6 dB point in the spatial frequency spectrum. Also the azimuthal resolution is given by the following equation

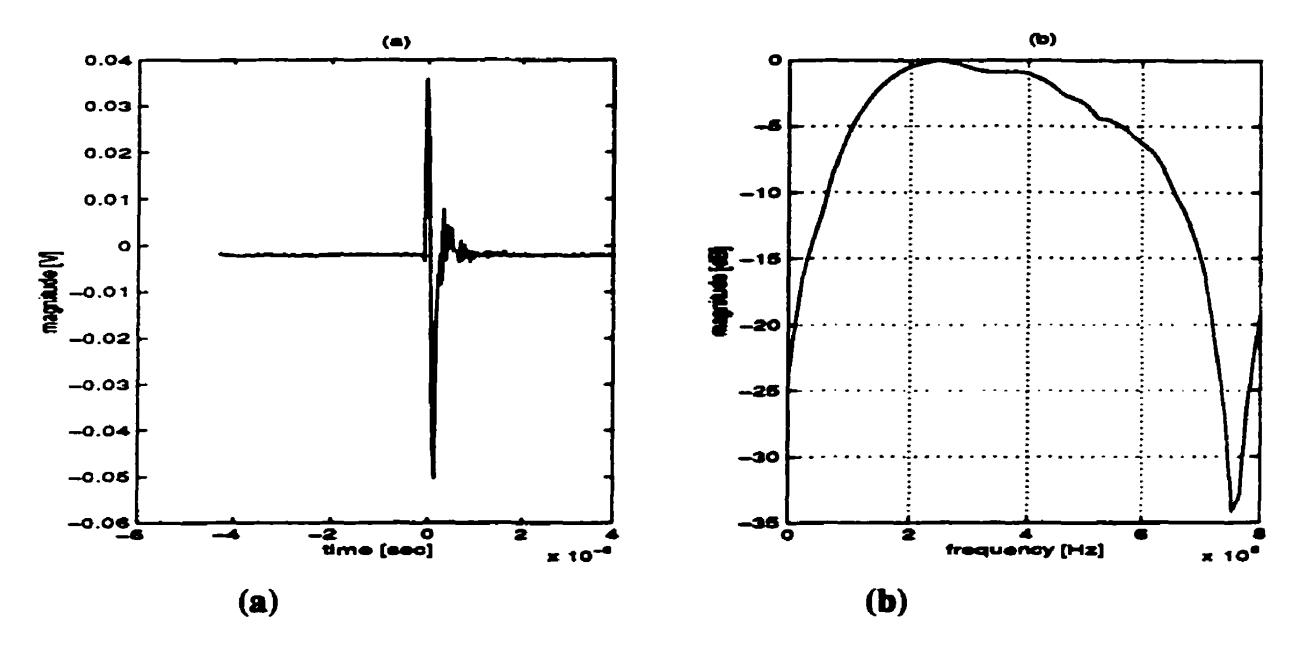


Figure -5.3 Transmit pulse signal of the experimental system. (a) Waveform (b) Frequency spectrum

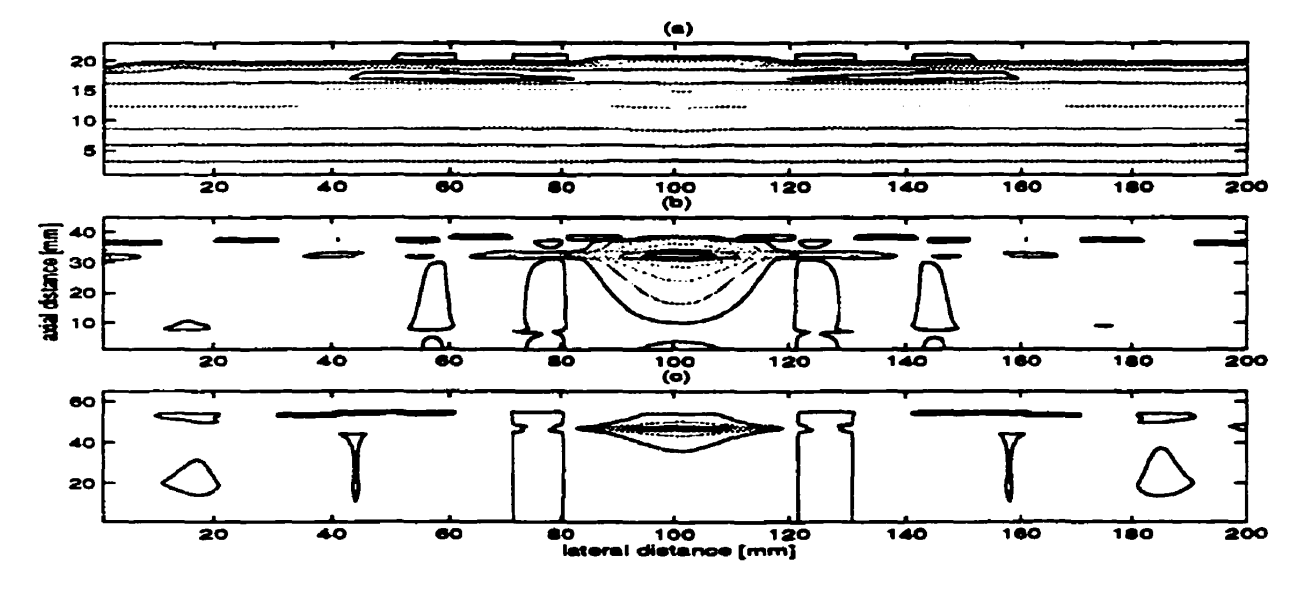


Figure 5.4 Effect of temporal sampling period on resulting image of point object for sampling frequencies (a) 2.5 MHz (b) 4.8 MHz and (c) 6.9 MHz

$$\delta x = \frac{0.6\lambda}{2\sin\theta_{\text{max}}}. (5.3)$$

This is a practical, useful index for determining the proper spatial sampling.

5.1.4d Filter Cut-Off Frequencies

Both low-pass and bandpass filters are used to remove noise and limit the information to the frequency band of the transducer. The frequency content of the initial ultrasound pulse is modified by the frequency response of the recording and digitizing system, which determined initially the parameters for the filters and subsequently modified slightly in response to actual evaluation of the displayed results. The cut-off frequencies for these filters are determined from the frequency spectrum of the averaged RF data. For the investigations in this thesis, the frequencies corresponding to the –20 dB level of the normalized frequency spectrum are taken as the cut-off frequencies. The filters constructed are FIR butterworth filters whose magnitude and phase response are shown in Figure 5.5.

5.1.4e Attenuation Coefficients

When imaging is done on tissue mimicking phantoms, the attenuation of the ultrasonic wave as it travels through the tissue is compensated by a time gain compensating (TGC) amplifier or an amplifier whose gain increases with depth. However, a more flexible method [29] is used in this work where the correction is done on the image values after the image reconstruction.

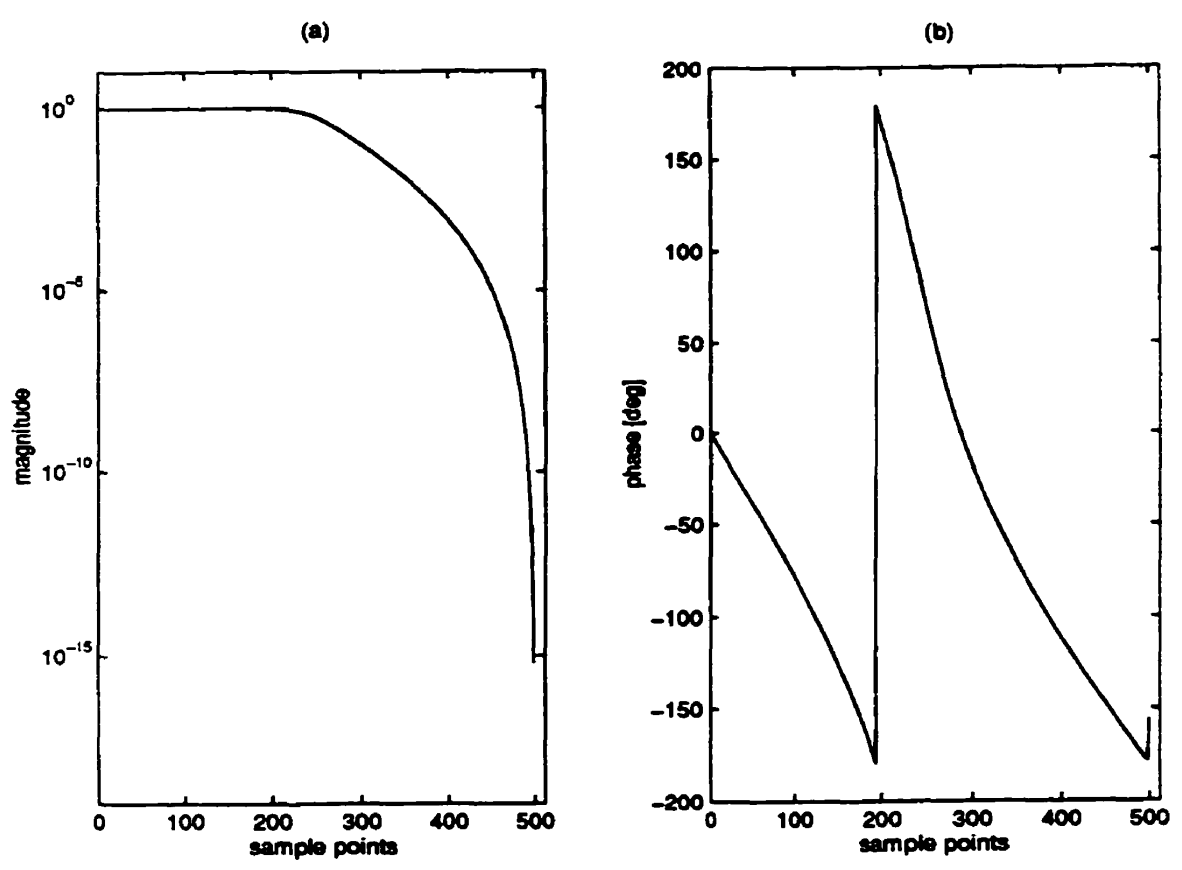


Figure 5.5 Sixth order digital FIR Butterworth lowpass filter used for filtering the RF data: (a) magnitude (b) phase

The incident pressure at a distance r from the transducer in the far field, due to the ultrasonic wave is given by the equation

$$P_{t} = \left(\frac{1}{r}\right)^{b} \exp(-\alpha r) P_{t} \tag{5.4}$$

where the first factor is from the spreading loss and the second factor is from the absorption loss. Since the waves are assumed to be spherical, the value of b is taken as 1. The argument, α , is the absorption coefficient and is frequency dependent. Since the image is reconstructed by summing the data signals from the point element within one effective aperture length, the amplitude of the reconstructed image is dependent only on its distance from the transducer, assuming that the scatter coefficient remains constant. Thus the correction factor, C_r , is given by

$$C_r = r^b \exp(2\alpha r). \tag{5.5}$$

The attenuation correction is then made by multiplying the reconstructed image amplitude by its corresponding correction factor C_r .

5.1.4f Inverse Filter

The transmit part of the experimental system has a fixed transmit focus. A retrospective filtering technique is used to reduce the effects of the fixed transmitter. The filter used is the Fourier transform of the self convolution of the receive aperture function divided by the convolution of the receive and transmit aperture functions. The filter impulse response is short and is designed using the simple mean square criterion method. The filter is independent of the beam direction i.e. $\sin \theta$. The transmit and receive aperture

function for the array is assumed to be rectangular with unit magnitude and zero phase (Section 4.2).

6. Simulation and Experiment

Two different types of investigations were conducted a) computer simulations and b) experimental investigations. Simulation studies of an ultrasound imaging system has been carried out to determine the effect of apodizations, as discussed in Section 4.2, on images. Beam widths and side lobe levels are shown to be affected by the type of apodization used on an array. Also different imaging modalities, analog beamformer and digital beamformer have been simulated. Through the comparison of their performances, the reasons for the cause of gradual shift towards digital beamformation from analog beamforming could be understood, as discussed in Section 3.1. Digital beamforming (DBF) can be subdivided into two types 1) Delay-Sum-Add beamforming (phased array) and 2) Synthetic aperture imaging. Experimental investigations have been carried out to compare and test the efficacy of the above two imaging architectures. The first method is commonly used in present day commercial digital ultrasound machines while the second represents the future direction of the digital beamformer, and has a lot of potential. Through the experimental investigations, the advantages and limitations of both these architectures are brought out which will determine their application in commercial machines.

6.1 Simulations

In the simulations, a 128 element transducer with a center frequency of 3 MHz is used. The element height is 2mm, with the width equal to the wavelength and a -3 dB element angular response of 23.1 degrees. The excitation pulse for transmits consisted of two

periods of a 3 MHz sinusoidal wave with Hanning weighting. The impulse response of both transmit and receive aperture is a two cycle Hanning weighted pulse. The simulations demonstrated the spatial variation of the point spread function for several different imaging modalities, and the beam widths of each system at -6 dB and at -10 dB were plotted as function of range. The simulations are carried out with either a single transmit and receive focus, multiple focusing on both transmit and receive, or dynamic focusing. Apodization consisted of either rectangular or Hanning weights. The number of transmit elements used in the simulations was either 64 or 128.

Configuration A simulated a single transmit focus and receive focus using 128 elements which were uniformly weighted. Configuration B simulated a conventional analog beamformer with single transmit focus and multiple receive focal zones. Each zone had a length of 20 mm. It used 64 active elements for transmit and Hanning apodization to weight the elements (both transmit and receive). For configuration C, four transmit and receive focal zones were used. The length of the focal zones was 20 mm. 128 transmit elements were used. Configuration D simulated a typical digital beamformer, with multiple transmit focus and dynamic receive focus. The transmit had four focal zones of length 20 mm. Hanning apodization is employed to maintain a constant f-number over each focal zone. A f-number of 4 was used on transmit and 2 on receive. For configuration A, a point target at the transmit focus was used. For configuration B, C and D, a five point target with the points at the center of each focal zone was used. These configurations represent the gradual evolution of beamformer from analog to the present day digital beamformer.

6.2 Experimental Investigation

The two different implementations of the digital beamformer for which experimental investigations were carried out are described below.

6.2a Delay-Sum-Add (DSA) Architecture

This implementation of digital beamformer is the earliest and commonly used beamformer in commercial ultrasound imaging instruments. All the beamforming was done after the data were acquired using the experimental imaging system described in Section 5. In this method, the beamformer samples the pulse echo received at each array element and stored prior to the delays being applied. The stored samples for all array elements, for a particular steering direction are delayed according to the receiving time delays for the focal point and summed to obtain the constructive interference. The amplitude of the envelope of the focused signal is displayed with corresponding brightness.

Linear Array Delay Mathematics

The method by which a linear array may be excited in order for the wavefront to propagate in any desired azimuth angle is shown in Figure 2.3 (Section 2). Figure 6.1 shows the coordinate system used to determine the time delay needed for an element so that the summing of echoes from a target at a range R_{fp} and angle θ produces

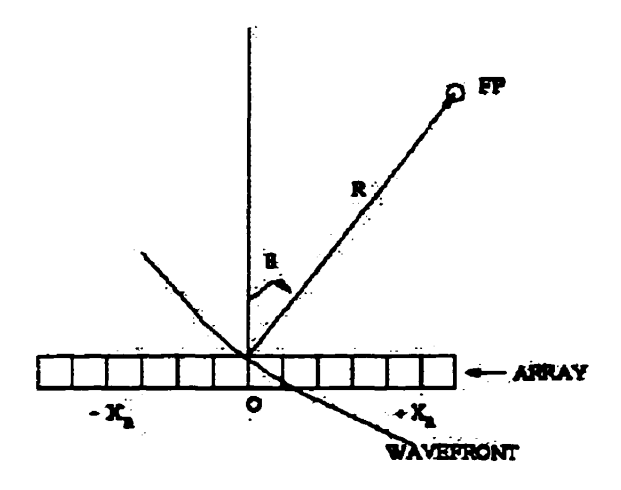


Figure - 6.1 Coordinates for calculating the time delays given by Equation (6.1)

constructive interference. For the calculation, it is assumed that the echo wavefront returning from a point scatterer is of circular shape. The resultant delay τ_n required at an element that is at a distance x_n from the center of the array for the delayed element's output to coincide in time with the center element output is given by

$$\tau_n = \frac{1}{c} \left\{ R_{fp} - \left[R_{fp}^2 - 2R_{fp} x_n \sin \theta + x_n^2 \right]^{/2} \right\}$$
 (6.1)

Here R_{fp} is the radial distance from the array center and θ is the pointing angle relative to the array normal. The constant c is the velocity of sound in the medium.

Two problems arise with the use of above equation in computing channel delay element times. First, the time delay becomes negative and therefore non-causal for negative steering angles i.e. to the left of the center array. This can be overcome by adding a positive constant to the delays for all elements. Second, is the inseparability of θ and R_{fp} dependencies, which make the direct computation of the time delays time consuming. This can be overcome by the use of parabolic approximation. Equation 6.1 can be approximated as

$$\tau_n \cong \frac{1}{c} \left\{ x_n \sin \theta - \frac{x_n^2}{2R_{fp}} \cos^2 \theta \right\}$$
 (6.2)

This equation is a second order approximation and minimizes the mean squared error over the array aperture for reasonable ranges R_{fp} . The desired delay function can thus be approximated by the sum of a linear phase delay and a quadratic phase delay across the aperture, as stated in Section 4.1. Equation 6.2 can be used to calculate both transmit and receive delays. In the experimental set up, the real-time transmit used fixed transmit

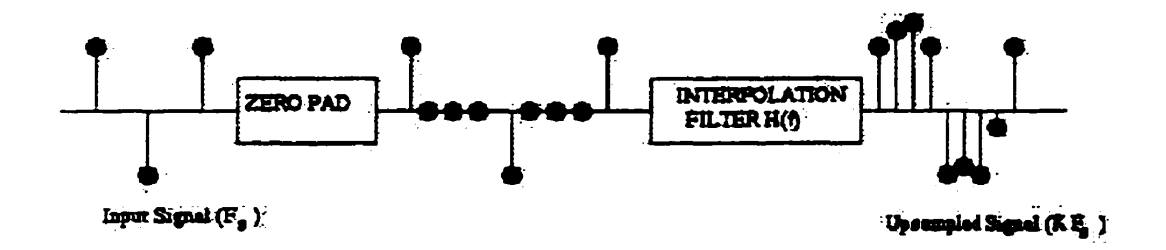


Figure -6.2 Interpolation beamforming

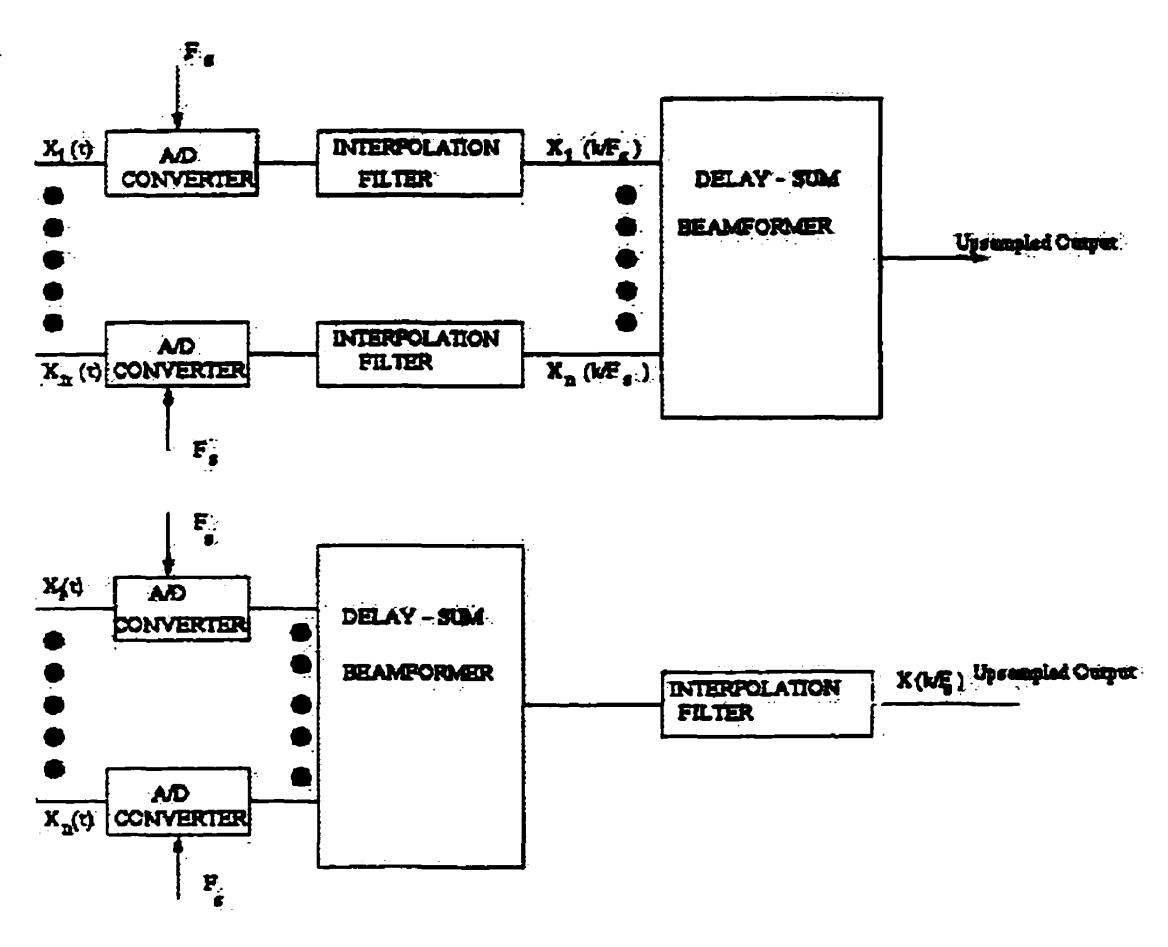


Figure -6.3 Interpolation filter placement in digital beamformer

focus, the time delay equation was used to calculate receive delays for single receive focus and multiple receive focal zones.

In this experimental investigation, the total receive delay time in each receive channel is calculated and stored in a matrix array for each scan, representing a single b-mode scan. After all the received information has been suitably delayed, the outputs are then summed. The sum is then rectified, envelope detected and processed to obtain the brightness information. In case of multiple receive zones, the delays for each channel, focal zone and B-mode scan are stored in a 3-dimensional array. The received information is first delayed for a range R_{fp1} along the same azimuthal orientation. Once all the echoes within that focal region associated with R_{fp1} are delayed, the delay in each of the channels is altered to produce a new focus some distance beyond the first. This process continues until all echoes from the most distant focal region R_{fpN} have been delayed. This delay process is continued for each scan direction.

For the DSA architecture, a high sampling rate is required as discussed in Section 6.1.3. However, if temporal interpolation of the receive data is performed in conjunction with the beamforming operation, the received data needs only to be sampled at the Nyquist rate. This is called interpolation beamforming.

In this investigation, the interpolation is accomplished by zero padding the original sequence, and passing the resulting sequence through a finite impulse response (FIR) low

pass digital filter as shown in Figure 6.2. The FIR digital filter is characterized by a nonrecursive input-output relationship such that

$$y_k = \sum_{n=1}^{N_c} h_n x_{k-n} \tag{6.3}$$

where x_k and y_k denote the kth samples of the filter input and output sequences, respectively, and the h_n denote the N_c filter coefficients. The optimum placement of the interpolation filter also is an important consideration. The filter can be placed either before delaying the receive signals or after they are delayed and summed.

The above architecture of the beamformer is applied on three different phantoms having both single receive focus and multiple foci, with and without apodization. Hanning apodization has been used. Also the different placement of the interpolation filter have been tried out in the beamformer as shown in Figure 30. The optimal placement of the interpolation filter is also an important consideration. Since both the interpolation and beamforming operations are linear, the placement of the two processes can be interchanged as shown in Figure 6.3

.

For DSA beamforming, the signals were sampled at 25 MHz, while for intrepolation beamforming they were sampled at 10 MHz and then upsampled to 25 MHz. The spatial resolution between the beams was calculated using Equation 5.3 ($\delta x = 0.4$ mm). This resolution is large due to the inter-element distance that is 2mm.

6.2b Synthetic Aperture Imaging (SAR) Architecture

In this section, the architecture for digital beamforming with synthetic apertures is described. The synthetic approaches can be separated into two classes:

- synthetic receive apertures
- synthetic transmit or transmit/receive aperture

With synthetic aperture processing, the goal here is to achieve a level of performance without actually employing all the transmit and receive channels. The approach used involves transmitting with two or more transmit sub apertures and receiving with two or more subarrays. Though this approach has received much attention in the literature, few if any results of practical applications have been reported.

The approach used here uses partial beam sums that are obtained from signal subsets of overlapping receive sub apertures on consecutive firings. This architecture is called multi-element synthetic aperture focusing method (MSAF) [33]. The MSAF system is shown in Figure 3.11 with a five element active transmit ($K_r = 5$) and five element active ($K_r = 5$) subapertures. For an N-element transducer array with K_r -element receive subaperture, the overall processing resulting in an MSAF image is expressed as

$$S_{MSAF}(r, \sin \theta) = \sum_{n=1}^{N-K, +1} \sum_{k=1}^{K_r} a_{n,k} (r - \tau_{n,k}, \sin \theta), \tag{6.4}$$

where $(r, \sin \theta)$ represent range, azimuth, $a_{n,k}$ is the signal amplitude from the kth channel of the subparture at the nth firing and τ is the beamforming delay. The MSAF

image can be regarded as the sum of the low-resolution images obtained from each firing.

The following partial beam sum gives the low-resolution image from the subaperture associated with the nth firing:

$$s_n(r,\sin\theta) = \sum_{k=1}^{K_r} a_{n,k}(r - \tau_{n,k},\sin\theta). \tag{6.5}$$

The image quality of each low-resolution image is determined by the single receive subaperture. The lateral point spread function of a K_r -element subaperture is:

$$P_{SAP}(\sin\theta) = \frac{\sin\left(\frac{\pi}{\lambda}K_r d\sin\theta\right)}{\sin\left(\frac{\pi}{\lambda}d\sin\theta\right)},\tag{6.6}$$

where λ is the wavelength and d is the element spacing.

The image reconstruction continues by shifting spatially and temporally, each low-resolution image for each transmit position. The final high-resolution synthetic aperture image is the coherent summation of all low-resolution subpaperture images (Figure 6.4). Thus, the final high resolution MSAF image is given as:

$$S_{MSAF}(r, \sin \theta) = \sum_{n=1}^{N-K_r} s_n(r, \sin \theta), \tag{6.7}$$

where N is the total number of transducer elements. The overall PSF of an MSAF system is approximated as:

$$P_{MSAF}(\sin\theta) = \frac{\sin\left(\frac{2\pi}{\lambda}(N - K_r + 1)d\sin\theta\right)}{\sin\left(\frac{2\pi}{\lambda}d\sin\theta\right)} \times P_{SAP}(\sin\theta), \tag{6.8}$$

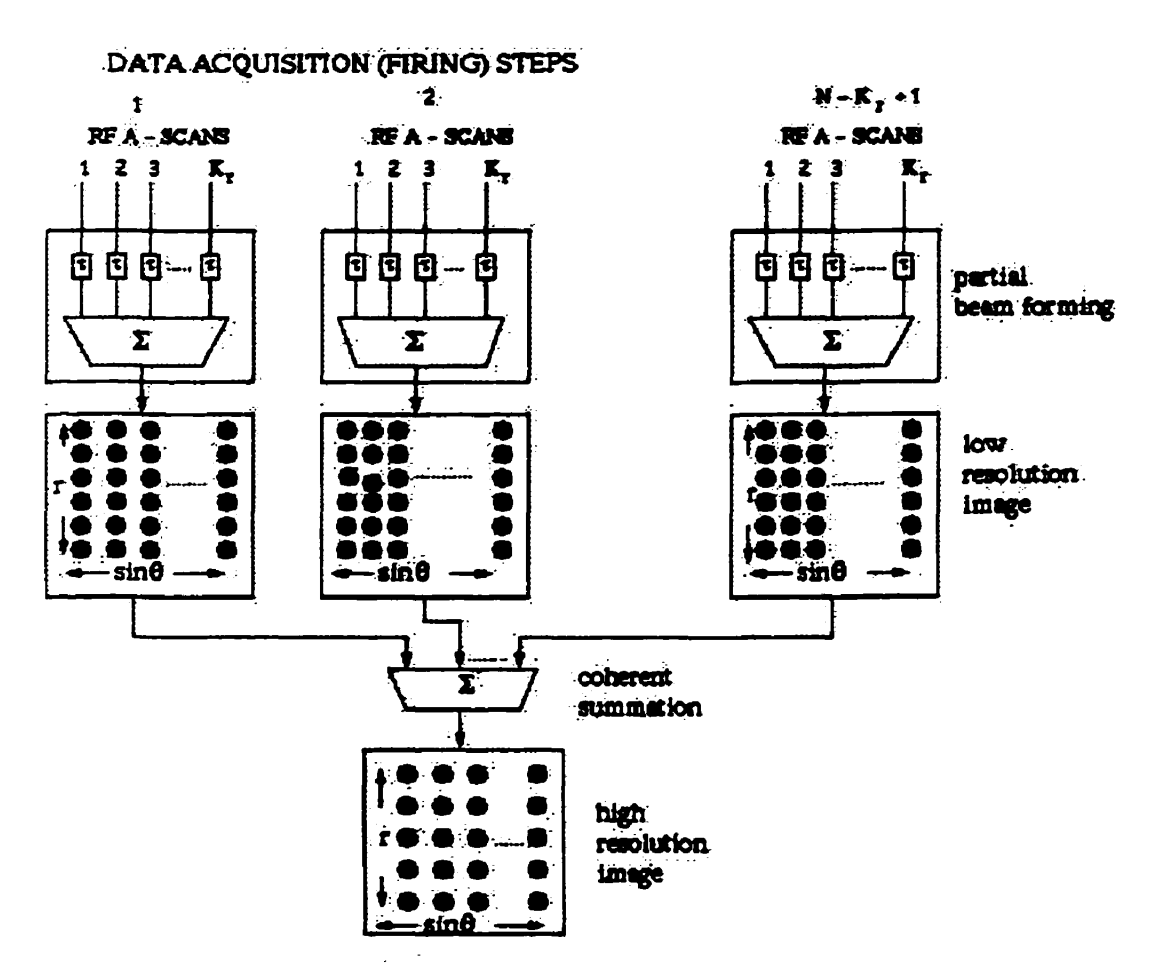


Figure -6.4 Synthetic aperture imaging architecture

where the first term is the two-way PSF of the synthetic aperture formed by subaperture steps, and second term is the one-way PSF of the receive subaperture.

The MSAF technique is emulated digitally using the data sets acquired from three different phantoms. The data set is the RF A-scans acquired from the transmit part of the experimental set up. The beamforming is realized by MSAF processing, and is followed by envelope detection and scan conversion. In the investigations, 8 parallel channels both in transmit and receive are used. Each firing is viewed as excitation from a single virtual element, and hence does not require any transmit beamforming. The MSAF is based on 64-element array and hence employs 56 firings/frame. The final high-resolution image is simply obtained by pixel-to-pixel summation of low-resolution images.

The images obtained from the DSA and M-SAF method are compared with images from a digital ultrasound machine that acts as the "gold standard". The machine used is a ATL HDI UM9 machine. The phantoms were imaged using a linear array consisting of 128 elements and had a center frequency of 6.9 MHz. The RF data are sampled at 20 MHz and are stored on a magneto-optical drive. The data is then transferred to the computer for image reconstruction.

7. Results

7.1 Simulations

The trade-off between resolution and sidelobe level associated with the application of apodization weights as described in Section 4.2 is explored using a wire object. Configuration A with 128 transducer elements, as described in Section 6.1 is used to image these wire objects. It had 64 elements active, during transmit and used all the 128 elements for receive. The ultrasound images of the wire objects are presented in Figure 7.1 and were created using configuration A, which had a fixed transmit and receive focus at 100 mm. The wire is placed at a distance of 100 mm from the array surface. The three images are created over a 40 dB dynamic range without apodization, with uniform rectangular apodization and using non-uniform Hanning apodization. The effect of apodization is clearly visible, with apodization improving the lateral resolution (Figurres 7.1b and 7.1c), when compared to the image with no apodization (Figure 7.1a).

Figure 7.2 shows the point spread function (PSF) calculated at a focal range of 100 mm using the configuration A described in Section 6.1. The plots showed the spatial variation of beam width and side lobe level without a) apodization, b) with rectangular apodization and c) with Hanning apodization, as a function of the lateral and the axial distances. To a large extent the performance of an ultrasound imaging system is characterized by the spatial response of the transducer. From the response, one can determine the spatial resolution as well as the image dynamic range, the two most important parameters of

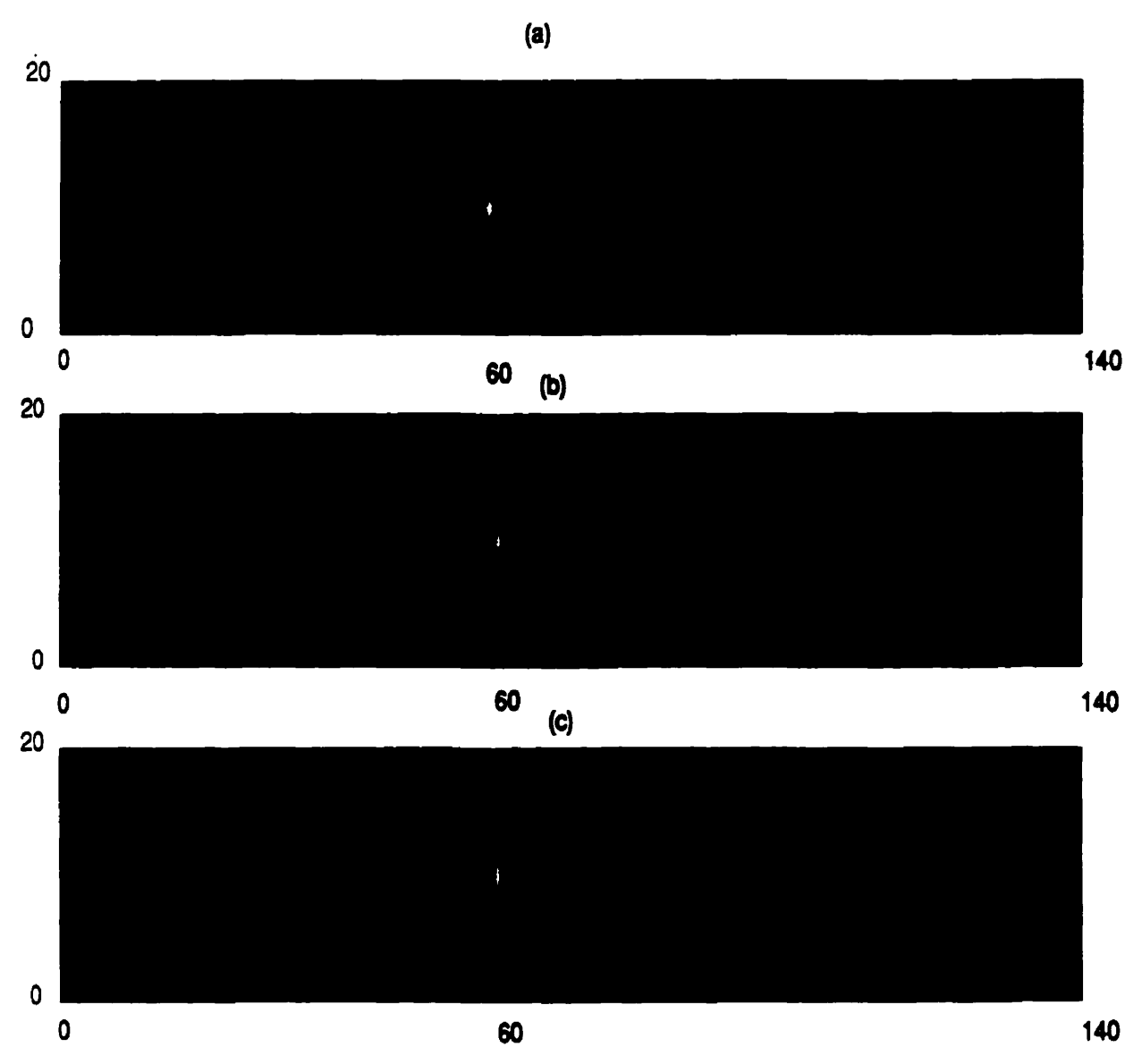


Figure- 7.1 Images produced with single transmit and receive focus displayed over a 40 dB range. The data are collected from a wire object using configuration A with the object positioned at 100 mm: (a) without apodization, (b) rectangular apodization and (c) hanning apodization. All latral and axial distances are in milimeters

image quality. We see a decrease in beam width and side lobe level with apodization (Figures 7.2b and 7.2c), thus indicating a improvement in image quality when compared to the image without apodization (Figure 7.2aa). The peaks of all the PSF's are normalized to one corresponding to the maximum value of the main lobe. Table 7.1 shows the beam width measured at -6 dB and the side lobe levels for each window versus the focal range. The values for beam width versus the focal range are plotted in Figure 7.3, indicating that apodization does help in controlling the beam width as we move into the far zone, where the gradual divergence of beams occur.

Table -7.1. Beam width and side lobe level Vs Focal range: (a) without apodization, (b) rectangular apodization and (c) hanning apodization

Focal Rang	ge	100	103	105	107
Beamwidth [mm]	(a)	3.659	3.689	3.723	3.824
	(b)	3.349	3.620	3.584	3.543
	(c)	3.126	3.569	3.598	3.502
Sidelobe Level [dB]	el(a)	-11.3	-9.2	-11	-11.54
	(b)	-10	-10	-10.9	-12.07
	(c)	-13.37	-12.07	-15.2	-12.83

Figure 7.4 shows the comparison of the -6 dB beamwidth versus the depth for the linear array in configuration A. The point spread functions for the wire object are calculated at distance of 3 mm, 5 mm and 7 mm respectively from the fixed transmit focus of 100 mm. The numerical values are tabulated in Table 7.2. These results indicate that apodization does help in improving the spatial response, when the objects appear beyond the focal region as pointed out in Section 4.2.

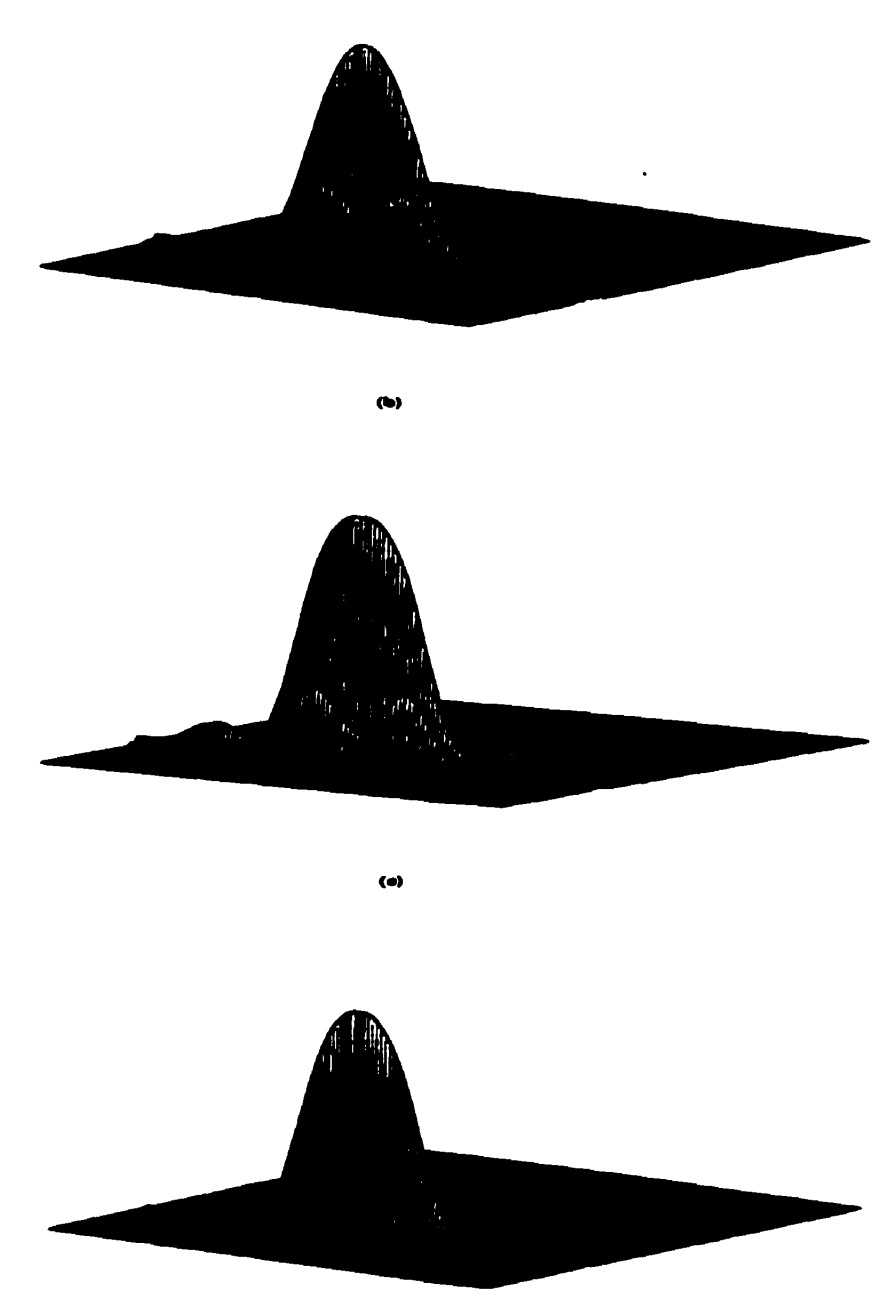


Figure -7.2 Point spread function (PSF) of images in Figure 7.1: (a) without apodization (b) rectangular apodization and (c) hanning apodization

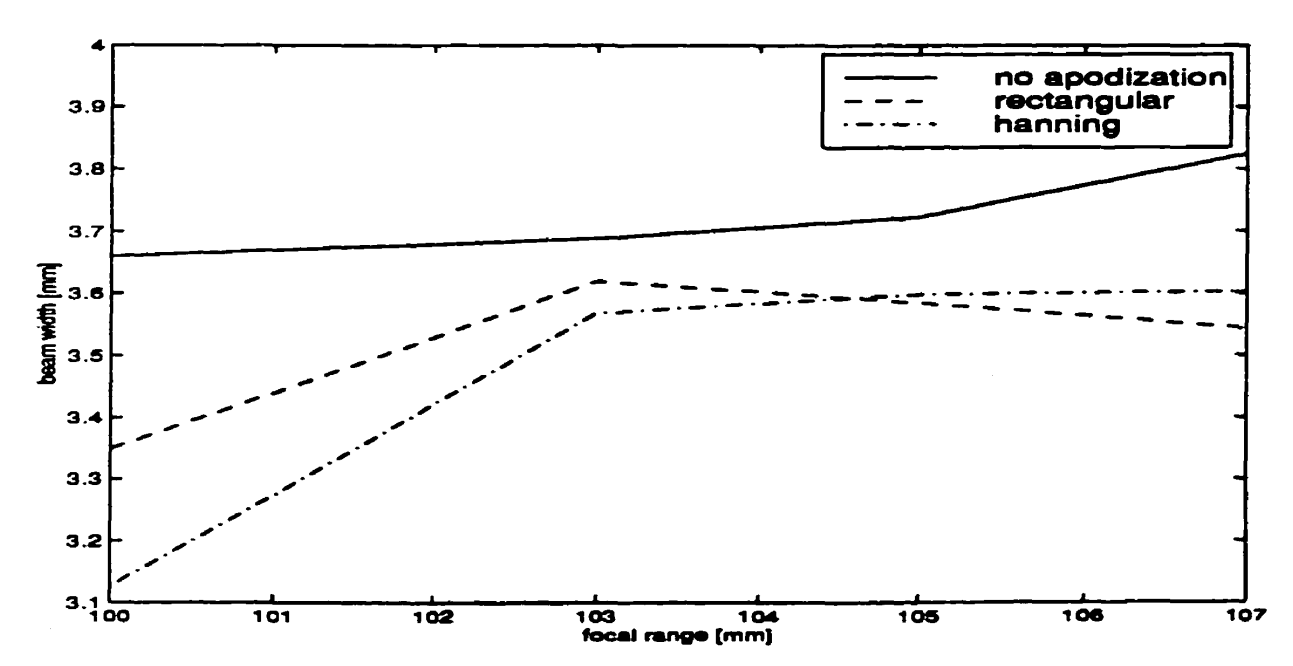


Figure -7.3 Comparison of 6-dB beamwidth versus focal range for a wire object obtained using configuration A.

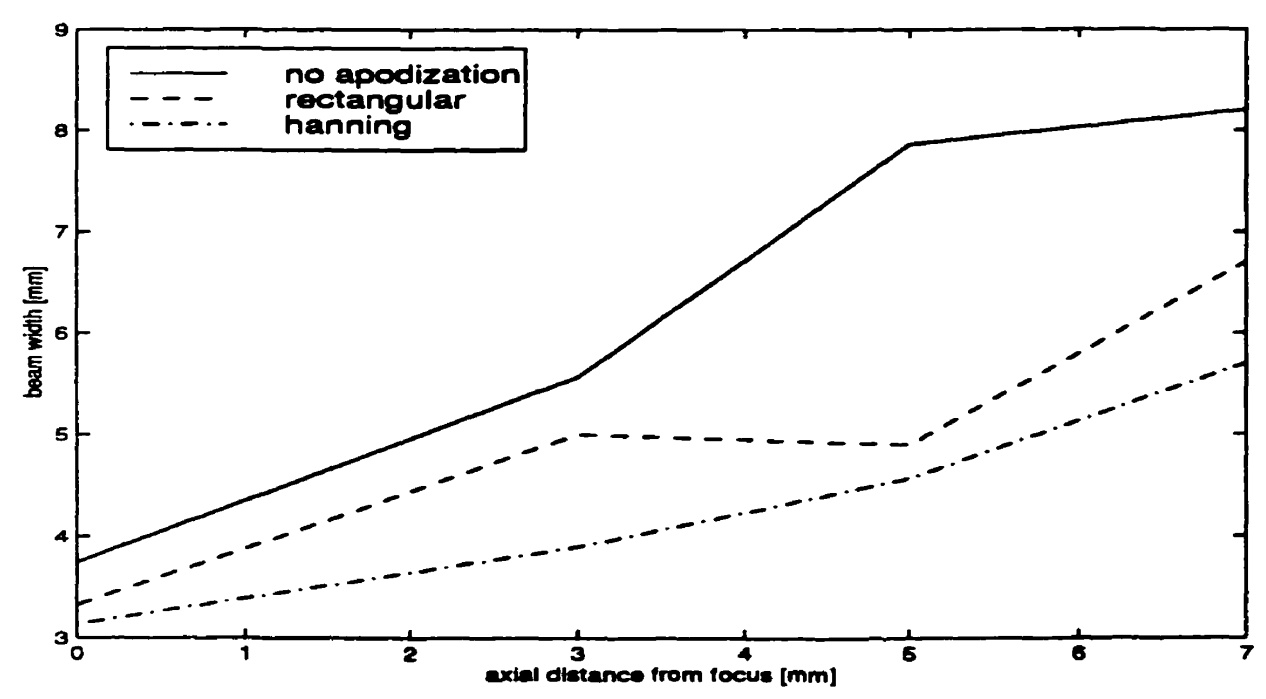


Figure -7.4Comparison of 6-dB beamwidth versus depth for a wire object imaged using configuration A.

Table -7.2 Resolution of a wire target away from the focus of 100 mm for (a) without apodization, (b) rectangular apodization and (c) hanning apodization

Axial distance from focus [mm]		0	3	5	7
Beamwidth	(a)	3.7	5.5	7.8	8.2
[mm]	(b)	3.3	5.0	4.8	6.77
	(c)	3.1	3.8	4.5	5.77

Figure 7.5 shows the surface plots of a 6 wire phantom obtained from configurations B, C and D, as described in Section 6.1, which shows the beam responses and side lobes for the arrays modeled. The surface plots are used to bring out the effect of various configurations on beam response and sidelobes, that may not be visible in gray-scaled images due to the scan conversion. The six wire objects areat distances 35, 50, 65, 80, 95 and 110 milimeters. Figure 7.5a shows the surface plot for configuration B, that had a fixed transmit focus at 60 mm and five receive focal zones starting at 10 mm from the array surface and with a zone length of 20 millimeters. It uses 64 elements during transmit and all 128 elements for receive. Figure 7.5b shows the surface plot for configuration C that had four transmit points at 40, 60, 80 and 120 milimeters and five receive focal zones with same parameters as configuration B. All the 128 elements are used for both transmit and receive. Figure 7.5c is the surface plot for configuration D which employed dynamic apodization and dynamic receive that continousally 'tracked' the receive echoes. The system had four transmit points at 40, 60, 80 and 120 milimeters and the data are sampled at a frequency of 25 MHz as discussed in Section 5.1.4b. These plots bring out the efficacy of a digital beam former in improving the image quality by limiting the beam spread and elminating side lobes (Figure 7.5c), as compared to the

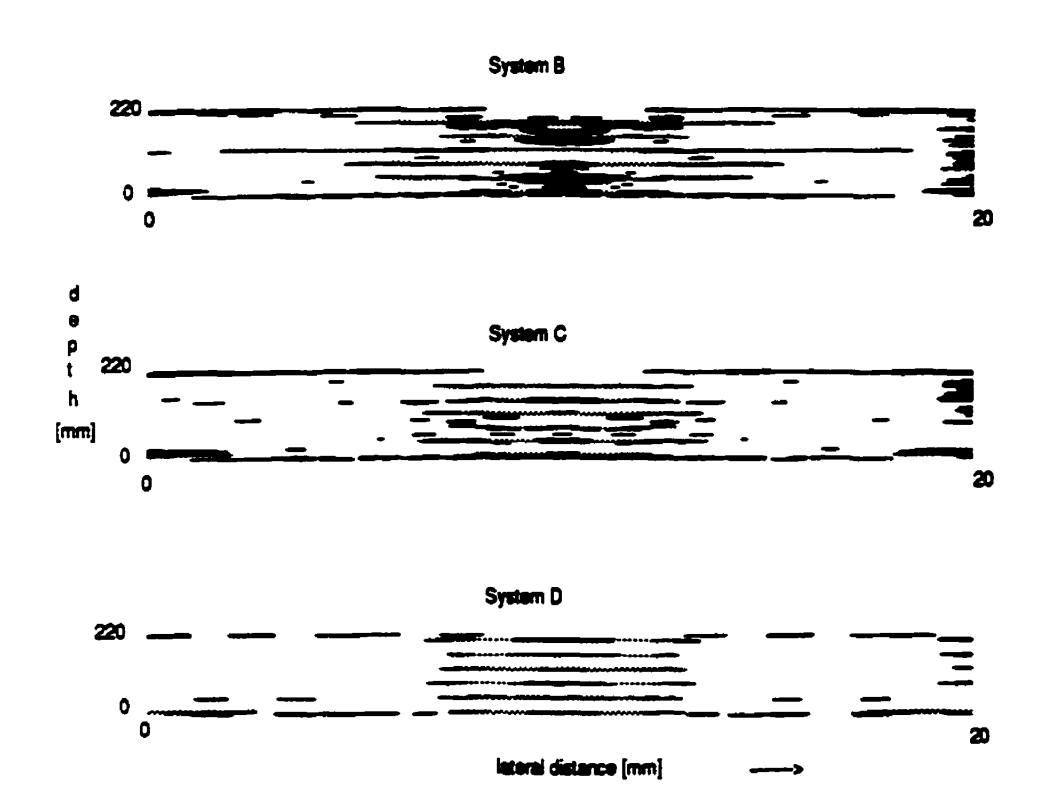


Figure -7.5 Surface plots of images of a six wire phantom obtained from (a) configuration B, (b) configuration C and (c) configuration D

other two configurations (Figures 7.5a and 7.5b). Also the ability of the digital beamformer to pick up signals in the far zone better than configuration C with multiple focus, is evident from Figure 7.5c.

In order to generate the plots shown in Figure 7.6, a PSF is calculated at various ranges between 30 and 120 mm. The lateral response on milimeters at -6 dB and -10 dB were computed for each PSF. These beam widths were plotted versus range. Figure 7.6a shows the lateral response for configuration B with 64 active elements in transmit and 128 elements on receive. Figure 7.6b shows the performance of configuration C with 128 elements active on both transmit and receive. Figure 7.6c demonstrates the decrease in beam width over range when compared to Figure 7.6b, using dynamic apodization and receive. As discussed in Section 3.2, on of the reasons for the popularity of digital beam forming is its ability to maintain good imaging capability at increasing distances from the array. This can be noted from the Figure 7.6c and table 7.3, where the beam width at lower signal levels over focal range is narrower than in configuration B and C (Figures 7.6a and 7.6b respectively).

Table 7.3 presents the results that provide a comparison of the three configuration B, C and D that are modeled.

Figure 7.7 shows the lateral PSF's for the configurations B, C and D, obtained for the wire phantom described above. The magnitude is in dB and is normalized to the peak value. The PSF was calculated at range of 100 mm for each system. An increase in

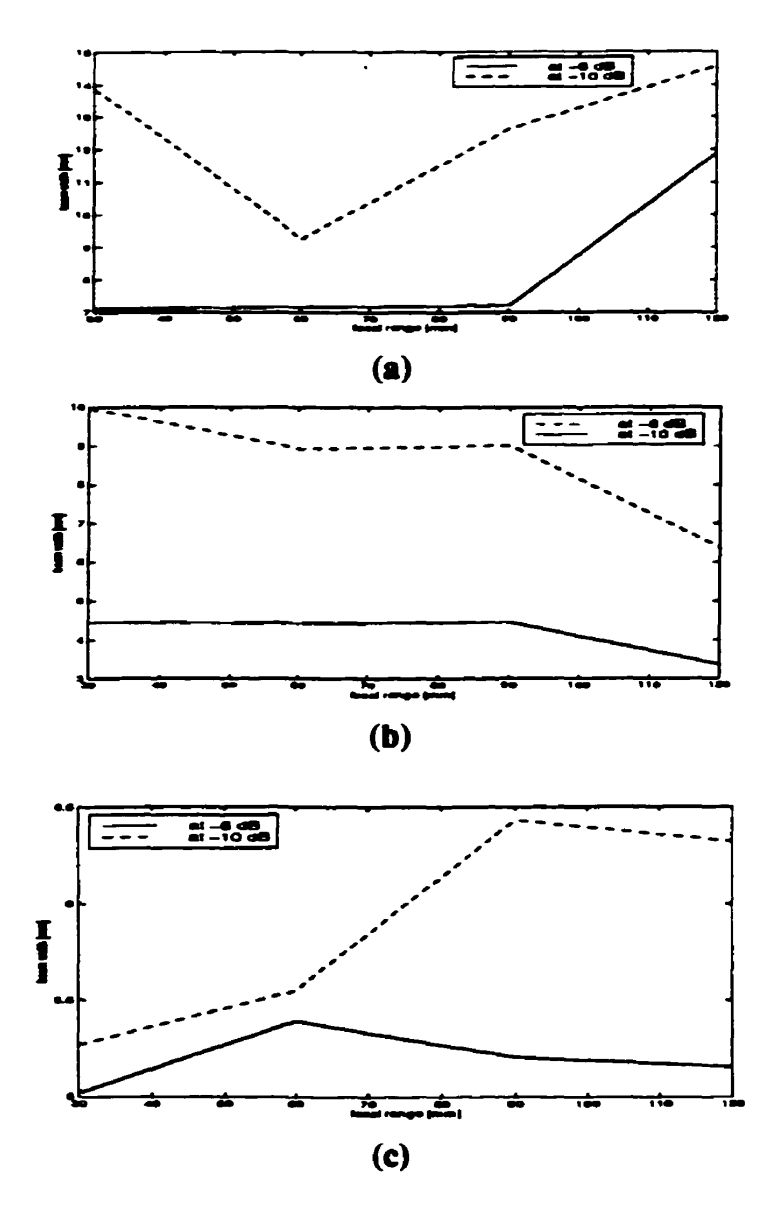


Figure-7.6 Simulated lateral beamwidth versus range for (a) configuration B (b) configuration C and (c) configuration D.

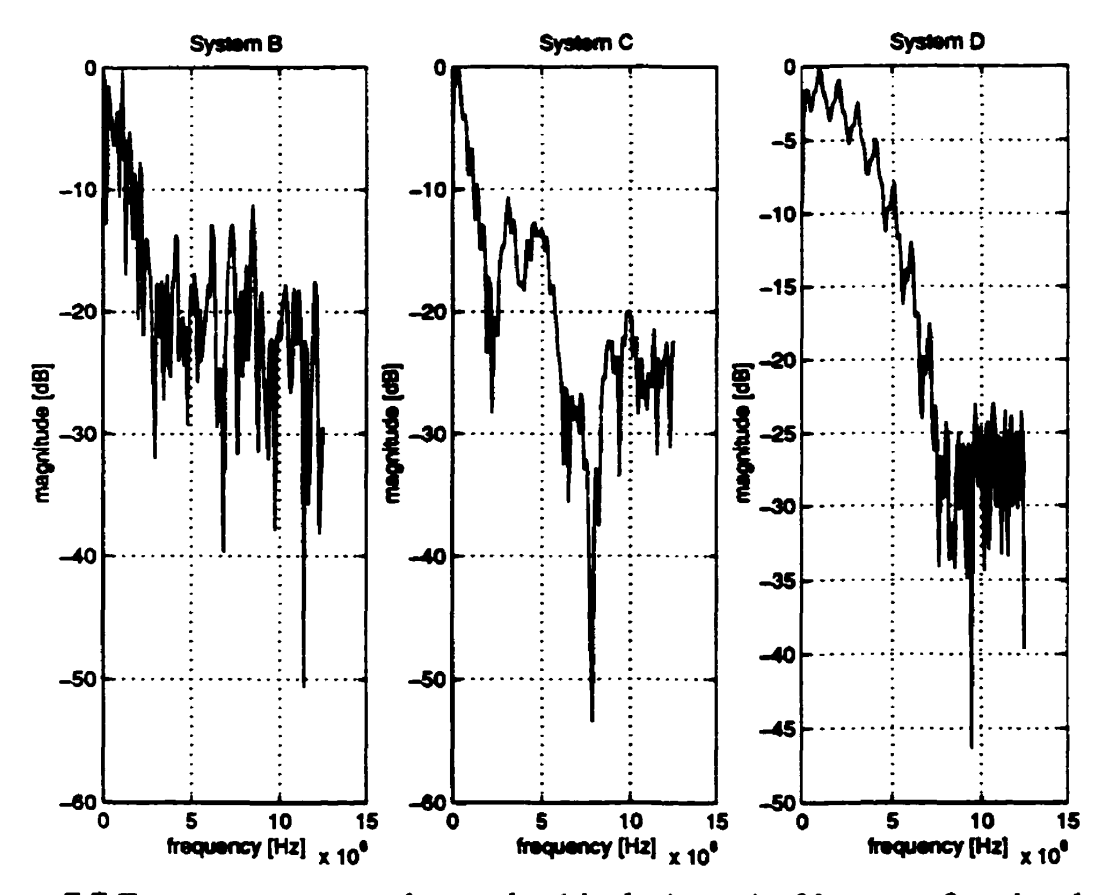


Figure -7.7 Frequency spectrum beam plot (single A-scan) of images of a wire phantom using (a) configuration B, (b) configuration C and (c) configuration D.

overall signal level is consistent with the discussion (Section 3.2) on digital beam forming (Figure 7.7c), when compared to analog beamformers (Figure 7.7b and 7.7c).

Table –7.3 The percentage narrowing of the lateral resolution of system C and D referenced to system B

Focal	Signal	Improvement in lateral resolution		
range [mm]	level	System C	System D	
30	-6 dB	37 %	. 34 %	
	-10 dB	19 %	61 %	
60	-6 dB	38 %	24.5 %	
	-10 dB	34 %	40 %	
90	-6 dB	38.06 %	27.7 %	
	-10 dB	28.7 %	49 %	
120	-6 dB	71 %	56.6 %	
	-10 dB	56 %	56.6 %	

7.2 Experimental investigations

This section presents the results for the investigations carried out for the Delay-Sum-Add and synthetic aperture (SA) architecture as described in Section 6.2. All data acquisitions and processing for image reconstruction follow procedures described in Section 5, except when otherwise mentioned. Gray-scale images, edge detected images, beam plots and contour plots are presented to show the superiority of digital beam forming over conventional analog beamforming (Sections 1.2 and 3). The reconstructed images may not match the quality as seen on commercial ultrasound monitors. This may be because of the poor quality and low end ultrasound machine being used to acquire the required RF data. Also, since the processing is done off-line and simulated, it may not match the actual processing done inside ultrasound machines.

7.2a Delay-Sum-Add (DSA) architecture

This section presents the results for the DSA architecture. The images obtained directly from the ultrasound machine will be called US images, while those images reconstructed after software processing (Section 5.1.2) the raw RF data and beamformed RF data are referred to as raw image and beamformed image, respectively. The phantoms used in this section are the metallic ball on Lucite slab (Section 5.1.3c) and a Lucite block (Section 5.1.3a), henceforth referred to as Mb phantom and Lu phantom respectively.

Figure 7.8 ishows the US image of the Mb phantom obtained from the Aloka ultrasound scanning machine (Section 5.1.1). No TGC (time gain compensator to compensate for the weak echoes acquired from deeper depths) was applied during the imaging. The image was displayed with a overall gain of 3 dB and over a dynamic range of 40 dB. The image does exhibit some ringing effect and poor lateral resolution because of the nature of transducer array.

Figures 7.9a and 7.9b are the raw and beamformed reconstructed images, respectively shown over the same 40 dB dynamic range. The curvature of the metallic sphere is more clearly visible in beamformed image than in raw image. The images are much brighter because of higher amplitudes due to the summing. The difference between the two images are more pronounced when the area around the metallic sphere is enlarged (Figure 7.10). Here the curvature of the top of the sphere in beamformed image can is more defined, while in the raw image it is less clear. The lateral resolution is also improved with beamforming. That digital beamforming helps in better edge detection can be seen in Figure 7.11a. The edges in this image are more continous while in the raw image (Figure 7.11b) the edges are discontinous. There is more noise in the background of the raw image, while in beamformed image it is practically absent. This shows that coherent summing during beamforming reduces and sometimes eliminates noise.

Figures 7.13 show the effect of beamforming at the signal level, which yields better images, when compared to raw signals. Figures 7.12a and 7.13a show the frequency spectrum of the interpolated beam number 122. Digital beam forming does raise the overall signal level while reducing the sidelobes as stated in Section 1.2 and discussed in

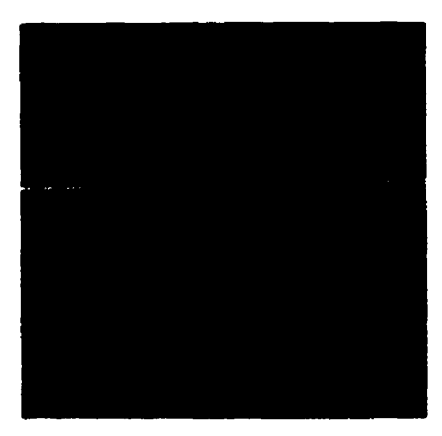


Figure-7.8 Image of a phantom (metallic ball on Lucite) as seen on the Aloka US 64 machine.

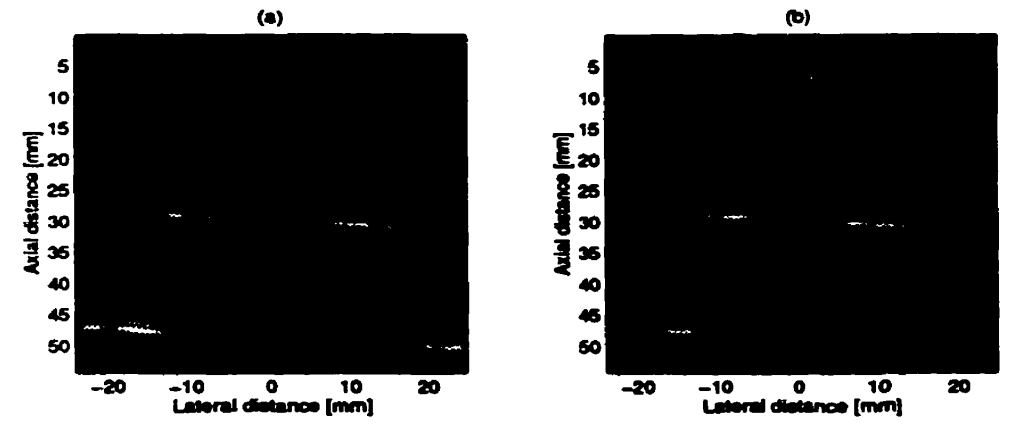


Figure -7.9 Images of phantom (metallic ball on Lucite slab) obtained after processing (a) raw data (b) beamformed data



Figure -7.10 Cropped section of images in Figures 7.9a and 7.9b showing the metallic ball

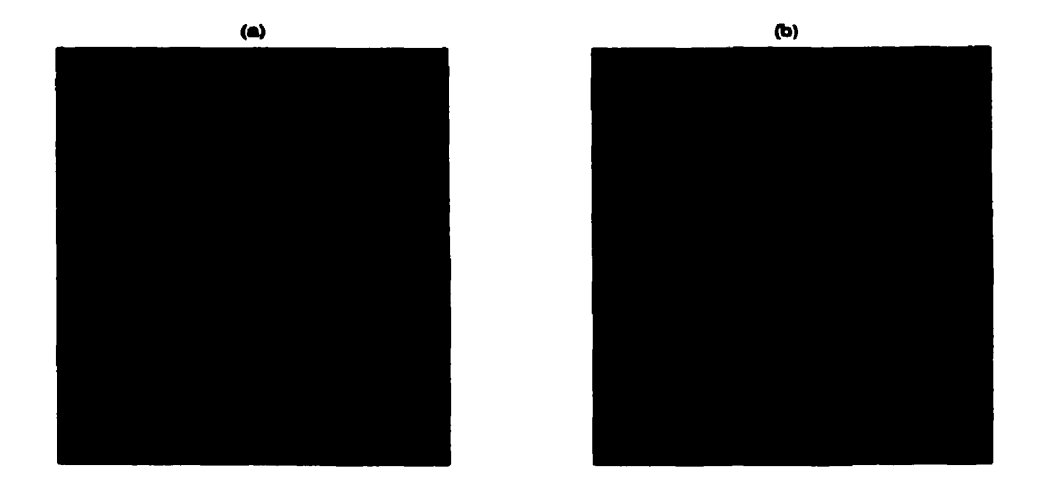


Figure -7.11 Edge detected images of the phantom (metallic ball on Lucite) obtained after processing the (a) raw data (b) beamformed data

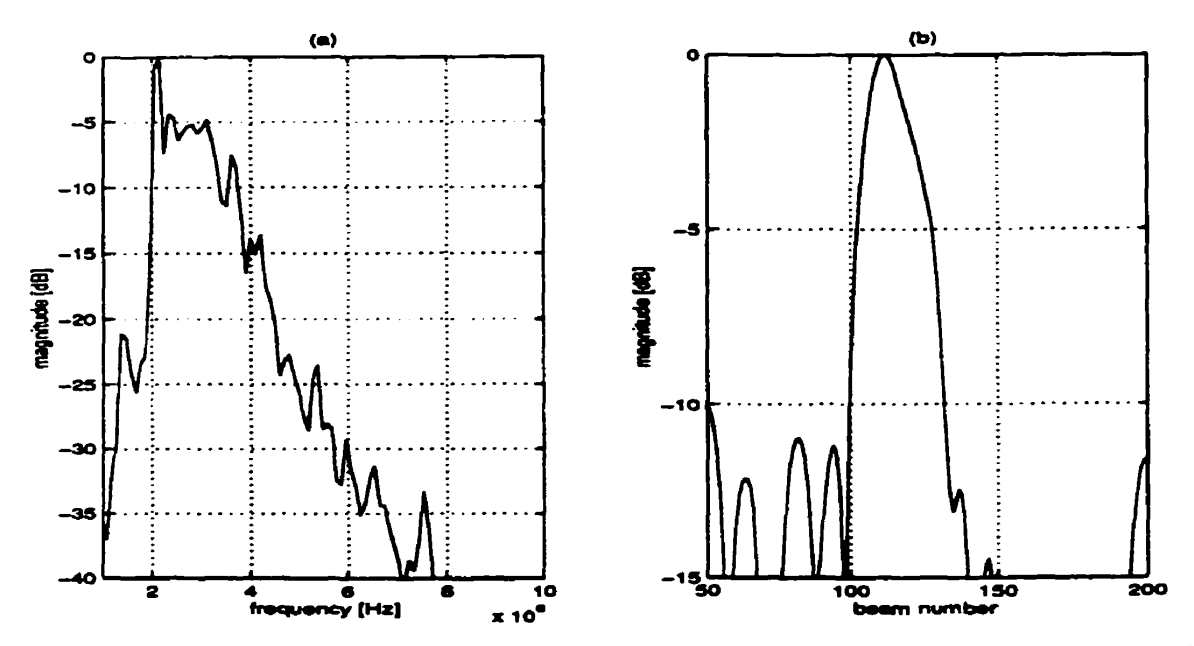


Figure -7.12 Frequency spectrum and normalized beam width ((a) and (b) respectively) of a interpolated beam for processed raw data

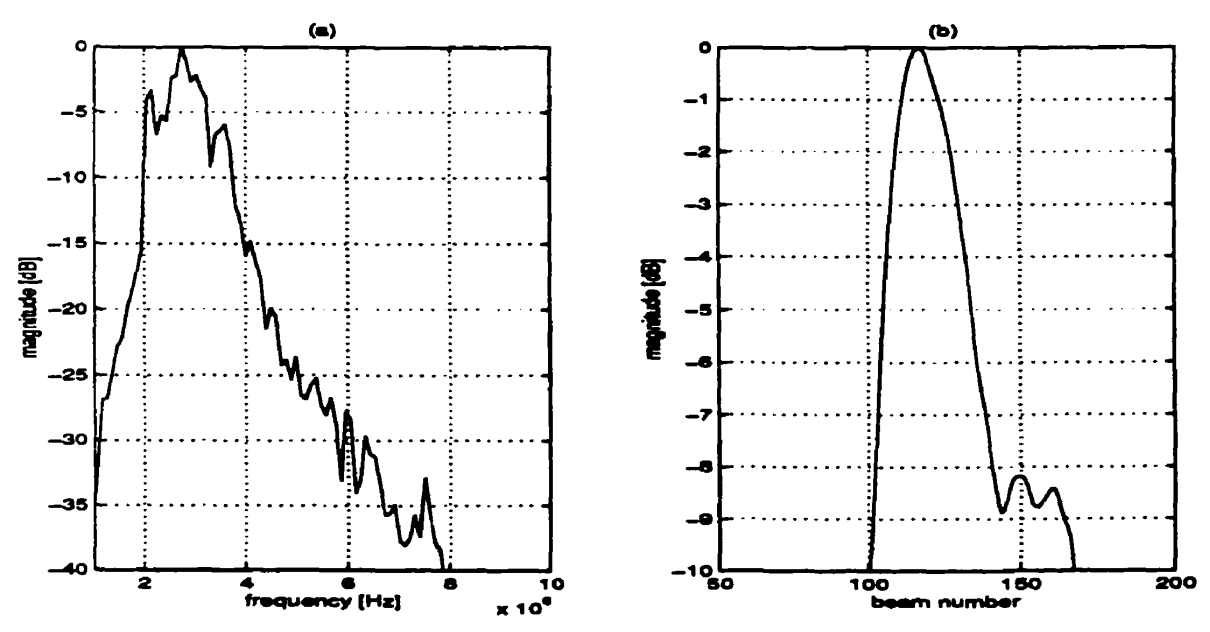


Figure -7.13 Frequency spectrum and normalized beam width ((a) and (b) respectively) of a interpolated beam number for processed beamformed data

Section 3. This helps in increasing the dynamic range of the system. Also as can be seen from the beam plots (Figures 7.12b and 7.13b), the improvement in lateral resolution shown in Figure 7.10b is due to the narrowing of the beams. The -3dB beam width for the raw image is 3.4% broader than the beamformed signal at -3 dB. Also the sidelobes are absent in the beam formed signal which results in an increase in the contrast of the images.

Figure 7.14b further illustrates the improvement in images achieved with digital beamforming. The images of the Lu phantom are better when compared with the raw image (Figure 7.14a). Also digital beamforming does help enhance the signal information at distances far from the array, due to its dynamic receive and coherent summing. This is seen in the beamformed image where the lower surface of the Lucite slab shows up better against the background as compared to the raw image where the contrast is worse.

Figures 7.15 and 7.16 show the frequency spectrum and beam plots of raw and beamformed images of the Lu phantom respectively. Digital beamforming does increase the signal level and lower side lobe level as stated earlier.

Interpolation beamforming is the temporal interpolation of the receive data's performed in conjunction with the beamforming operations. Results are presented on the effect of this method by imaging a Lucite phantom of dimensions $12.5 \times 9 \times 1.5$ mm. The image is cropped to show the upper and lower surface of the block. Figure 7.17 shows the raw and beamformed image after processing the data that are sampled at 10 MHz, which just

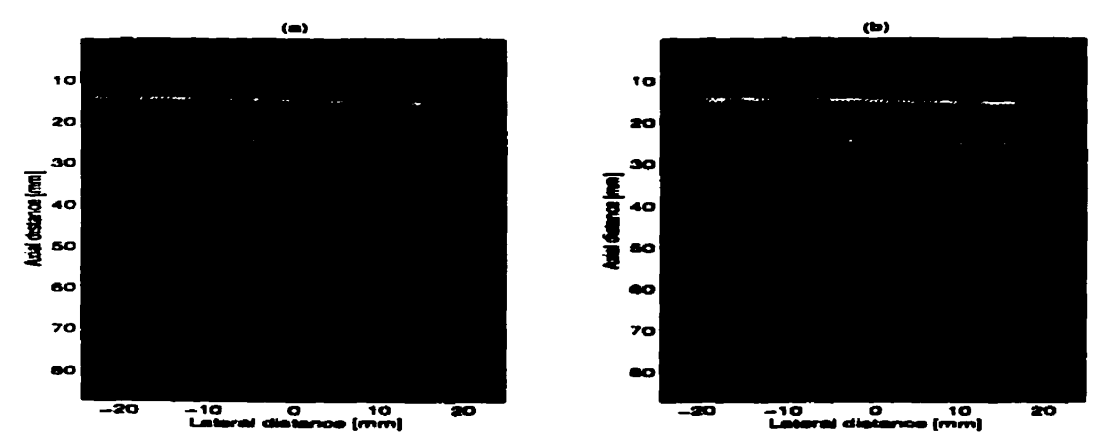


Figure -7.14 Images of a Lucite slab $(12.5 \times 9 \times 1.5mm)$ obtained after processing (a) raw data (b) beamformed data

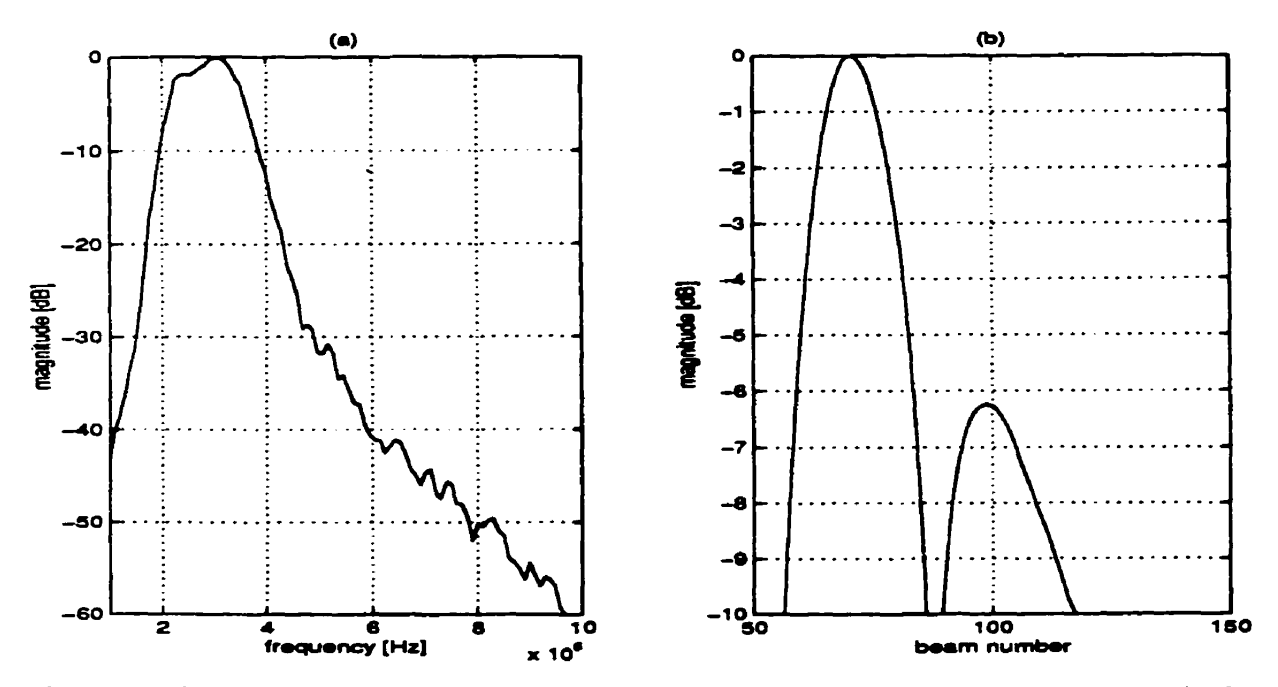


Figure -7.15 Frequency spectrum and normalized beam width ((a) and (b) respectively) of a interpolated beam for beamformed raw data

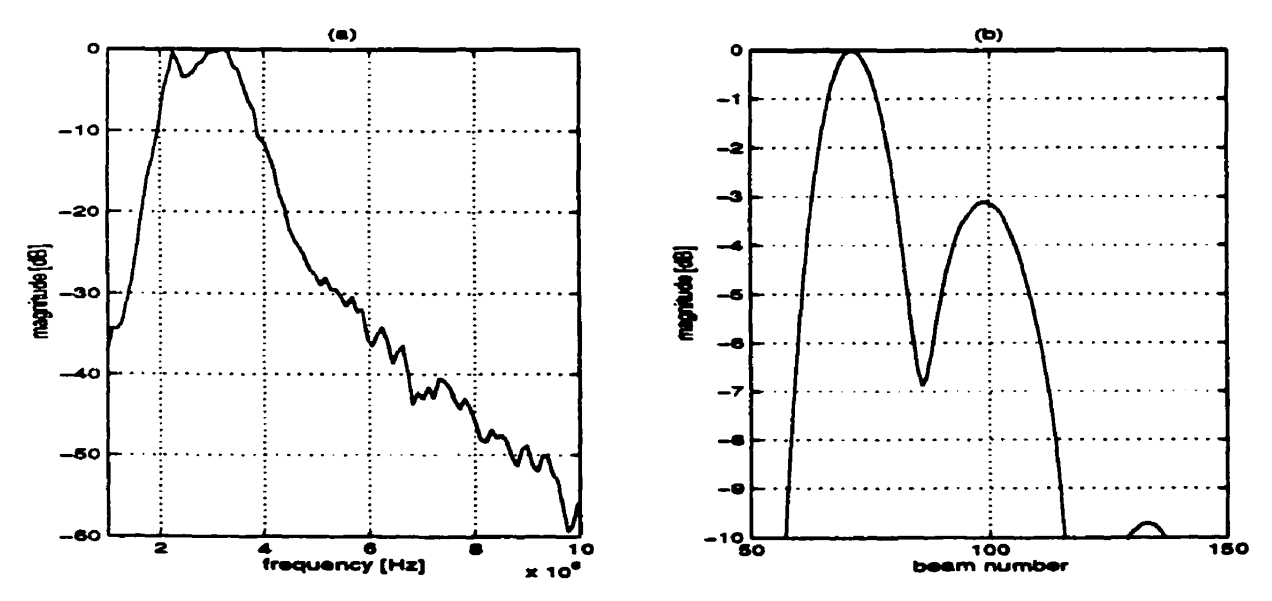


Figure -7.16 Frequency spectrum and normalized beam width ((a) and (b) respectively) of a interpolated beam for processed raw data

satisfies the Nyquist requirements. We see poor image quality and 'dark' pixels indicating lack of sufficient information. Though the beamformed image is comparatively sharper than the raw image, the lower surface of the block is not clear in both images. Comparing these images with the raw and beamformed images respectively in Figure 7.18, the effect of sampling at levels much higher than Nyquist level is obvious. Here the data is sampled at 25 MHz i.e. four times the minimum sampling rate. The images show much better lateral resolution and contrast when compared to corresponding images in Figure 7.17. With interpolation beamforming, the data are upsampled to 25 MHz after they are acquired at 10MHz. Figures 7.19a and 7.19b shows the images obtained after processing the upsampled data before beamforming and upsampling after beamforming respectively. Figure 7.19a has image quality equal to that in Figure 7.18b i.e when the data are actually sampled at 25 MHz. But when the data are upsampled after beamforming operations, the images are of poor quality with low contrast.

Figure 7.20 shows the frequency spectrum of the interpolated beam at (a) 10 MHz, (b) 25 MHz, (c) 25 MHz-upsampled before beamforming and (d) 25 MHz-upsampled after beamforming operations. The data sampled at 10 MHZ, exhibits wide band spectrum as it is sampled at around Nyquist frequency. Figure 7.20b shows a peak around 3 MHz, the center frequency of the transducer and low sidelobes, thus exhibiting excellent dynamic range. Though when the data is upsampled to 25 MHz before beamforming (Figure 7.20c, appears similar Figure 7.20b, it has higher sidelobes thus lowering the dynamic range. Figure 7.20b indicates why Figure 7.19b is of poor quality, with high side lobes and harmonics, thus lowering the dynamic range and contrast level considerably.

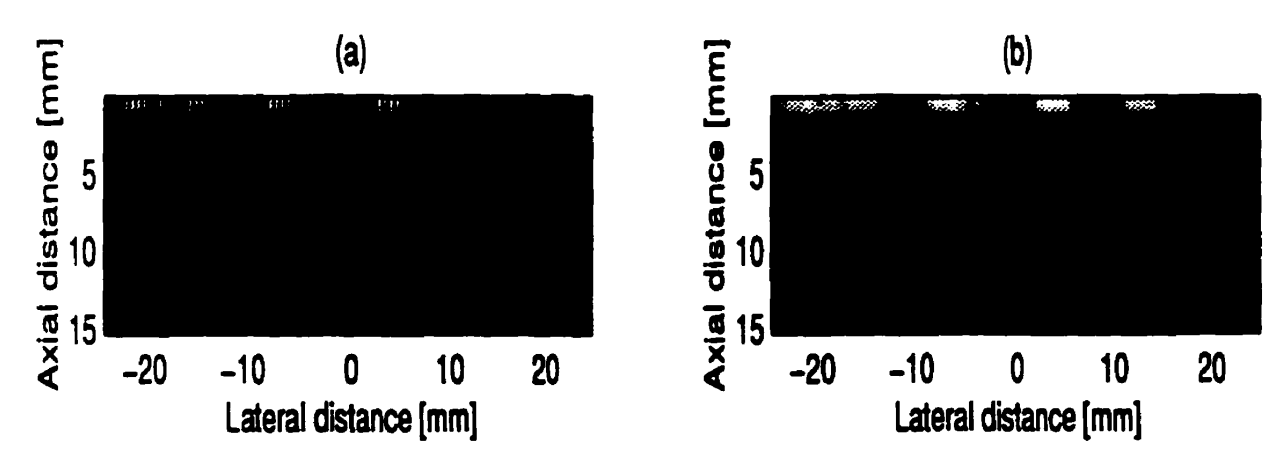


Figure -7.17 Image of the Lucite phantom obtained after processing (a) raw data (b) beamformed data when the signal data is sampled at 10 MHz.

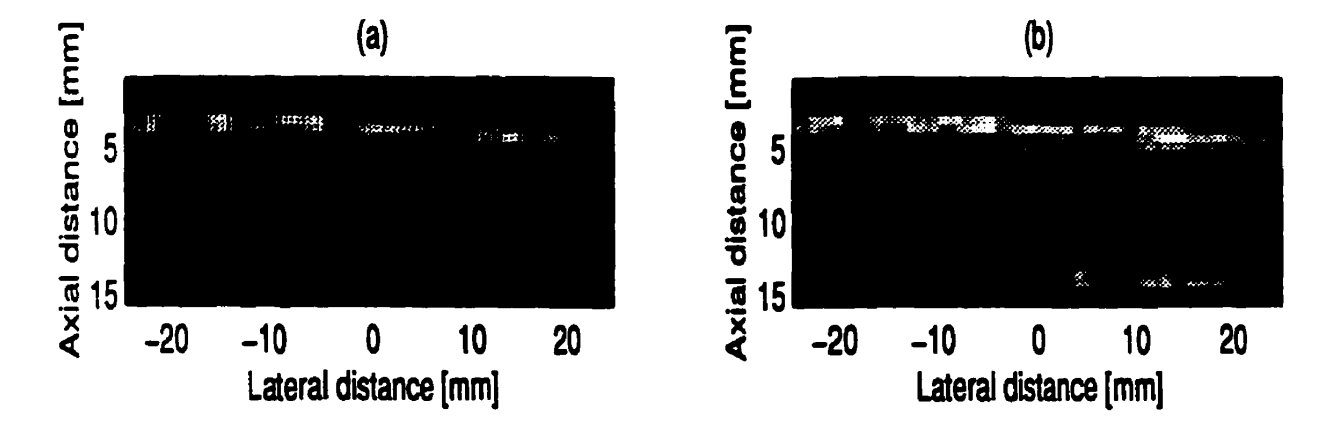


Figure -7.18 Image of the Lucite phantom obtained after processing (a) raw data (b) beamformed data when the signal data is sampled at 25 MHz.

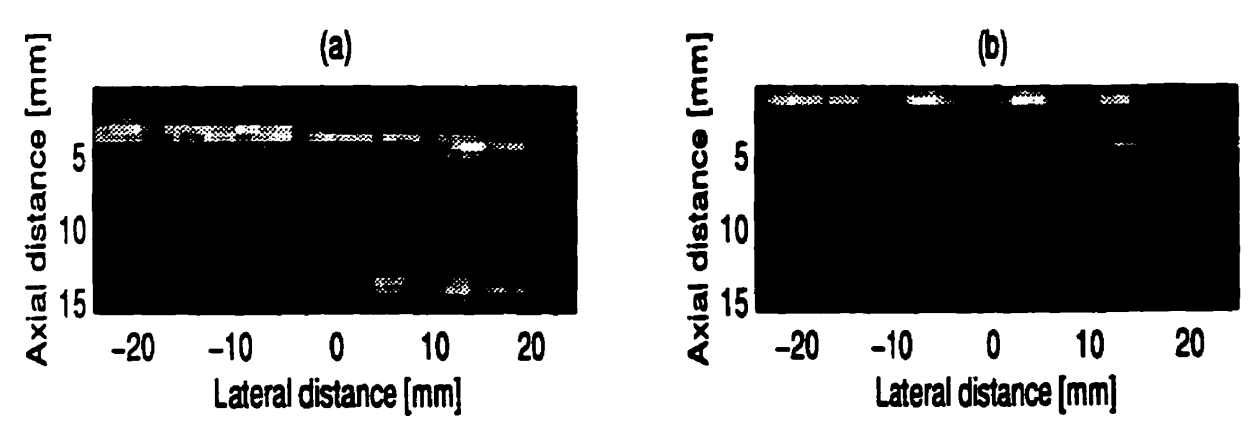


Figure -7.19 Image of the Lucite phantom obtained after processing data (a) upsampled to 25 MHz before beamforming (b) upsampled to 25 MHz after beamforming

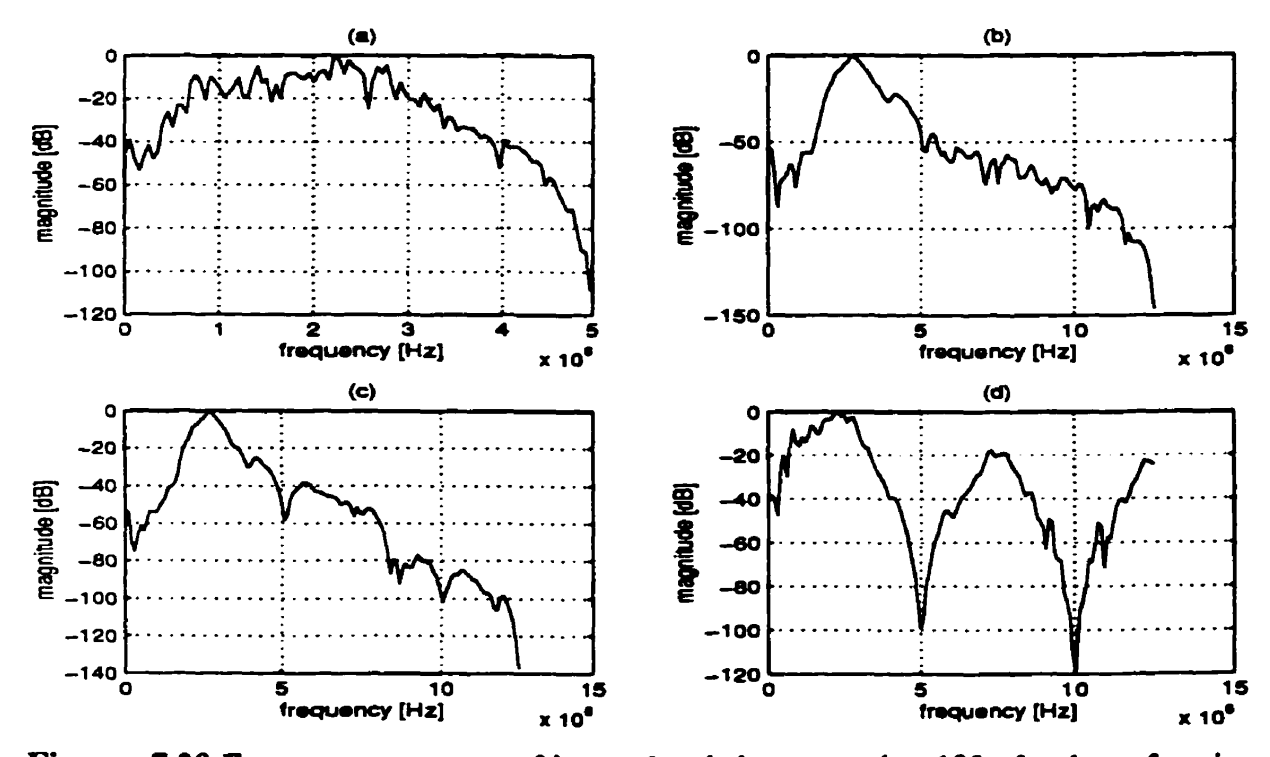


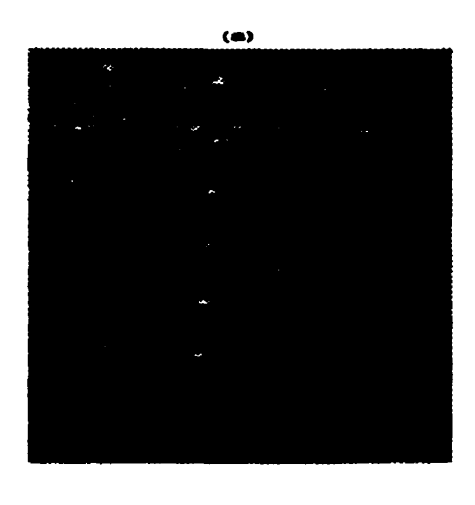
Figure -7.20 Frequency spectrum of interpolated beam number 120 after beamforming when (a) signal sampled at 10 MHz (b) signal sampled at 25 MHz (c) signal upsampled to 25 MHz from 10 MHz before beamforming (d) signal upsampled to 25 MHz from 10 MHz after beamforming

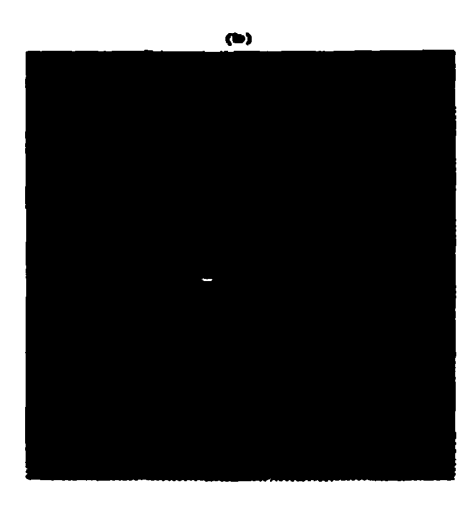
7.2b Synthetic Aperture Imaging

This section presents results for experimental investigation of the proposed MSAF method described in Section 6.2b and is compared to the Delay-Sum-Add method. One of the phantoms used is the wire and cyst phantom described in Section 5.1.3d. The wires are at different spatial positions and are used to test the point spread function at different lateral and axial positions. The lesion and scattering phantom (Section 5.1.3c) are used to test contrast resolution. To test the subaperture system, 8 parallel channels, both in transmit and receive, $N_t = N_r = 8$, where N = 64, are used here. All the processes are carried out digitally to emulate digital imaging systems.

Figure 7.2.1b shows the images of the wire phantom corresponding to K = 8 transmitreceive subapertures. The full aperture i.e. delay-sum-add (DSA) images are shown in Figure 7.2.1a These images illustrate that the point resolution of the MSAF technique does approach to that of the DSA method, although, the MSAF method produces higher sidelobes than the DSA method.. The contrast level of MSAF method is much worse than the DSA method.

Figure 7.22 shows another images of the wire phantom, to test the point spread function at different depths and lateral locations. The lateral resolution of the MSAF image (Figure 7.22c) is poor compared to DSA image (Figure 7.22b). Also on observing the right Figure 7.22c, the axial resolution is worse when compared to Figure 7.22b.





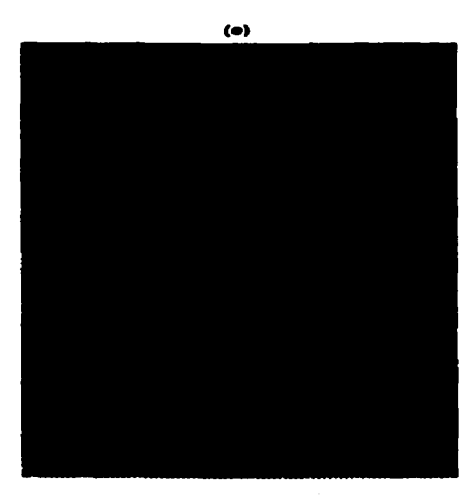
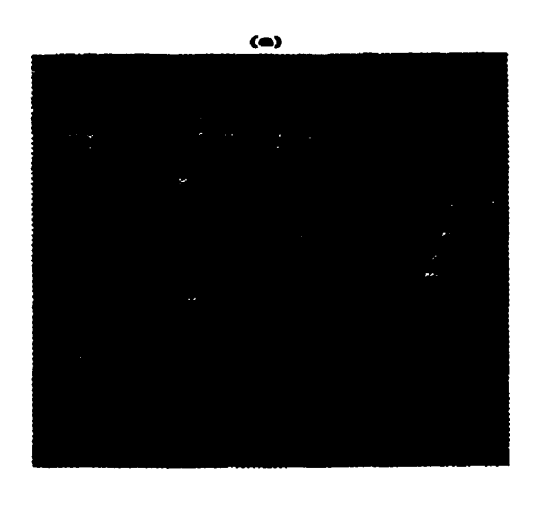
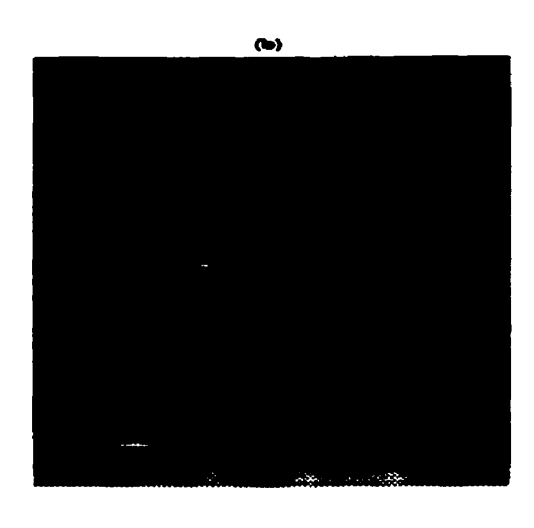


Figure -7.21 Images of the wire and cyst phantom after (a) beamforming by ATL machine (b) beamforming by DSA architecture (c) beamforming by M-SAF architecture





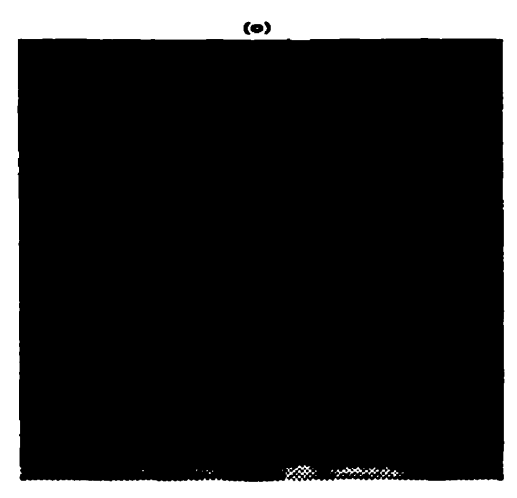


Figure -7.22 Images of wire phantom after (a) beamforming by ATL machine (b) beamforming by DSA architecture (c) beamforming by M-SAF architecture

Figure 7.23 shows the scan-converted images of the cyst phantom for the MSAF and DSA methods. Straightforward examination of the images shows that the contrast resolution with MSAF method (Figure 7.23b) is worse than the image with DSA method (Figure 7.23c). But the cysts in MSAF image are more rounded while those in the DSA image are of ovoid shape. A quantitative comparison of the CNR (contrast-to-noise-ratio) for the images is done, by computing it as follows:

$$CNR = \frac{\left|\mu_c - \mu_s\right|}{\sqrt{0.5(\sigma_c^2 - \sigma_s^2)}},$$

where μ_c and σ_c^2 are the mean and variance of the intensity within the cyst, and μ_s and σ_s^2 are the mean and variance outside the cyst. The mean CNR is computed over three cysts in the phantom (Figure 7.23) using 40 dB display dynamic range. Also the signal-to-noise-ratio (SNR) in dB of a phased array (DSA method) and synthetic aperture (MSAF) method are given by $20\log(N\sqrt{N})$ and $20\log(\sqrt{K_sK_sN_e})$ respectively [36]. Table 7.4 presents the values for CNR and SNR for the ATL image, M-SAF and DSA methods. The CNR value of all the images, for both the techniques are normalized to that of the CNR value of the ATL image. The M-SAF method has a lower SNR and CNR ratio compared to the DSA method. These results show that images of poor quality are produced with smaller apertures.

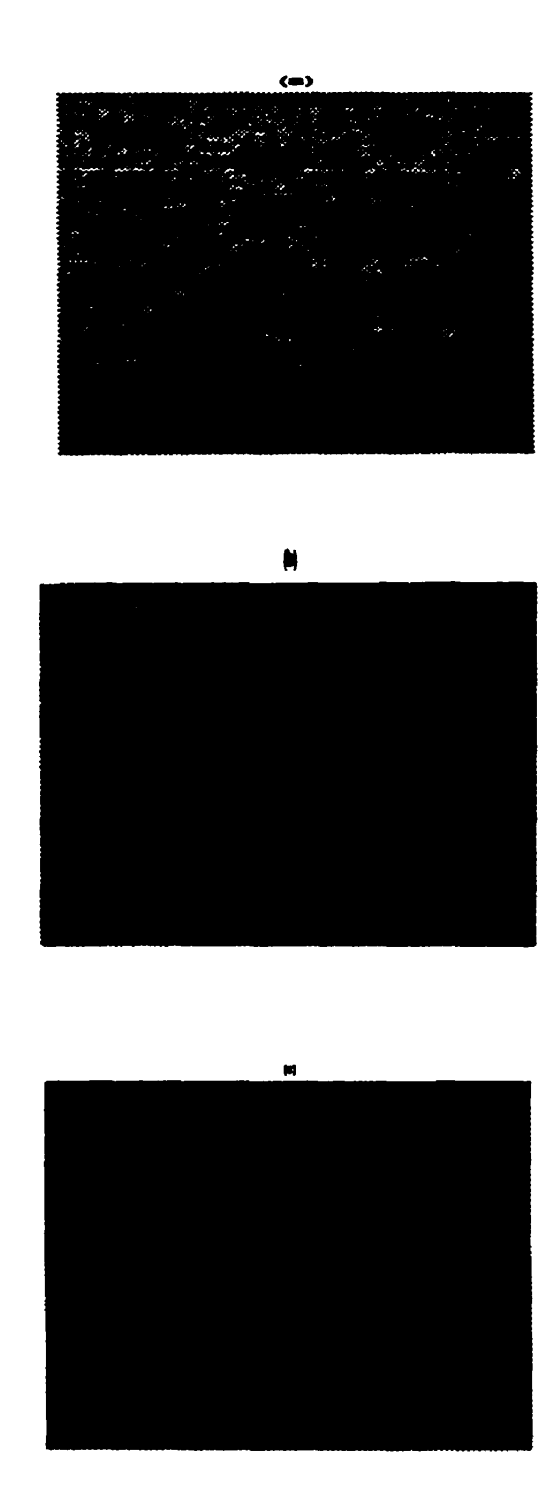


Figure -7.23 Images of the cyst phantom after (a) beamforming by ATL machine (b) beamforming by DSA architecture (c) beamforming by M-SAF architecture

Table -7.4 Normalized CNR and SNR for DSA and M-SAF architecture

Architecture Phantom	Delay-Sum-Add (DSA)	Multi-synthetic aperture focusing (M-SAF)
phantom		
Cyst phantom	0.09	0.013
SNR [dB]	51.04	35.2

8. Discussion

8.1 Simulations

Figure 7.1 demonstrates the improvement in lateral resolution after apodization when compared with images produced with no apodization. The processed images show better resolution and lower side lobe level compared to unprocessed raw data. These figures show gray scale images of a typical wire object created using configuration A. The first image (Figure 7.1a) is the unprocessed image (without apodization). It has wide lateral resolution due to the spreading of the beam. The next two images (Figures 7.1b and 7.1c) produced after processing exhibit progressively narrower lateral resolution, even though the differences between the rectangular apodization and hanning apodization cannot be distinguished easily from these figures. This is consistent with the theory discussed in Section 4.2. Apodization weights the elements to the produce apertures shown in Figure 4.2 (Section 4.2). These apertures restrict the spread of the beam, thus produce narrower beams when compared to cases without apodization. The weighting also reduces the side lobe level resulting in an increase in dynamic range, where dynamic range is the ratio of maximum axial response to the maximum off-axis response.

Figure 7.2 also shows the beam response of a wire object with respect to the lateral and axial distances, obtained without processing and with processing. Fig. 7.2a has wide beam at the focus and also higher sidelobe levels. This is because there is no processing done on the RF data. Figures 7.2b and 7.2c show the beam response after processing.

Notice that the beam is narrower and also produces lower sidelobes. It can be seen that hanning apodization produces lower sidelobes and narrower beams when compared to a uniform rectangular apodization. The improvements in the sidelobe level results from the product of the apodized transmit beam pattern and receive beam pattern.

It can be observed from Table-7.1 that the side lobe levels are around -10 dB when there is no processing and around -11 dB and -15 dB with uniform apodization and hanning apodization respectively. Also the side lobe levels after processing are progressively lower levels as the focal range increases. The reduction in side lobe level amplitude for hanning windows increases larger ranges, when compared with rectangular apodization. This can be attributed to the non-uniform nature of weighting. The results obtained are expected as discussed on in Section 4.2, except at 103 mm for rectangular window, which shows a higher level than the non-processed case. This may be due to errors(inaccurate measurements) in the simulations conducted.

Figure 7.3 shows the improvement in beam width as a function of focal range with apodization. Although lateral resolution should be independent of depth, the resolution of the wire at 107 mm with rectangular apodization is worse than the two wires at shallower depths. In case of hanning apodization it can be noticed that, the resolution remains almost constant with increasing depth. In case of resolution without apodization, there is a marked increase in the beam width as we move from the array. This is due to the broadening of the beam in the far zone, while in processed cases weighting controls the beam width.

Figure 7.4 shows the lateral beam width versus depth. There is a gradual deterioration in the lateral resolution as the object is placed at increasing distances away from the fixed focus. This is expected, but as can be observed from the plots, the deterioration in the lateral resolution is far less when apodization is used and hence increase focusing. These beam widths are compared to the beam widths at the focus for both processed and unprocessed cases, which are found to be 3.7, 3.3, 3.1 millimeters without apodization, with rectangular apodization and with hanning apodization respectively. A hanning window has a gradually decreasing slope compared to the rectangular weighting. From Figure 4.3 (Section 4.2), it can be noted that the hanning window approaches zero in smoother fashion and hence contributes to better beam width control.

Figure 7.5 is the surface plot comparison for a typical simulated analog beamformer with single fixed focus and multiple transmit focus and a digital beamformer with dynamic apodization and receive. The analog beamformer with single transmit focus (configuration B) show higher beam spread and side lobes around the deeper wire objects. The analog beam former is focused at one point on transmit and hence there is a gradual convergence of the beam around that focal point only, resulting good resolution at the focal point. Using a multiple transmit foci and receive method (configuration C) improves the axial and lateral resolution (Figure 7.5b). The beam widths are narrower when compared to configurations B and D due to the use of a larger aperture. However this causes an increase in number of side lobes. Figure 7.5c shows the remarkable improvement achievable by employing a digital beamformer. The side lobes are practically non-existent, which is due to the continuos focus maintained on receive. The

beams show better focusing because of dynamic apodization, where the ratio of the aperture to the desired focal depth are greater than the ratio of array length to its focal length.

Figure 7.6 plots the beam width versus the focal range at two signal levels. The advantages of using a digital beamformer are obvious. The lateral resolution deterioration at lower signal levels are higher in configurations B and C than in D. The beam widths are double when compared at the -6 dB level. The depth of field is significantly reduced when a single transmit focus is used. There is an increase in beam width see from Figures 7.6a to 7.6c of approximately 100% at -6 dB. Configuration C and D show narrowing of the beam at -10 dB for deeper distances. This is due to the use of multiple transmit and receive. At the -6 dB signal level, the beamwidth for configuration B increases dramatically beyond the fixed transmit focus while in configuration C and D, they are nearly constant for the entire focal range except at later depths. The diffraction limited resolution at all ranges is because of the transmit and receive aperture are nearly in focus. However configuration D requires a complex scan converter and a large dynamic range for the ADC's. The beam width for configuration C is lower than for configuration D for all ranges, is due to the use of a larger receive aperture. Figure 7.7 shows the frequency spectrum for each system. Configuration D has lower side lobe levels around -25 dB. This is due to the dynamic apodization. Configuration C shows higher side lobe levels around -20 dB, which is due to the larger aperture being employed. Configuration B shows higher side lobe levels due to the lack of any control on transmit for deeper distances.

Table 7.3 shows that there is an improvement in lateral resolution of about 50 % for configuration D when compared with B for all ranges. There is nearly a 30 % increase in lateral resolution for configuration C when compared with B but it is better at higher signal levels.

8.2 Experimental investigations

8.2a Delay-Sum-Add architecture

The efficacy of the proposed Delay-Sum-Add architecture is compared with the common analog beamformer architecture. The images generated using the analog beamforming (Aloka, SSD-246) show poor lateral resolution because of the transducer array design of the ultrasound machine used. The inter-element spacing of the array is 2 mm, which causes the appearance of many grating lobes. This contributes to the degradation of the images. As presented in Section 4, an inter-element spacing that is greater than d/λ causes grating lobes to appear, as in this case. The DSA method does improve the image quality and lateral resolution that can be observed from Figures 7.9b, 7.10b and 7.11b when compared with the images in Figures 7.9a, 7.10a and 7.11a. Properly delaying the samples and summing them, produces a coherent, strong signal with a narrow beam width and lower side lobes. An improvement in the lateral resolution though not clear in Figure 7.9bb is noticed in the enlarged beamformed image (Figure 7.10b). Since the array is always in focus while on receive, the main lobe width is narrower (Section 8.1, Figures 7.6 and 7.7). Thus the curvature of the sphere is clearly visible after beam forming (Figure 7.10b). The edge detected images also demonstrate that beamforming does help

in improving image definition. The summing of signals after delaying reduces the spurious signal level in the system, hence enhanced detection of reflected signals is achieved. This is further obvious from Figure 7.11a, which shows noise in the background of the raw image. The ability of the analog beamformer to bring out the real signal is reduced. This results in reduced contrast when compared with DSA beamformed image.

The frequency spectrums (Figures 7.12a and 7.13a) show the difference in the main lobe and side lobe levels. With beamforming, summation increases the energy of the resulting signal, which means higher amplitudes for envelope detected signals, which in turn means brighter images. Though this is not clearly visible from Figure 7.9b, may be due to the quantization error while delaying the signals [24]. Since the signals are delayed by advancing them according to the corresponding delays, they may not exactly match real time delayed signals. This may lead to less than coherent summing of the signals resulting in lower than expected amplitudes. This quantization error results in lower array gain and higher side lobe levels (Section 3). By observing the frequency spectrum of the beam formed signal, we do see the increase in amplitude of about 5 dB at 3MHz when compared with Figure 7.12a for the raw signal. The beam plots for the beamformed signal (Figure 7.13b) reveal that the main lobe beam width is reduced, thus improving lateral resolution. The beam width is reduced by 5% when compared with the raw signal (Figure 7.12b). Also the side lobes present in Figure 7.12a disappear after beamforming (Figure 7.13b). This is in line with the discussion earlier for configuration D (Section 8.1, Figure 7.7) and in Section 3 that proper delaying reduces the side lobes [24], thus

increasing the contrast. Some beam spread is also visible at -8 dB (Figure 7.13b) for the beamformed signal. This may be due to improper delaying causing quantization errors [24].

The processing time for DSA method increases with the size of data, and number of channels in the array. and thus the frame rate due to the increase in processing steps viz. delaying, summing etc. The computational time could be reduced by the use of multiple beamformers, each servicing a set off channels, thereby enabling the parallel processing of data. Also the data storage space needed for DSA method is very high due to the multiplicity of the processes. Also data storage space increases with the sampling rate. This can be reduced by buffering the data for each scan angle until the array starts scanning a new angle and new data acquired move in. Also by sampling at Nyquist frequency and then performing interpolation beamforming (Section 6.2a, Figure 6.2 and 6.3), storage space can be reduced.

This temporal interpolation results in appreciable saving of storage sample due to the reduced number of samples, which when translated to hardware means savings in A/D circuitry and reduction in cable bandwidth for data transmission. Figure 7.17 shows that sampling at around the Nyquist rate is not enough for imaging. Since the transducers were designed as wide band (Section 5.1.4b, Figure 5.3b), sampling at twice the center frequency of the transducer will produce aliasing, and also exclude the necessary frequency components that lie beyond the Nyquist rate. Thus sampled data loses a lot of information as can be seen in Figure 7.17, where there is a lot of 'gray' in the images.

Even digital beamforming does not help in improving the images. As discussed in Section 3 and 5.1.4, the bandwidth of the waveform determines the sampling frequency. This is because information content is dependent on the bandwidth and not on center frequency of the transducer. Thus when digital beamforming is done on signals sampled at higher frequencies, it results in images with higher dynamic range and contrast (Figure 7.18). This is because the signals exhibit higher main lobe and lower sidelobe levels (Figure 20b). Sampling at around Nyquist frequency produces aliasing and harmonics (Figure 20a), resulting in low dynamic range, and hence poor image quality (Figure 7.17). Event though interpolation beamforming help in obtaining images comparable in quality (Figure 7.19a) with Figure 7.18b, the optimum placement of the interpolation filter is also an important consideration (Figure 7.19). Images obtained with prebeamforming interpolation (Figure 7.19a) have better dynamic range, contrast and brightness when compared with postbeamforming interpolation (Figure 7.19b). This may be because of quantization errors in postbeamforming. As the delay operations (advancing the signals) are performed at 10 MHz, the quantization step is high and so accurate delays cannot be implemented to advance the signals. This results in less than coherent summing of the signals, resulting in lower mainlonbes, wider beams and higher side lobes as is evident from Figure 7.20d. Also the postbeamforming filters must accommodate peak amplitude corresponding to the addition of signals, whereas the prebemforming interpolation filters need only accommodate peaks corresponding to data of a single channel. On the other hand prebeamforming interpolation is the same as beamforming at 25 MHz, with the signal samples being estimates at the higher frequency. Thus the upsampled signal (Figure 7.20c) show a frequency spectrum similar to that at 25

MHz (Figure 7.20d). This results in images comparable to Figure 7.18b. The upsampled signals may be affected by filter dynamic range, resulting in higher side lobes as evident from Figure 7.20c. However interpolation beamforming does help in reducing storage space and also processing time is not too different from that needed for beamforming with no interpolation.

Limitations

There are certain limitations associated with the Delay-Sum-Add architecture. These limitations are:

- 1) target ambiguity caused by ohase quantization errors
- 2) limitations in delay line systems
- 3) increased hardware complexity
- 4) low frame rate

The time delay for transmit and receive given by Equation 6.2 (Section 6.2a) are usually discrete. This leads to quantization approximation to the ideal focusing and steering delay curves. This in turn can lead to a phase grating effect that produces grating lobes within the image field of view. These are independent of the amplitude grating lobes produced to due to the inter-element spacing. These anomalous responses degrade the resolution of the system and decrease the image dynamic range as seen in Figures 7.9b and 7.10b. Several approaches have been considered to minimize the grating lobes [1], one of the solutions being decreasing the time delay increments.

Even though the digital delay systems have become practical and offer many advantages over analog delay lines, there are shortcomings primarily associated with sampling rate and noise in the digital circuitry. Since the sample rate is generally four to ten times to that established by the Nyquist criterion, the minimum delay increment is larger thus causing phase quantization error and also necessitates the use of A/D converters with large dynamic range, increasing the cost of the beamformer. This limitation can be avoided with use of interpolation beamforming as discussed above.

The system complexity is directly related to the number of elements or channels in an array that is used for transmit and receive. In DSA architecture since all the elements are used for transmit and receive, it increases the hardware needed for each channel i.e. each element would need a delay line, ADC, amplifier etc. All this increases the cost of the system. Reducing the number of active elements by employing synthetic aperture methods can reduce the system complexity and cost which is discussed next.

The use of a large number of elements increases the number of beam lines which means better resolution but a slower frame rate. Thus DSA architecture is not suited for high speed imaging like 3-D ultrasound imaging.

8.2b Synthetic Aperture Imaging

As observed from Figure 7.21, M-SAF method does produce images with the resolution almost comparable with the commonly employed DSA processed images. The point

resolution does get better with M-SAF processing (Figure 7.21c), as we move further down the phantom. This is because of the smaller subapertures being used, which in turn increases the focal range for the aperture. Also Figure 7.22c indicates poor lateral and axial resolution when compared with the DSA processed image (Figure 7.22b). This may be due to the smaller aperture being used and hence fewer beam lines are formed. This increases the lateral resolution. More beam line scan be formed by beam space interpolation [33], thus reducing the lateral resolution. Poor axial resolution is due to the low dynamic range as is evident by the poor contrast in the M-SAF images produced (Figures 7.21c and 7.22c). The synthetic aperture produces higher side lobes (Figure 7.22c).

Contrast level is tested, using the cyst phantom. It is obvious comparing the images in Figure 7.23 that the M-SAF processing produces image (Figure 7.23c) of poor contrast when compared to DSA processed image (Figure 7.23b). The poor contrast is due to the lower signal amplitude for the beams due to the smaller apertures. In the DSA method, the entire array is used for transmit and receive, thus receiving contributions from each element. But in M-SAF method, subapertures of 8 elements are used which means lower beam amplitudes. Also the ability of these apertures to lower side lobe is limited due to fewer elements compared to the full array in the DSA method, producing images with lower dynamic range. These contribute to producing images with lower contrast levels in the M-SAF method. The cysts are rounded in the M-SAF image compared to the ovoid shape in the DSA image. This is because of the quantization errors introduced in the processing. As can be recalled from Section 5.1.2, delays are implemented by advancing

the signals, they may not accurately represent a real-time delayed signal with same delays. This error may depend on the quantization steps dictated by the sampling frequency. This error is more pronounced in DSA method because of the larger aperture used for beamforming, while in M-SAF method only 8 elements are used at a time for beamforming. So the ovoid shape in the DSA image is due to the less than coherent summing of the RF data.

Table 8.1 quantifies the CNR and SNR levels. The DSA method show higher CNR and SNR ratios indicating better image quality. Since more transmit and receive elements are used, the SNR increases, thus producing images with higher contrast when compared to M-SAF method. By summing more number of signals in DSA method, for each scan angle reduces the noise, assuming they are not correlated. This increases the SNR of the beamformed signal.

The system complexity, defined as the number of active channels during imaging, is lower for M-SAF method compared to the DSA method. It is reduced by a factor of Kt/N and Kr/N for transmit and receive respectively, compared to the DSA method.

Limitations

The M-SAF architecture has its limitations related to penetration of ultrasound in tissue. Since fewer elements are used for transmit, the combined strength is less that of the DSA architecture which uses all the elements in the array. Also there will be some loss of echo

strength due to beam spreading since the transmit beam will not be well focused as with the methods that use the full transmit aperture. Since fewer elements are used on receive, the noise cannot be suppressed by beamforming as efficiently when full receive aperture is used. Hence synthetic aperture method works in those regions where there is no dynamic range limitations. The fewer number of beam lines produced by the synthetic aperture method though increasing the frame rate produces images with poor lateral resolution. Another major limitation of the synthetic aperture method is its susceptibility to motion artifacts during the transmit firings. However investigations have been carried out to compensate for the phase aberrations caused due to movement of tissue while imaging [33]. Compensation can be avoided if fewer active elements are used in the subpaertures.

9. Future Work

Ultrasonic imaging is proving to one of the most important tools for diagnostic imaging and is gaining clinical popularity. With digital beamforming, novel beamforming methods can be exploited. Not only will digital beamforming (DBF) use in ultrasound systems increase but it will also help in producing systems with high image quality at lower costs. As technological advancements are made, it will become viable to design and construct diagnostic ultrasound systems with near optimal imaging characteristics. The Delay-Sum-Add approach to acoustic imaging offers great versatility for both realtime and off-line processing. These may have important implications in teleimaging, where the subjects are in inaccessible terrain, while all the processing is done off-line, in a nodal center. Such systems are under development now. Arrays with increased number of elements can be developed for improving the dynamic range. To overcome the effects of image speckle in coherent DSA architecture, transducer angulation or spatial compounding [39] techniques are being developed, where averaging techniques for the images are employed. This method helps in improving the spatial resolution as well as the detectability of low-contrast regions. Multi-frequency compounding technique or harmonic imaging is also proving to be useful in reducing image speckles [1]. In this method, several images are formed at different frequencies by using transducers of different frequency or by driving a broad-band array at different frequencies in its passband. With a view to reducing the hardware requirements and the bandwidth required for digital processing, new techniques to efficiently generate sample clocks for dynamic focusing and steering must be developed.

With an eye on producing images of comparable quality with low channel counts, considerable research is being conducted in the area of synthetic aperture processing. With low channel count, lower power consumption and simpler digital circuitry, the synthetic aperture method can be directly applied to personal computer based and handheld scanners. Transmit/receive circuitry, a custom digital beamformer along with a image display such as an LCD, can produce a small package. Also the M-SAF methods can be further improved with use of transmit defocusing through beam optimization or filtering techniques [41]. One of focal areas in synthetic aperture imaging will be on phase aberration and motion compensation [30, 33] that may ultimately lead to real-time applications.

With the development of 2D arrays, 3-D ultrasound is proving to be a powerful method for imaging. The high frame rate necessary for real-time volumetric imaging can be achieved by using the synthetic aperture techniques. The acquisition speed of a synthetic aperture can be increased not by decreasing the beam lines but by decreasing the number of transmit elements in the aperture. Thus good lateral resolution can be maintained.

10. Conclusion

This thesis has looked into the gradual shift of beamforming from analog to digital and also traced the evolution of digital beamformers to its present day commercial implementations. The effect of apodization on lateral resolution and side lobes were studied through simulation. While rectangular apodization have narrower lateral resolution when compared with hanning apodization, it has higher side lobes. So a compromise between the two was used as apodization weight. With digital beamforming, the advantages of it over conventional analog beamformers has been brought out by comparing its performance with the simulated analog beamformer implementation. Digital beamforming does help in improving the image quality and has improved lateral resolution compared to analog beamformers. Also the increased dynamic range in a digital beamformer is due to the dynamic receive focusing and apodization. Two different architectures of digital beamformer have been compared through experimental investigations. The DSA architecture produces high resolution images but at a high cost due to the many parallel transmit and receive channels. Interpolation beamforming reduces the sampling rate, saving storage space but lowers the dynamic range and contrast. It had higher contrast levels when compared to the alternate architecture, synthetic aperture imaging where a large aperture is synthesized by multiplexing a smaller aperture over a large array. This method produced images with poorer lateral resolution and was susceptible to motion artifacts, but helped in increasing the frame rate that is suitable to do 3-D imaging. Also the system complexity is lower due to the low channel count. Thus with more research, images of comparable quality of DSA architecture can be produced at a lower cost through synthetic aperture imaging.

References.

- [1]. Olaf T. Von Ramn, and Stephen W. Smith, "Beam steering with linear arrays", 1974 IEEE Trans. on Biomedical Engineering, Vol 30, No. 8, pp 439.
- [2]. Gehlbach, S. M. and Alvarez, R. E., "Digital ultrasound imaging techniques using vector sampling and raster line reconstruction systems", 1981, *Ultrasonic Imaging* 3, pp 107.
- [3]. Mucci, R.A., "A comparison of effecient beamforming algorithms", *IEEE Trans. Acoust. Speech Signal Processing*, 1984, ASSP-32, pp 548.
- [4]. Kim, Y. G., and Park, S. B., "New dynamic focusing scheme for ultrasound scanners", 1987, *Electronic letters* 23, pp 181.
- [5]. Song, T. K. and Park, B. S., "A new digital phased array system for dynamic focusing and steering with reduced sampling rate.", 1990, *Ultrasonic Imaging* vol 12, pp 1.
- [6]. Christensen, D. A., "Ultrasonic bioinstrumentation", 1988, John Wiley and Sons
- [7]. Kim J. H., Song, T. K. and Park, B. S, "A pipelined sampled delay focusing in ultrasound imaging systems", *Ultrasonic Imaging* vol 9, pp 75.
- [8]. McKeighan, R. E. and Buchin, M. P., "New techniques for dynamically variable electronic delays for real time ultrasound imaging", 1977, *Ultrasonics Symposium Proceedings*, pp. 250.
- [9]. Somer, J. C., "Electronics sector scanning for ultrasonic diagnosis", 1968, *Ultrasonics*, vol 6, pp. 153
- [10]. Anderson, W. A., "A new real time phased array sector scanner for imaging the entire adult human heart", 1977, *Ultrasound in Medicine*, vol. 3B, pp. 1547.
- [11]. Thurstone, F. L. and Von Ramn., "Electronic beam steering for ultrasonic imaging", 1974, *Ultrasound in Medicine*, pp. 43.
- [12]. Von Ramn and Thurstone, F. L., "Thaumascan: Improved image quality and clinical usefulness", 1970, *Ultrasound in Medicine*, vol. 2, pp. 463.
- [13]. Eaton, M. D., Melen, R. D. and Meindel, J. D., "A flexible, real-time system for experimentation in phased-array ultrasound imaging", 1980, *Acoustic Imaging*, vol. 8, pp. 55.

- [14]. Karrer, H. E., Dias, J. F. and Pering, R. D., "A phased array acoustic imaging system for medical use", 1980, *Ultrasonics Symposium Proceedings*, pp. 757.
- [15]. Tancrell, R. H., Callerame, J., and Wilson, D. T, "Near-field, transient acoustic beamforming with arrays", 1978, *Ultrasonics Symposium Proceedings*, pp. 339.
- [16]. Wright, J. "Resolution issues in medical ultrasound",1985, *IEEE Ultrasonics Symposium Proceedings*, pp. 793.
- [17]. Reid, J. M, and Wild, J.J., "Current developments in ultrasonic equipment for mechanical diagnosis", 1956, Proc. Nat. Electronics Council, vol. 12, pp. 44
- [18]. Burckhardt, C. B. et al., "A simplified ultrasound phased arrays sector scanner", 1979, Echocardiology, pp. 385.
- [19]. Walker, J. T. and Meindl, J. D., "A digitally controlled CCD dynamically focussed phased array", 1975, *Ultrasonics Symposium Proceedings*, pp. 80
- [20]. Stonestrom, J. P and Anderson, W. A., "A custom nMOS chip for medical ultrasound", 1982, VLSI Design, May, pp. 44
- [21]. Manes, G. F., Atzeni, C., and Susini, C., "Design of a simplified delay system for ultrasound phased array imaging", 1983, *IEEE Transactions on Sonics and Ultrasonics*, vol. 30, No. 6, pp. 350.
- [22]. Manes, G. F., Atzeni, C., and Susini, C., Somer, J. C., "A new delay technique with application to ultrasound phased-array imaging systems", 1979, *Ultrasonics*, Sept, pp. 225.
- [23]. Peterson, D. K, and Kino, G. S., "Real-time digital image reconstruction: A description of imaging hardware and an analysis of quantization errors", 1984, *IEEE tran. Sonics. Ultrason*", vol. SU-31, pp. 337.
- [24]. Steinberg, B. D., "Digital beamformating in ultrasound", 1992, *IEEE Transactions on Ultrasonics, Ferroelectrics, and Frequency control*", 39, pp. 716.
- [25]. Linden, D. A., "A discussion on sampling theorems", 1979, Proc. IRE, vol. 47, pp. 1219
- [26]. Cho, W. H., and Ahn, Y. B., "Multi-order sampling for digital beamforming of wide-band signals", 1996, *IEEE Transactions on Ultrasonics*, Ferroelectrics, and Frequency control", vol. 43, No.3, pp. 495
- [27]. O'Donnell et. Al, "Real-time phased array imaging using digital beam forming and autonomous channel control", 1990, *Ultrasonics Symposium*, pp. 1499.

- [28]. Lockwood, G. R., Talman, J. R., and Brunke, S. S., "Real-time 3-D ultrasound imaging using sparse synthetic aperture beamforming", 1998, *IEEE Transactions on Ultrasonics, Ferroelectrics, and Frequency Control*, vol. 45, No. 4, pp. 980.
- [29]. Ozaki, Y., Sumitani, H., Tomada, T., Tanaka, M., "A new system for real-time synthetic aperture ultrasonic imaging", 1988, *IEEE Transactions on Ultrasonics*, Ferroelectrics, and Frequency Control, vol. 35, No. 6, pp. 828.
- [30]. Nock, L. F., and Trahey, G. E., "Synthetic receive aperture imaging with phase correction for motion and for tissue inhomogeneities-Part 1: Basic Principles", 1992, *IEEE Transactions on Ultrasonics, Ferroelectrics, and Frequency Control*, vol. 39, No. 4, pp. 489.
- [31]. Ylitalo, J. "Synthetic aperture ultrasound imaging using a convex array", 1995, *IEEE Ultrasonics Symposium*, pp. 1337.
- [32]. Ylitalo, J., and Ermet, H., "Ultrasound synthetic aperture imaging: Monostatic approach", 1994, *IEEE Transactions on Ultrasonics, Ferroelectrics, and Frequency Control*, vol. 41, No. 3, pp. 333.
- [33]. Karaman, M., Bilge, S. H., and O'Donnell, M., "Adaptive multi-element synthetic aperture imaging with motion and phase abberation correction", 1988, *IEEE Transactions on Ultrasonics, Ferroelectrics, and Frequency Control*, vol. 45, No. 4, pp. 1077.
- [34]. Karaman, M., Li, Pai-Chi., and O'Donnell, M., "Synthetic aperture imaging for small scale systems", 1995, *IEEE Transactions on Ultrasonics, Ferroelectrics, and Frequency Control*, vol. 42, No. 3, pp. 429
- [35] Ziomek, L. J., Fundamentals of acoustic field theory and space-time signal processing, CRC press, 1995
- [36] Karaman, M., Li, Pai-Chi., and O'Donnell, M., "Array processing for hand-held scanners", 1994, *IEEE Ultrasonics Symposium* pp. 1543
- [37] Karaman, M., and O'Donnell, M., "Subaperture processing for ultrasonic imaging", 1998, *IEEE Transactions on Ultrasonics, Ferroelectrics, and Frequency Control*, vol 45, No. 1, pp. 126
- [38] Frazier, C. H., and O'Brien, W. D., "Synthetic aperture techniques with a virtual source element", 1998, *IEEE Transactions on Ultrasonics, Ferroelectrics, and Frequency Control*, vol 45, No. 1 pp. 196
- [39] Jespersen, S. K., Wilhjelm, J. E., and Sillesen, H., "Multi-angle compound imaging", 1998, *Ultrasonic Imaging*, vol. 20, No. 2, pp 82

- [40] Crombie, P., Bascom, P. A. J., and Cobbold, R. S. C., "Calculating the pulsed response of linear arrays: Accuracy versus computational effeciency", 1997, *IEEE Transactions on Ultrasonics, Ferroelectrics, and Frequency Control*, vol. 44, No. 5, pp. 997
- [41] Freeman, S., Li, Pai-Chi., and O'Donnell, M., "Retrospevtive dynamic transmit focusing", 1998, *IEEE Transactions on Ultrasonics, Ferroelectrics, and Frequency Control*, vol. 43, No. 5, pp. 1